#### ORIGINAL PAPER

# An improved One-Dimensional Turbulence model formulation for pipe and channel flows

Juan A. Medina Méndez<sup>1</sup> | Heiko Schmidt<sup>1</sup> | David O. Lignell<sup>2</sup> | Alan R. Kerstein<sup>3</sup>

#### Correspondence

Juan A. Medina Méndez. Email: medinjua@b-tu.de

#### Present address

Chair of Numerical Fluid and Gas Dynamics, BTU Cottbus-Senftenberg, Siemens-Halske-Ring 15a, D-03046 Cottbus, Germany

#### **Abstract**

We improve the One-Dimensional Turbulence (ODT) model formulation for turbulent channel and pipe flows. A substantial part of the work is focused on the use of the temporal ODT (T-ODT) formulation with potential applicability to a broader range of confined flows. We present novel guidelines for the selection of the T-ODT model parameters. Additionally, we introduce a modification of the spatial ODT (S-ODT) formulation in order to be able to simulate confined flows using a conservative Lagrangian finite volume method (FVM). The proposed S-ODT confined flow formulation allows constant flow rate (CFR) forcing-like schemes, and thus, imposition of a fixed bulk flow Reynolds number Re<sub>b</sub> in constant property flows. Most engineering flows of relevance are steady CFR-driven flows, which highlights the relevance and applicability of the proposed confined flow S-ODT formulation. We validate the modified S-ODT formulation by comparing it with T-ODT results for statistically steady channel and pipe flows, and with available Direct Numerical Simulation (DNS) data from the literature. We find, for both formulations, reasonable agreement for the mean flow. Second-order flow statistics involving normal components of the Reynolds stress tensor exhibit moderate deviations from DNS data. Nonetheless, transport-term contributions to the TKE transport equation are reasonably predicted. We find evidence of a well-defined logarithmic layer arising in the ODT model. Our results also suggest that the model performance improves for larger Reynolds number flows, consistent with the model representation of turbulence phenomenology.

#### KEYWORDS

ODT, channel, pipe, steady flow, developing flow, turbulence modeling

#### 1 INTRODUCTION AND RELEVANCE OF THE RESEARCH

Although the canonical channel and pipe flow configurations have been studied extensively, there are still numerous issues in the field of wall-bounded flows which have not been properly addressed. Such fundamental issues play an important role in a variety of applications ranging from niche topics in aerodynamic drag, to widely applied topics in heat generation and transport, e.g., relevant for today's energy transition. Detailed discussions regarding the current state of the art on wall-bounded flow research have been presented, e.g., by Marusic et al. [1]. Persistent open questions focus on the structure and scaling of wall turbulence at very large Reynolds numbers. An example of an unresolved issue is the existence and universality of different regions in the mean velocity profile, among others, the so-called logarithmic region, see [2].

The most detailed comprehensive studies of the mean velocity characteristics for turbulent pipe and channel flows have been carried out in the past by Direct Numerical Simulations (DNS) such as [3, 4, 5, 6, 7], as well as experiments, see [8, 9, 10, 11]. DNS faces important limitations due to computational costs. In terms of the spatial discretization, DNS costs scale with the cube of the flow Reynolds number. As an example, in low Mach constant properties fixed pressure gradient (FPG) driven flows, the wall-normal resolution is given by the friction Reynolds number  $Re_{\tau} = \delta/\delta_{\eta}$ , which indicates the ratio between the boundary layer thickness  $\delta$  (outer length-scale of the flow, e.g., a pipe radius or a channel half-height), and the viscous length-scale  $\delta_{\eta}$ , the latter being comparable to the Kolmogorov length-scale of the flow. In comparison to DNS, experimental studies are usually

Abbreviations: ODT, One-Dimensional Turbulence; DNS, Direct Numerical Simulation.

ZAMM 2025;00:1–49 wileyonlinelibrary.com/journal/ © 2025 Copyright Holder Name

<sup>&</sup>lt;sup>1</sup>Chair of Numerical Fluid and Gas Dynamics, Brandenburg University of Technology (BTU) Cottbus-Senftenberg, Brandenburg, Germany

<sup>&</sup>lt;sup>2</sup>Chemical Engineering Department, Brigham Young University, Utah, USA

<sup>&</sup>lt;sup>3</sup>Independent Consultant, Danville, California, USA

limited by measurement technology and accuracy. Experimental studies at large Reynolds numbers, just like DNS, are also confronted with spatial resolution issues, see [9]. Although research and development of emerging and necessary technologies would benefit from the information and accuracy delivered either by DNS or detailed experimental work, the reality is that these methodologies are expensive and not easily accessible. This is, conversely, the business case for turbulence modeling, usually represented by model families such as Reynolds-Averaged Navier-Stokes (RANS) or large eddy simulations (LES). In general, RANS and LES are filter-based approaches, in which only smooth signals are represented in a coarse numerical domain.

There is an inherent compromise in terms of accuracy when using turbulence models. The rationale for their application being that limited accuracy is better than no information in little-to-unknown flow regimes, e.g., large Reynolds number flows. Additionally, if the dynamics of the small scales are well understood and accurately modeled, to the best possible extent, the use of turbulence models can allow parametric studies and optimization procedures which would otherwise be unfeasible using only DNS or experiments. Representative examples of turbulence models are typical industrial RANS or very large eddy simulations (VLES) utilizing linear eddy viscosity models. In said models, the Reynolds stress is related to the filtered or averaged velocity gradient using a turbulent diffusivity (gradient-diffusion or Boussinesq hypothesis), see [12]. Inner layer laws are usually prescribed as part of the model constraints in wall-bounded flows, such that the numerical simulations involve mostly the outer layer of the mean flow [13, 12]. This shows an important issue in typical RANS or VLES; namely, that the correct solution generally depends on the prescribed law of the wall, e.g., the logarithmic law.

It is not trivial to solve the modeling problem without the specification of laws of the wall or gradient-diffusion approaches, but there are some valid alternatives. Data-driven statistical modeling based on the benefits of machine learning (ML) has gained recent attention. Several studies can be mentioned in this regard, e.g., [14, 15, 16]. The focus of our work, however, is not on data-driven approaches, but in map-based turbulence models. The use of mappings as a formal way to treat advective processes in turbulent flows can be traced back to the parallel development of two models: the first one is the Lagrangian vortex method for the simulation of solenoidal inviscid flows [17], and the second one is the set of generalized lattice map-based vorticity and advection-diffusion mixing models [18, 19]. Observations on stretching and folding of vortex lines, as well as the related use of maps, can also be traced back to observations and mechanisms suggested by Reynolds himself as a description for fluid mixing [20]. We contextualize the discussion to the One-Dimensional Turbulence (ODT) model, which uses a specific type of mapping, a triplet map, in order to represent turbulent transport in a 1-D domain, see [21]. Modeling of turbulent transport in this way has the advantage of delivering a representation of the Reynolds stress as a result of an ensemble average of said mappings, such that the inconvenient prescription of laws of the wall is no longer necessary. The compromise, to that extent, could be generalized as being the same associated to any turbulence model, i.e., the inherent empiricism portrayed in the form of model coefficients. Although the local and instantaneous velocity field represented in the ODT domain is naturally not equivalent to a fully resolved 3-D DNS velocity field, related statistical moments of any order (e.g., mean flow and variance of velocity fluctuations) can be represented without extensive modifications to the model formulation.

There have been several publications regarding the application of ODT on different flow scenarios, see [22, 23, 24, 25, 26]. Having said that, model applications are still in its infancy when compared with RANS, LES, or even data-driven approaches. There are, so far, no clear relations between ODT model parameter constants and usual physical quantities of interest, e.g., in classical wall-bounded flows such as channel or pipe flows. Another relevant issue in ODT is the inherent one-dimensional character of the model, and the limitations this poses when the representation of elliptic flow effects is desired, such as 2-D or 3-D flow development, recirculation, separation, among others. Low Mach number variable density pipe flow development was discussed in [27], utilizing the so-called temporal and spatial ODT formulations. Notably, flow development aspects were better captured with the help of the spatial formulation, e.g., better representation of near-wall gradients and wall-normal turbulent flux profiles in the streamwise direction, see [27]. However, the improved performance of the spatial formulation was achieved at the expense of a non-conservative numerical method implementation. This is inconvenient, since it contravenes the precepts of the Lagrangian finite volume method (FVM) used in all other adaptive-grid ODT publications.

In this paper, we revisit the application of the ODT model in turbulent pipe and channel flows. In Section 2, we summarize the most relevant features and capabilities of the existing temporal and spatial ODT (T-ODT and S-ODT) model formulation. Section 2 also introduces a novel S-ODT modification which allows the simulation of confined developing flow, utilizing a fully Lagrangian FVM. This remediates the non-conservative properties of the numerical method proposed in [27]. Section 3 details the numerical configuration, as well as the characterization of the statistically steady channel and pipe flow study cases to be discussed. Novel guidelines for the selection of the ODT model parameters are suggested in Section 4. The guidelines relate some model parameters to usual physical quantities of interest for statistically steady turbulent channel and pipe flows. Results of the selected study cases are discussed in Section 5, in the context of first and second-order velocity statistics for a likewise

selected range of Reynolds numbers. ODT results are compared with available DNS data from the literature. Finally, some concluding remarks are provided in Section 6.

# 2 OVERVIEW OF THE ODT MODEL

The appealing feature of the ODT model is its simplified representation of scalar turbulent transport, i.e., scalar advection by small-scale turbulence. The representation is best understood as the effect that a notional turbulent eddy would have on a 1-D scalar profile. That is to say, ideally, a triplet map of said 1-D scalar profile, see [28, 21]. The triplet map involves threefold spatial reduction or compression of a given property profile within some specific eddy range  $[\xi_0, \xi_0 + l]$ . Hereby,  $\xi_0$  is the representative coordinate of the left edge of the map, and l is the representative length scale of the map, i.e., the model representation of the size of a turbulent eddy. The mapping functions describing the planar and cylindrical triplet maps are detailed in Appendix A.1. Triplet maps are sampled following a stochastic process.

In the absence of friction, and of any other body force, the measure-preserving property of the triplet map for a flow defined by a 1-D velocity field guarantees conservation of momentum and kinetic energy [21]. The missing dissipation of kinetic energy due to viscous shear, which is characteristic of turbulent flow, is incorporated in ODT through an operator split method. During the time intervals between implemented mappings, 1-D transport equations for scalars are numerically integrated in a DNS-like fashion.

The majority of published ODT model applications to date have relied on the T-ODT formulation, in both Cartesian (planar) and cylindrical coordinates, see [22, 23, 24, 29, 26]. In the following, we give an overview of the most relevant aspects of the existing T-ODT formulation, focusing on low Mach number flows with constant fluid properties.

#### 2.1 T-ODT formulation

In the T-ODT formulation, the notional ODT domain, or line-of-sight through the turbulent flow, is assumed to capture the time-dependent behavior of a flow, which is statistically homogeneous in directions normal to the numerical domain. The time-dependent behavior is given by the time-integration of 1-D scalar transport equations *punctuated* by the implementation of stochastically sampled (in time) triplet maps. Mappings are required in order to modify the otherwise 1-D laminar flow which would result from the advancement of the scalar transport equations. Modeled statistical moments of the turbulent flow in the 1-D numerical domain are obtained as a result of the ensemble average of stochastically implemented mappings. The stochastic sampling of maps is discussed in Section 2.1.1, while the form of the applicable 1-D transport equations in ODT is discussed in Section 2.1.2.

Figure 1 shows a sketch of the typical T-ODT flow for the streamwise velocity component of a channel and a pipe flow, in Cartesian and cylindrical coordinates, respectively. In Cartesian coordinates, the 1-D domain can be considered a 1-D stack in wall-normal direction y, of arbitrary length and width  $\Delta z$  and  $\Delta x$ , respectively. The flow is assumed homogeneous in streamwise and spanwise directions, z and x, respectively, such that the magnitudes of x and x are not relevant, and can always be factored out from the formulation.

In cylindrical coordinates, the 1-D domain consists of ring sectors of small arc length  $r\Delta\theta$ , of arbitrary angular displacement  $\Delta\theta$ , and arbitrary length  $\Delta z$ . We note the treatment of the apparent geometrical singularity at the pole (r=0) in cylindrical coordinates. This relies on the utilization of the typical domain mapping function  $r \to \hat{r}$  which is commonly used in DNS, see [30, 31]. That is,

$$\hat{r} = \begin{cases} r & \text{if } 0 \le \theta < \pi, \\ -r & \text{if } \pi \le \theta < 2\pi \end{cases}$$
 (1)

The flow variables mapped to  $\hat{r}$  follow the identities concerning sign reversal derived in [31]. The purpose of this is to allow continuous and two-sided radial derivatives around  $\hat{r}=0$ , see [31]. Similar to the planar Cartesian formulation, the cylindrical ODT formulation assumes homogeneity of the flow properties in the streamwise z and tangential  $\theta$  directions. The only exception are inhomogeneities in  $\theta$  which correspond to potential asymmetries around the pole. These can only be caused by implementation of triplet maps for which  $\xi_0 < \hat{r} = 0 < \xi_0 + l$ .

For the sake of generality, we will use from now on a coordinate system represented by a position vector  $\underline{s} = [\psi, \xi, z]^T$ , where  $\{\psi = x, \xi = y\}$  and  $\{\psi = \theta, \xi = \hat{r}\}$  for Cartesian and cylindrical coordinates, respectively. Note that  $\xi = 0$  corresponds to the centerline coordinate in Cartesian coordinates (y = 0), and the pole coordinate  $(\hat{r} = 0)$  in cylindrical coordinates, respectively.

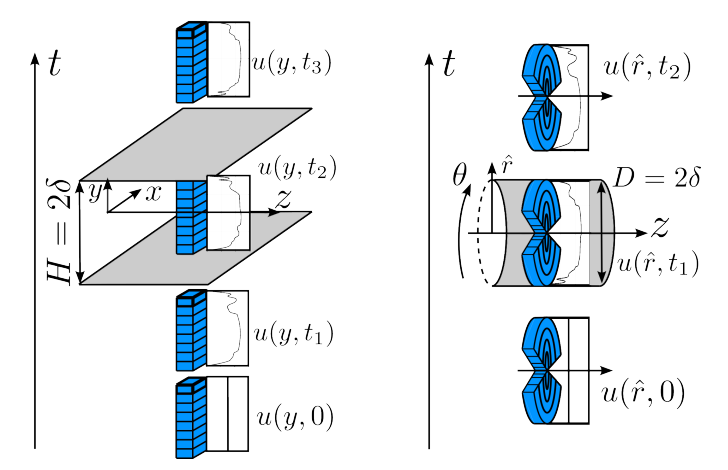


**FIGURE 1** T-ODT flow configuration in Cartesian (left) and cylindrical coordinates (right). Note that  $0 < t_1 < t_2 < t_3$ . We utilize uniform zero initial conditions for the velocity field  $\underline{u}(\xi, t = 0) = \underline{0}$ . H and D denote the height and diameter of the channel and pipes, respectively.

This implies, according to Figure 1, that walls are located at  $\xi = \pm \delta$ . The associated velocity vector for this generalized coordinate system is noted as  $u = [w, v, u]^T$ .

# 2.1.1 | T-ODT eddy events

In the following, we consider a vector velocity field providing information of the flow seen in the 1-D domain of Figure 1. Notation-wise, considering constant density, the generalized representation of v-advective transport is  $\xi^{-m}\partial(\xi^m v\underline{u})/\partial\xi$ , noting m as an integer which takes the value m=0 (and thus,  $\xi^m=\xi^0=1$ ) in Cartesian coordinates, and m=1 in cylindrical coordinates. The turbulent contribution to such advective flux can be represented in ODT by the following transformation

$$\underline{M}(u,\xi,t_e) + \underline{K}(u,\xi,t_e) : \quad u(\xi,t_e) \to u(f(\xi),t_e) + c(u,t_e,\alpha)K(\xi)$$
(2)

The sum of the operators  $\underline{M} + \underline{K}$  is given by the corresponding transformation of  $\underline{u}$  in Eq. (2). The operators  $\underline{M}$  and  $\underline{K}$  symbolically represent the added effects on  $\underline{u}$  of the triplet map  $f(\xi)$  and a so-called kernel function  $K(\xi)$ , respectively. The kernel function is defined as  $K(\xi) = \xi - f(\xi)$ . Likewise,  $\underline{c}$  is a uniform kernel coefficient (vector). From now on, we refer to the set of operations described by Eq. 2 as a candidate eddy event in ODT. An ensemble average operation of stochastically sampled and implemented eddy events models the effects of small scale turbulence on the statistical moments of the velocity field due to advective transport and pressure transport. Note that the transformation given by Eq. (2) is supposed to occur at a given (discrete, sampled) time  $t_e$ .

Notwithstanding the measure-preserving property of the triplet map, the kernel function  $K(\xi)$  is introduced in Eq. (2), in order to allow the transfer of kinetic energy from one velocity component to another, while guaranteeing simultaneous conservation of momentum. This is the ODT treatment for vector velocity fields [32, 22, 29]. Loosely speaking, the kernel coefficients indicate how much extractable kinetic energy contained in the mapping can be redistributed among velocity components following isotropy or anisotropy considerations, see also [32]. Consequently, one (non-dimensional) model parameter,  $\alpha \le 1$ , is introduced to model the tendency of the pressure to restore isotropy on the absence of shear and body forces on incompressible flow, see also [32]. This is the model representation of the pressure-scrambling effect on the Reynolds stress components for low Mach number constant property flow. Details on the choice of  $\alpha$  are given in section 4.1. Details of the procedure for calculation of  $\underline{c}$  are given in Appendix A.2.

Eddy events defined as per Eq. (2) are sampled following a stochastic process governed by three main parameters. These parameters are the eddy position  $\xi_0$ , the eddy size l, and the eddy rate distribution. The T-ODT eddy rate distribution  $\lambda_T$  is defined as

$$\lambda_{\rm T}(\xi, l, t) = \frac{C}{t_{\rm c}^2} \Delta t_{\rm l}^{-1}(\xi, l, t).$$
 (3)

Here, C is a non-dimensional proportionality coefficient, i.e., an ODT model parameter which scales the frequency of eddy events  $\Delta t_l^{-1}(\xi, l, t)$ . The frequency distribution  $\Delta t_l^{-1}(\xi, l, t)$  is modeled on dimensional grounds, in a way in which it can be

related to the flow state for any given eddy range  $[\xi_0, \xi_0 + l]$ . As a model parameter, C introduces empiricism into the ODT model, and thus, requires calibration based on some reference data.

As per Eq. (3), the sampling of eddy events in ODT is done from an instantaneous distribution which continually evolves with the state of the flow [33]. This inherent ODT feature distinguishes it from several other stochastic turbulence models, as well as other subgrid closures from filter-based turbulence models which rely on so-called equilibrium assumptions [12]. In principle,  $\lambda_T$  defines the eddy rate for a time-dependent flow-state. Integration of all possible rates leads to the mean rate  $\Lambda = \int_{l_{\min}}^{l_{\max}} \int_{0}^{2\delta} \lambda d\xi_0 dl$ , where  $l_{\min}$  and  $l_{\max}$  are bounds for all possible eddy event sizes. Clearly,  $\lambda_T$  and  $\Lambda$  define a probability density function (PDF) for eddy events  $\phi_l$ , such that  $\phi_l = \lambda_T/\Lambda$ , see [21]. Said PDF allows stochastic sampling using a Poisson process. Sampled eddies could then be implemented with probability  $P_{a,T,P} = \Lambda \Delta t_{\text{samp}}$ , or rather,  $P_{a,T,P} = \lambda_T \Delta t_{\text{samp}}/\phi_l$ , given that  $\Delta t_{\text{samp}} = (\chi \Lambda)^{-1}$  is chosen with a constant  $\chi > 1$  such that  $P_{a,T,P} < 1$ . This is a thinning method for reconstruction of  $\phi_l$ , see [29]. In practice, it is highly inconvenient to reconstruct  $\phi_l$  due to the large computational overhead implied by the need of explanation of all possible flow states at all times required for the calculation of  $\Lambda$ . Since  $\Lambda$  (or more generally,  $\phi$ ) is unless that

In practice, it is highly inconvenient to reconstruct  $\phi_l$  due to the large computational overhead implied by the need of evaluation of all possible flow states at all times required for the calculation of  $\Lambda$ . Since  $\Lambda$  (or more generally  $\phi_l$ ) is unknown, another more readily available PDF  $\phi_l^* = h(l)g(\xi_0)$  is used instead of  $\phi_l$ , in combination with a rejection method, see [33, 34, 22]. Hereby, h(l) and  $g(\xi_0)$  are presumed PDFs for the size and position of eddy events, respectively, see also [33]. In this way, the acceptance probability  $P_{a,T,R} = \phi_l l(\beta \phi_l^*)$  decides implementation of candidate eddy events by the rejection method, considering  $\beta$  as a constant such that  $P_{a,T,R} < 1$ . The final, resulting acceptance probability combining the thinning and rejection methods is obtained as  $P_{a,T} = P_{a,T,P}P_{a,T,R}$ , absorbing  $\beta$  into the magnitude of  $\Delta t_{\text{samp}}$ , such that

$$P_{\mathbf{a},\mathsf{T}}(\xi_0,l,t) = \frac{\lambda_{\mathsf{T}}(\xi_0,l,t)\Delta t_{\mathsf{samp}}}{h(l)g(\xi_0)} \tag{4}$$

We remark that h(l) and  $g(\xi_0)$  are presumed PDFs, although their exact form is not relevant, see also [33]. Bounds of h(l) are set by length-scales  $l_{\min}$  and  $l_{\max}$ . On the one hand,  $l_{\min}$  is set by the Kolmogorov length-scale, or, conversely, the viscous length scale  $\delta_{\eta}$ . On the other hand, there are no clear physical guidelines for  $l_{\max}$  (unless it is known *a priori*), although it is bounded by the size of the numerical domain  $l_{\min} < l_{\max} \le 2\delta$ . Further considerations on  $l_{\max}$  will be discussed later in Section 4.4.

The eddy event frequency  $(\Delta t_l)^{-1}$ , which is required for the evaluation of the corresponding eddy rate  $\lambda_T$  as per Eq. (3), is modeled on dimensional grounds using kinetic energy, see [22, 29, 34]. We focus on constant property flows and determine  $(\Delta t_l)^{-1}$  as follows

$$(\Delta t_l)^{-1} = \sqrt{\frac{2}{\int_{\xi_0}^{\xi_0 + l} K^2 \xi^m d\xi}} K_0 \left[ \frac{K_0}{\rho} \left( \underline{Q} \cdot \underline{1} \right) - \frac{Z}{2} \frac{\eta^2}{l^2} \int_{\xi_0}^{\xi_0 + l} \xi^m d\xi \right]$$
 (5)

We have defined the kinematic viscosity  $\eta = \mu/\rho$  as usual, given by the ratio between the (constant) dynamic viscosity  $\mu$  and the (constant) density  $\rho$ . Similarly, we note the scalar product operator for vectors  $\{\cdot\}$ , the ones-vector  $\underline{1} = [1, 1, 1]^T$ , and the factor  $K_0$  defined as

$$K_0 = \frac{1}{l^2 \int_{\xi_0}^{\xi_0 + l} \xi^m d\xi} \int_{\xi_0}^{\xi_0 + l} K^2 \xi^m d\xi$$
 (6)

The factor  $K_0$  converges to 4/27 in the continuous limit of the planar eddy event formulation, see [33, 34]. The available kinetic energy per velocity component  $\underline{Q}$ , which has dimensions of energy per unit of base area  $(\Delta x \Delta z)$  in Cartesian coordinates, and of energy per unit length and angular displacement  $(\Delta z \Delta \theta)$  in cylindrical coordinates, is defined in Appendix A.2. In this context,  $\underline{Q} \cdot \underline{1}$  is the total available turbulent kinetic energy. Note that we have also introduced another non-dimensional ODT model parameter in Eq. (5), the viscous penalty coefficient Z. The model parameter Z must be calibrated alongside C based on available reference data. In wall-bounded flows, Z generally acts as a tuning parameter for inherent 3-D buffer layer or outer layer dynamics (or their effects on the flow statistics), which cannot be properly represented by ODT [21, 35]. The viscous penalty imposed by Z may lead to imaginary values of  $\Delta t_l$ . These candidate eddy events are not implemented. Otherwise, the implementation of sampled candidates is decided after calculation of their acceptance probability  $P_{a,T}$  by Eq. (4) and a Bernoulli trial. In the usual ODT implementation,  $\Delta t_{samp}$  is adjusted dynamically, such that the moving average  $\overline{P}_{a,T}$  (defined over a suitable time window) adjusts to a very small input value (we use 0.02).

# 2.1.2 T-ODT deterministic advancement (governing equations for numerical integration)

Next, we discuss the form of the 1-D transport equations required for the numerical time-integration step which follows every implemented eddy event in ODT. This discussion also follows existing T-ODT formulations, and in particular, formulations

relying on the use of a dynamically adaptive grid, see [32, 22, 29]. From now on, we will refer to the numerical time-integration step as the ODT deterministic advancement process. In this context, we note that the numerical simulation time always corresponds to the accumulated time from the stochastic eddy event sampling procedure. Therefore, the numerical time-integration of the transport equations always catches up to implemented eddy events, which is why we also reference alternatively the ODT deterministic advancement process as a deterministic catch-up process (to eddy events).

For consistency of the presentation of this work, which is dedicated to a conservative FVM for ODT, we write the conservation equations in an integral form. Mass conservation in a finite volume cell is written as

$$\int_{\Delta\Omega} \frac{\partial \rho}{\partial t} d\Omega + \Delta \psi \Delta z (\xi^m \rho v_R) \bigg|_{\xi_c - \Delta \xi/2}^{\xi_c + \Delta \xi/2} = 0$$
 (7)

Integrals are understood over a finite volume cell  $\Delta\Omega=(\Delta\xi^{m+1}\Delta\psi\Delta z)/(m+1)$ . Note also that  $d\Omega=(d\xi^{m+1}\Delta\psi\Delta z)/(m+1)$ , whereas  $\xi^m d\xi=(m+1)^{-1}d\xi^{m+1}$ . The second term in Eq. (7) is evaluated at both edges of the 1-D finite volume cell. We reference  $\Delta\xi$  as the distance between the 1-D cell edges, and  $\xi_c$  as the mid-point of the corresponding 1-D cell. We defer a discussion of the FVM discretization scheme and numerical method to A.3. Note that we have intentionally used  $v_R$  in Eq. (7), the relative velocity between the fluid and the (analysis) system boundary, in order to refer alternatively to Eulerian and Lagrangian frameworks for familiarity. In an Eulerian framework, where the (analysis) system boundary is at rest,  $v_R$  is nonzero, and  $\Omega$  refers to a (fixed) Eulerian control volume. In a Lagrangian framework, or a material T-ODT cell volume,  $v_R=0$ , since the system boundary moves with the velocity of the fluid. The Reynolds transport theorem (RTT) relates Eq. (7) to its Lagrangian form, which is written as

$$\frac{\mathrm{d}}{\mathrm{d}t} \int_{\Delta\Omega_t} \rho \mathrm{d}\Omega = 0 \tag{8}$$

Besides the remark that  $\Delta\Omega_L \neq \Delta\Omega$ , since  $\Delta\Omega_L$  is now the Lagrangian (material) cell volume, we stress that  $v_R$  is also different from the wall-normal velocity v. Specifically, v models the 3-D velocity field in ODT. That is to say, similar to u and w, v is responsible for deciding upon implementation of eddy events in ODT via Eq. (5). However,  $v_R$ , or rather  $\rho v_R$ , is the mass flux associated to the system of 1-D transport equations, and as such, it can only be related to (pure) 1-D flow, e.g., compression or expansion of the Lagrangian (material) cell volume.

ODT formulations in previous publications usually consider a Lagrangian ODT domain and utilize a dynamically adaptive grid, see [22, 29]. Since we will also resort to the use of a dynamic grid adaption strategy, we focus our discussion on the Lagrangian form of all transport equations, e.g., Eq. (8) for mass conservation. For the case of the constant property turbulent channel and pipe flows at discussion in this work, given that  $\rho$  is a constant, Eq. (8) leads to a Lagrangian cell volume of constant size. Thus, Eq. (8) is automatically enforced for a given initial discretization of the numerical domain (at the beginning of a time-step), without the need of further operations.

In order to formulate the integral law for momentum conservation, it is important to discuss the role of the hydrodynamic pressure in low Mach number constant property flows, see [36]. Usually, in DNS of fixed pressure gradient-driven (FPG-driven) turbulent pipe or channel flows, the hydrodynamic pressure is decomposed onto a mean and a fluctuating pressure gradient. The mean pressure gradient is only non-zero in the streamwise direction. It balances the wall shear stress, and it is imposed as a uniform source term  $-d\bar{p}/dz$  on the streamwise momentum equation, see [37, 38, 39]. This has also been done in existing T-ODT formulations, see [22, 26]. Fluctuating pressure effects relevant for turbulent flow, such as the pressure scrambling effect, are not modeled in the deterministic ODT advancement process, but instead as part of the ODT eddy events as detailed in Section 2.1.1. Thus, there is no need for a pressure gradient term in the wall-normal momentum equation. Following the same mass conservation logic, we note that momentum fluxes (due to velocity advection) entering or leaving the material ODT cell volume, are not explicitly represented in a Lagrangian conservation law since  $v_R = 0$ . Considering constant density, and the fixed form of the Lagrangian finite volume cell  $\Delta\Omega_L = (\Delta \xi^{m+1} \Delta \psi \Delta z)/(m+1)$ , the integral form of momentum conservation can then be written as

$$\frac{\mathrm{d}}{\mathrm{d}t} \int_{\Delta\xi} \underline{u} \xi^m \mathrm{d}\xi = \int_{\Delta\xi} \left( -\frac{1}{\rho} \frac{\mathrm{d}\overline{\rho}}{\mathrm{d}z} \underline{e}_{\underline{z}} \right) \xi^m \mathrm{d}\xi + \left( \xi^m \eta \frac{\partial \underline{u}}{\partial \xi} \right) \Big|_{\xi_c - \Delta\xi/2}^{\xi_c + \Delta\xi/2}$$
(9)

We used  $\underline{e_z} = [0, 0, 1]^T$  to indicate the unit vector aligned with direction z. The first integral term on the right-hand side (RHS) corresponds to the FPG term imposed as a momentum source for u. The second term on the RHS is the usual viscous flux difference between cell edges valid for a vector velocity field in 1-D planar Cartesian coordinates. Although we use the vector formulation in Cartesian coordinates (channel flows), we only resort to the use of a single velocity component formulation in the specific case of cylindrical coordinates (pipe flows). This is discussed in the context of the choice of the ODT model parameter

 $D=2\delta$ 

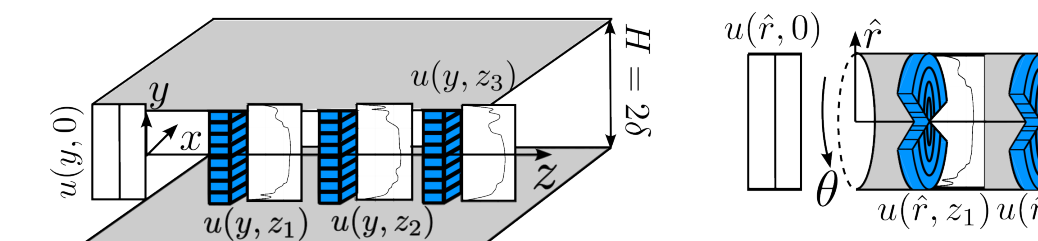


**FIGURE 2** S-ODT flow configuration in Cartesian (left) and cylindrical coordinates (right). Note that  $0 < z_1 < z_2 < z_3$ . Inlet conditions for the velocity field are set to uniform profiles  $\underline{u}(\xi, z = 0) = [0, 0, U_b]^T$ . H and D denote the height and diameter of the channel and pipes, respectively.

 $\alpha$  for cylindrical coordinates in Section 4.1. In the cylindrical, single component formulation, v = w = 0, and therefore, extended vector forms of the viscous flux for cylindrical coordinates such as those derived in [27] are not necessary.

We recall that the sole numerical integration of Eq. (9) through an entire ODT simulation without implementation of eddy events, necessarily leads to a numerical solution representing a pure 1-D (laminar) flow. For uniform initial conditions, said numerical solution satisfies symmetry conditions around  $\xi = 0$ , such that asymmetries (around  $\xi = 0$ ) can only arise due to implementation of eddy events. In the case of the cylindrical ODT formulation, eddy event implementation may lead to a numerical integration step for flow profiles which are asymmetric around the pole  $\hat{r} = 0$ . Said situation is a unique feature of the cylindrical ODT formulation, since such asymmetries are incompatible with the implied axisymmetric assumption of standard 1-D cylindrical (r-dependent) transport equations. This completes the description of the T-ODT formulation. Further details on the FVM discretization scheme and numerical method can be found in Appendix A.3.

#### 2.2 S-ODT formulation

There have been several previous studies relying on spatial ODT (S-ODT) formulations, see [22, 27, 29, 34, 40]. In general, S-ODT is a *quasi*-2-D approximation of a statistically steady flow. Such an approximation can be achieved by relying on inherently *quasi*-2-D governing equations, such as those corresponding to the parabolic partial differential equations (PDEs) applicable for boundary layer-like flows. In S-ODT, the statistically steady flow seen in the ODT line, experiences inhomogeneity in the streamwise direction due to eddy events, see Figure 2. This implies a streamwise marching logic, which is similar to the numerical schemes used to solve the *quasi*-2-D PDEs for statistically steady boundary layer-like flows; the difference being that streamwise advancement is *punctuated* in S-ODT by eddy events, similar to how temporal advancement is *punctuated* by T-ODT eddy events. Following this logic, a static 2-D flow snapshot can be recovered after one simulated S-ODT realization. Similar to T-ODT, one deterministic advancement process is always carried out catching up to implemented eddy events.

Initial conditions in S-ODT can be referenced as inlet conditions for the streamwise position z = 0. Owing to the random occurrences of eddy events that punctuate z-advancement, multiple realizations utilizing similar inlet conditions may produce an ensemble of static pictures, allowing flow statistics to be gathered. For fully developed flows which can also be considered statistically streamwise homogeneous or invariant, fluctuation statistics may also be gathered by averaging over the streamwise interval of statistically invariant advancement during one simulated realization.

In the following, we briefly review the most relevant aspects of existing S-ODT formulations, such as those presented in [22, 27, 29, 34, 40]. The formulation in [27] was the first attempt of an S-ODT formulation applicable for confined flows, since previous formulations were only applicable for unconfined systems with spatially uniform far-field flows, e.g., boundary layers, jets or mixing layers, see [34]. In such cases, the S-ODT domains allowed outgoing or ingoing mass fluxes at their endpoints. This is not physically consistent in the presence of walls at the endpoints of the S-ODT domain. Hence, a modified treatment is necessary to ensure correct balancing of momentum fluxes (due to advection by the streamwise velocity component) with the simultaneous enforcement of balanced (streamwise) mass flux in the numerical ODT domain. This is achieved only in an approximate sense in [27] through the use of non-conservative Lagrangian differential equations in the S-ODT deterministic advancement process. In an attempt to harmonize the confined flow S-ODT formulation of [27] with previous integral Lagrangian (conservative, FVM-based) S-ODT formulations, we discuss a modified confined flow S-ODT treatment in Section 2.2.3. However, for ease of understanding, we discuss next the eddy event sampling procedure, as well as the form of S-ODT PDEs corresponding to existing conservative Lagrangian FVM forms published in the literature (for unconfined flows).

# 2.2.1 | S-ODT eddy events

Next, we review the most relevant aspects of eddy event implementation in existing S-ODT formulations to date. We consider infinitesimal volume differentials of the form  $d\Omega = \xi^m d\xi dz \Delta \psi = (m+1)^{-1} \left(d\xi^{m+1} dz \Delta \psi\right)$ . All flow properties are inhomogeneous in directions  $\xi$  and z, and assumed homogeneous solely in direction  $\psi$ . The exception, as in T-ODT, are inhomogeneities in cylindrical coordinates due to asymmetries around the pole. Since S-ODT is a 2-D flow approximation, intuition may lead to believe that S-ODT conservation laws should observe 2-D material cell volumes, in analogy with the 1-D material cell volumes used in the T-ODT formulation. This is not the case. S-ODT is best interpreted instead as a streamwise array of wall-normal 1-D Lagrangian, semi-material domains. In this context, every Lagrangian ODT domain in the streamwise array can only deform in the wall-normal direction as in a fully material T-ODT domain. As in Eq. (7), this implies  $v_R = 0$  in every Lagrangian cell volume. However, it is also necessary to discuss an additional streamwise relative velocity between the fluid and the Lagrangian ODT cell volume in the S-ODT conservation or balance laws,  $u_R$ . The latter is necessarily nonzero, and in fact, we need to consider  $u_R = u$ , given that the ODT domain (a 1-D domain) can not observe streamwise deformation. Thus, each streamwise ODT domain in the array (and each cell volume within it) deforms in wall-normal direction, in order to allow incoming and outgoing streamwise mass fluxes. As in the numerical solution of boundary layer-like parabolic flows, streamwise marching schemes demand that each streamwise array member at a position  $z_{n+1}$  is determined by its upstream neighbor at position  $z_n$ .

S-ODT eddy events are sampled stochastically in the streamwise direction z as part of the streamwise marching scheme. Each S-ODT eddy event can be defined by its associated operators  $\underline{M}$  and  $\underline{K}$ , and the corresponding transformation rule in analogy to Eq. (2),

$$\underline{\underline{M}}(\underline{u}, \xi, z_e) + \underline{\underline{K}}(\underline{u}, \xi, z_e) : \underline{\underline{u}}(\xi, z_e) \to \underline{\underline{u}}(f(\xi), z_e) + \underline{\underline{c}}(\underline{u}, z_e, \alpha) K(\xi) + \underline{\underline{b}}(\underline{u}, z_e, \alpha) J(\xi). \tag{10}$$

In contrast to T-ODT, S-ODT conservation laws observe exact numerical balance of flow rates (of mass, momentum, and energy) due to associated fluxes caused by streamwise advection attributed to  $u_R = u$ , see [34]. For isothermal and constant density flows, triplet mapping of scalar profiles can only guarantee an exact balance (before and after mapping) of streamwise mass flux, as per the measure-preserving properties of the map. Triplet mapping alone is unable to balance momentum fluxes due to streamwise advection for each velocity component or kinetic energy fluxes due to streamwise advection (before and after mapping). Thus, kernel functions  $K(\xi)$  and  $J(\xi) = |K(\xi)|$ , as well as associated kernel coefficients (vectors)  $\underline{c}$  and  $\underline{b}$ , respectively, are introduced in order to satisfy the additional constraints of enforcement of i) balance of the momentum flux due to streamwise advection together with ii) balance of the kinetic energy flux due to streamwise advection, considering kinetic energy transfer between velocity components as in the vector T-ODT formulation (see also [34, 41]). The calculation of the constant coefficients  $\underline{c}$  and  $\underline{b}$  in S-ODT is defined in Appendix A.2.

As mentioned, modification of the velocity components as per Eq. (10) during S-ODT eddy events, enforces simultaneous balance of pre- and post-mapped momentum and kinetic energy fluxes (including kinetic energy transfers between velocity components). However, existing S-ODT formulations do not incorporate enforcement of streamwise mass flux balancing in the procedure for determination of  $\underline{c}$  and  $\underline{b}$ , see [34, 22, 41]. Instead, the constraint on the streamwise mass flux is performed as a corrector step upon modification of the Lagrangian ODT domain volume, after the transformation given by Eq. (10). This is an issue for confined flows which exhibit physical walls at the edges of the numerical domain, and it was remediated in [27] at the expense of a non-conservative deterministic advancement process. We discuss this issue as part of the modified treatment for the confined flow S-ODT formulation introduced in Section 2.2.3.

In order to complete the specification of S-ODT eddy events, we define the counterpart of  $\lambda_T$  from T-ODT, which can be redefined as a spatial eddy density function,

$$\lambda_{S}(\xi_{0}, l, z) = \frac{C}{l^{2}} \Delta z_{l}^{-1}(\xi_{0}, l, z). \tag{11}$$

The eddy streamwise (turnover) length-scale  $\Delta z_l(\xi_0, l, z)$  is defined in a very similar way to the eddy turnover time in T-ODT. However, S-ODT conservation laws for spatially developing flows are expressed in terms of streamwise fluxes, see [34]. Thus, the eddy streamwise (turnover) length-scale  $\Delta z_l(\xi_0, l, z)$ , or rather, the eddy streamwise (turnover) wavenumber  $(\Delta z_l)^{-1}(\xi_0, l, z)$ , is calculated as

$$(\Delta z_l)^{-1} = \frac{1}{u_l} \sqrt{\frac{2}{\int_{\xi_0}^{\xi_0 + l} u K^2 \xi^m d\xi} K_0 \left[ \frac{K_0}{\rho} \left( \underline{Q}_u \cdot \underline{1} \right) - \frac{Z}{2} \frac{\eta^2}{l^2} u_l \int_{\xi_0}^{\xi_0 + l} \xi^m d\xi \right]}.$$
 (12)

In this case,  $\underline{Q_u}$  is the available kinetic energy-flux per velocity component due to streamwise velocity advection, which has dimensions of power per unit width  $(\Delta x)$  in Cartesian coordinates, and of power per unit angular displacement  $(\Delta \theta)$  in cylindrical

coordinates, see Appendix A.2. The eddy-averaged velocity  $u_l$  is calculated for constant density as

$$u_{l} = \frac{\int_{\xi_{0}}^{\xi_{0}+l} u \xi^{m} d\xi}{\int_{\xi_{0}}^{\xi_{0}+l} \xi^{m} d\xi}$$
(13)

In analogy with T-ODT, considering now a streamwise sampling interval  $\Delta z_{\text{samp}}$ , the implementation of sampled candidate eddy events in S-ODT is decided upon calculation of the acceptance probability  $P_{\text{a,S}}$ ,

$$P_{a,S}(\xi_0, l, z) = \frac{\lambda_S(\xi_0, l, z) \Delta z_{\text{samp}}}{h(l)g(\xi_0)}$$
(14)

# 2.2.2 | S-ODT (deterministic) governing equations

As previously commented, the *quasi*-2-D S-ODT formulation is best interpreted as a streamwise array of wall-normal ODT (semi-material) domains which describe a statistically steady flow modified by the discrete implementation of eddy events in some of the domains, i.e., at some streamwise positions. The eddy events, thus, modify the otherwise steady *quasi*-2-D (laminar) boundary-layer-like flow. Similar to [34, 22, 29], we can write the integral mass conservation law for the Lagrangian S-ODT cell volume as

$$\frac{\mathrm{d}}{\mathrm{d}z} \left( \int_{z_n}^{z_{n+1}} \int_{\Delta\xi(z)} \rho u \xi^m \mathrm{d}\xi \mathrm{d}z \right) \Delta\psi = 0, \quad \text{which simplifies to} \quad \left( \int_{\Delta\xi(z)} u \xi^m \mathrm{d}\xi \right) \Big|_{z_n}^{z_{n+1}} = 0$$
 (15)

The second expression is obtained after cancellation of integral and differential operators, as well as due to the constant density assumption and constancy of  $\Delta \psi$ . The resulting integral on the second expression is evaluated at both upstream (initial) and downstream positions  $z_n$  and  $z_{n+1}$ , respectively. Unlike the T-ODT material cell volume which remains with a fixed size in constant density flows, the Lagrangian S-ODT (semi-material) cell volume will usually exhibit some degree of deformation in the wall-normal direction. The deformation is due to the changes in the inhomogeneous  $u(\xi)$  velocity profile between the upstream (initial conditions, directly after the implementation of an eddy event) and downstream positions, due to streamwise marching (deterministic advancement) of the momentum flux (due to streamwise advection). This is an important property of S-ODT domains, and it corresponds to the ODT representation of the lateral flows which are induced by streamwise flow development, as in previous, conservative, FVM-based S-ODT publications, see [22, 29, 34].

For confined flows, there can not be any inflows or outflows through the walls that reside at the domain boundaries. In practical terms, from a Lagrangian perspective, the overall size of the S-ODT domain can not change; local fluid parcels (or finite volume cells) may deform, but the sum of all fluid parcel deformations along the domain must be zero. This is a confinement constraint associated with zero (normal) mass flux at the 1-D domain boundaries. From now on, we will refer to this constraint and its enforcement as a conservative flux confinement enforcement (FCE) step. In general, the FCE is then equivalent to an imposed (streamwise) constancy of the global (domain-integrated) mass flow rate, or of the streamwise mass flux, in a domain of fixed-size  $2\delta$ . This makes the confined S-ODT formulation ideal for internal steady flows observing constant flow rates (CFR), which greatly extends model applicability. For constant density, the FCE step implies constancy of the domain-integrated bulk velocity  $U_b$ . Before commenting further on the FCE step, we detail the integral momentum conservation law of the S-ODT formulation, assuming constant density. This takes the same form as in [22, 29, 34],

$$\left(\int_{\Delta\xi(z)} u\underline{u}\xi^m d\xi\right) \Big|_{z_n}^{z_{n+1}} = \int_{z_n}^{z_{n+1}} \left(\xi^m \eta \frac{\partial \underline{u}}{\partial \xi}\right) \Big|_{\xi_c - \Delta\xi/2}^{\xi_c + \Delta\xi/2} dz \tag{16}$$

There are some relevant nuances concerning Eq. (16). In principle, the quasi-2-D formulation allows the inclusion of shear due to velocity gradients in both streamwise and wall-normal directions. Preserving the shear term due to streamwise gradients of velocity, however, although seemingly consistent, would lead to an elliptic PDE. It is not clear how this would affect eddy event sampling, given that in an elliptic context, both upstream and downstream conditions would influence eddy sampling. This is the reason why S-ODT formulations traditionally follow parabolic flow assumptions in which shear due to streamwise gradients can be considered negligible, see [34]. This is also, as previously mentioned, consistent with standard boundary layer approximations. These approximations are reasonably valid for the type of flows at discussion here, enabling flow development or changes in the context of a streamwise marching scheme. Similar reasoning favoring parabolic flow assumptions prevents the need to solve elliptic Poisson-like pressure equations, such that pressure gradients, if included, should be provided *a priori*. Nonetheless, due to

the use of inlet conditions, inclusion of any FPG source term is omitted, as it is customary for 3-D DNS utilizing inlet-outlet-like boundary conditions (BCs). As in T-ODT, the wall-normal pressure gradient is also omitted from the momentum balance law. Fundamentally, the overall role of the pressure can be understood in terms of the enforcement of mass conservation, or of the velocity divergence condition, as it is typical for low Mach number flows. This is discussed next in the context of the FCE step.

# 2.2.3 | Enforcement of mass conservation and of the confinement constraint (modifications required for confined flow S-ODT)

During the streamwise advancement of statistically stationary zero pressure gradient (ZPG) boundary layer-like flows, the wall shear stress balances, on average, the inertial streamwise acceleration. In S-ODT, there may be momentum imbalances due to wall-stress fluctuations induced by the ODT advection process. These imbalances would be responsible for variations of the global mass flow-rate, or alternatively, variations of the bulk velocity  $U_b$  in constant density flows. Nonetheless, S-ODT confined flow balance laws mandate that the global (domain-integrated) streamwise mass flux of fluid at any z agrees exactly with the inlet value due to Eq. (15). Even pure streamwise marching of Eq. (16) on the absence of turbulent transport (eddy events), and considering a fixed volume, does not satisfy this requirement. The exception being that Eq. (15) is used as an additional constraint.

In general, the z-dependent cross-section of a (semi-)Lagrangian S-ODT volume  $A_c(z)$ , i.e.,  $(m+1)^{-1}\Delta\psi\Delta\xi^{m+1}(z)$  for a certain fluid parcel or finite volume cell, is determined by Eq. (15) after advancement of Eq. (16). Solution of (15) for  $A_c$  after advancement of Eq. (16) follows an operator split rationale. This is similar to pressure projection schemes, and introduces a numerical error proportional to the size of the streamwise step  $\Delta z$ . In this context, given that momentum advancement is only part of the operator split approach, advancement of Eq. (16) is performed considering a fixed cross-sectional area of the finite volumes. Solution of Eq. (15) for all individual fluid parcels or finite volume cells, considering streamwise marching between coordinates  $z_n$  and  $z_{n+1}$  ( $\Delta z = z_{n+1} - z_n$ ), yields afterward a change in the area  $A_c(z_n) \to A_c^*(z_{n+1})$ ,

$$A_c^*(z_{n+1}) = \frac{u(z_n)A_c(z_n)}{u^*(z_{n+1})}. (17)$$

Here, we used  $u^*$  to indicate the streamwise velocity field at coordinate  $z_{n+1}$  resulting from advancement of Eq. (16). Only upon deformation of the net Lagrangian cross section  $\Sigma A_c(z_n) \to \Sigma A_c^*(z_{n+1})$  is it possible to obtain a desired constancy of the global (domain-integrated) mass flow-rate, which is given by the streamwise velocity component. Note that the aforementioned procedure for deformation of the Lagrangian volume is also considered after S-ODT eddy events, as part of the correction procedure post-Eq. (10), in order to enforce pre- and post-map balance of the global streamwise mass flux, and thus, the constancy of the global mass flow-rate. So far, this procedure is the usual one involved in the S-ODT formulation for unconfined flows, e.g., applicable in particular to a round turbulent liquid jet issuing into a vacuum (here meaning the low-density limit of the ambient fluid), see [34, 22, 29]. Note that the Lagrangian deformation procedure  $A_c(z_n) \to A_c^*(z_{n+1})$  involves displacement of the fluid parcel interfaces. As such, transport associated to the Lagrangian volume deformation can be considered to be of advective nature.

Usually, unconfined flows rely on the use of homogeneous Neumann BCs for Eq. (16). As a consequence, the streamwise velocity responsible for streamwise mass flux shows only a reduced distinctive region of the numerical domain, in which the unconfined flow is different from the free-stream (irrotational) flow. This is also the region of interest for integrated streamwise mass flux, such that uniform free-stream flow regions may be clipped out, as it is done in existing unconfined flow formulations, see also [34, 22, 29]. Having said that, imposition of homogeneous Neumann BCs on Eq. (16) is inconsistent with the physically correct no-slip BCs demanded by confined flows, and it is also inconsistent to clip out regions of a confined, fixed-size wall-bounded domain. As a way to remediate this problem, we introduce a subsequent correction on the mass flow-rate  $\rho u^*(z_{n+1})A_c^*(z_{n+1})$ . This is the novel FCE corrector step. The FCE step introduces a correction on the cross-sectional area  $A_c^{\dagger}(z_{n+1}) = \Gamma A_c^*(z_{n+1})$ , and on the streamwise mass flux  $\rho u^{\dagger}(z_{n+1}) = \rho u^*(z_{n+1})/\Gamma$ , where  $\Gamma$  is a correction factor. Consequently, the specific advective accelerations, or inertial forces, undergo a change from  $\rho u^*(z_{n+1})\underline{u}^*(z_{n+1})$  to  $\rho u^{\dagger}(z_{n+1})\underline{u}^*(z_{n+1})A_c(z_{n+1})$ , such that there is no change on the (cell-)local mass flow-rate. The correction factor  $\Gamma$  takes the form

$$\Gamma = \frac{\sum_{\text{cells}} A_c(z_n)}{\sum_{\text{cells}} A_c^*(z_{n+1})}$$
(18)

In plain terms,  $\Gamma$  is a uniform correction applied for all fluid parcels or finite volume cells, which aims at preserving the size of the 1-D domain. In this context, the sum over all cross-sectional cell areas is always constant and equal to the cross-sectional

area of the confined domain,  $\sum_{\text{cells}} A_c(z_n) = \sum_{\text{cells}} A_c^{\dagger}(z_{n+1}) = \Gamma A_c^*(z_{n+1})$ . Simultaneously, this enforces streamwise constancy of cell-local and global (domain-integrated) streamwise mass flux (or alternatively, of  $U_b$ ).

All of the aforementioned operations have an advective character, and have accomplished the goal of enforcing the fixed size of the confined domain, as well as the constancy of the streamwise mass flux, such that no (wall-normal) mass fluxes occur at the domain boundaries. The cross-sectional cell areas  $A_c^{\dagger}(z_{n+1})$ , crosswise (or radial)  $v^*(z_{n+1})$ , spanwise (or tangential)  $w^*(z_{n+1})$ , and streamwise velocities  $u^{\dagger}(z_{n+1})$  can then be associated to the final flow properties of the corresponding downstream ODT domain at  $z_{n+1}$ . This is the model equivalent of the enforcement of a formal 2-D divergence condition on the velocity field. One final issue remains for the full description of the FCE step. For the u velocity component, the FCE step implies a source of momentum flux. Said source is the equivalent streamwise pressure gradient acting on the flow, which is missing from Eq. (16). To that extent, the momentum flux finally changes from  $\rho u^{\dagger}(z_{n+1})u^*(z_{n+1})$  to  $\rho u^{\dagger}(z_{n+1})u^{\dagger}(z_{n+1})$ . This modification is interpreted as the outcome of a streamwise forcing that, in the absence of a prescribed pressure gradient, should on average correspond to the physically correct FPG if the FCE step accurately represents the interaction of the confinement and CFR constraints with the flow dynamics. This is advantageous because ODT is then applicable to flows that are characterized only in terms of their prescribed bulk velocities, fluid properties, and confinement geometry. On one hand, T-ODT constant property flows are then best suited for an FPG-type of forcing in the type of confined setup at discussion here, implying the imposition of a fixed  $Re_{\tau}$  (although CFR-type forcings could also be used as in [40]). On the other hand, S-ODT confined flows are best described with CFR-type forcings, which imply the imposition of a fixed bulk Reynolds number Re<sub>b</sub> =  $2U_b\delta/\eta$ . These and other such interesting issues for discussion motivate our choice to focus on constant property flows. Notwithstanding our deliberate choice, the T-ODT and S-ODT formulations presented here can also be straightforwardly applied for flows with shear-depending, variable viscosity. Another readily obtainable extension is that of thermally coupled buoyant flows observing small temperature and density fluctuations (Boussinesq approximation). Other processes leading to dilatation such as thermal expansion could also be incorporated in the formulation in the future, by consideration of the related additional mass flux sources, further extending the applicability of the model. This completes the description of the FCE step. Numerical implementation details for the S-ODT formulation can be found in Appendix A.3. Note that additional dynamic mesh adaption operations characteristic from the dynamic grid formulation, see [22], may introduce deviations on the global integrated momentum and energy fluxes resulting from concurrent eddy event implementation and subsequent deterministic numerical integration step. Sufficient care must be exercised to that extent, as explained in Appendix A.4.

# 3 | NUMERICAL SIMULATION INPUTS: FLOW CONFIGURATION, INITIAL AND BOUNDARY CONDITIONS

We have carried out channel and pipe flow simulations using both T-ODT and S-ODT model formulations. Table 1 lists the simulated cases. The majority of the cases investigated correspond to T-ODT flows. S-ODT flows are only evaluated in cases 550CS and 550PS, which imposed  $Re_b = 20000$  and  $Re_b = 19000$  in a turbulent channel and pipe flow, respectively. The limited number of S-ODT cases is due to significantly longer simulation times (clock time) involved in the computation of several converged flow statistics. This is explained by the added complexity of the numerical advancement scheme in S-ODT, as well as the number of statistical turbulent fluxes which are evaluated for verifying the conservativeness of the numerical method, see Appendices A.3 and A.5. In this context, the S-ODT flow evaluation performed in this work only seeks an understanding of the model formulation and its features, and does not intend an extensive parametric study.

In all evaluated cases, the flow configuration is a 1-D domain which follows the sketches in Figures 1 and 2. The only BCs required are those for the velocity field  $\underline{u}$ , which are the usual no-slip conditions at the edges of the 1-D domain (walls). T-ODT simulations utilize uniform zero initial conditions for the velocity field  $\underline{u}(\xi, t = 0) = \underline{0}$ , and rely on the use of a constant forcing term  $d\overline{p}/dz$  on the momentum equation in order to impose a given  $Re_{\tau}$  (FPG forcing). Conversely, S-ODT simulations rely on the use of uniform inlet conditions  $\underline{u}(\xi, z = 0) = [0, 0, U_b]^T$ , which impose a given  $Re_b$  (CFR forcing).

**TABLE** 1 Investigated cases. Values reported as approximate are not imposed on the simulations; rather, they are estimated with the help of skin friction coefficients  $C_f$  reported from various sources of reference data [5, 6, 42, 43, 44, 45, 46, 47].

Case	m (Geometry)	$\mathrm{Re}_{ au}$	$Re_b$	T-ODT/S-ODT	$\Delta \xi_{\min}^{+}$	Forcing	$U_b^+ = \sqrt{2/C_f}$
180CT	0 (Channel)	180	≈ 5714	T-ODT	0.167	FPG	≈ 15.698
395CT	0 (Channel)	395	$\approx 14147$	T-ODT	0.166	FPG	$\approx 17.908$
550CT	0 (Channel)	550	$\approx 20000$	T-ODT	0.165	FPG	$\approx 18.382$
590CT	0 (Channel)	590	$\approx 22050$	T-ODT	0.165	FPG	$\approx 18.685$
1000CT	0 (Channel)	1000	$\approx 40000$	T-ODT	0.167	FPG	$\approx 19.666$
2000CT	0 (Channel)	2000	$\approx 87300$	T-ODT	0.167	FPG	$\approx 21.539$
5200CT	0 (Channel)	5200	$\approx 250000$	T-ODT	0.167	FPG	$\approx 24.121$
10000CT	0 (Channel)	10000	$\approx 522000$	T-ODT	0.167	FPG	$\approx 25.888$
180PT	1 (Pipe)	180	$\approx 5300$	T-ODT	0.167	FPG	$\approx 14.641$
360PT	1 (Pipe)	360	$\approx 11700$	T-ODT	0.167	FPG	$\approx 16.205$
500PT	1 (Pipe)	500	$\approx 17000$	T-ODT	0.167	FPG	$\approx 17.161$
550PT	1 (Pipe)	550	$\approx 19000$	T-ODT	0.167	FPG	$\approx 17.273$
1140PT	1 (Pipe)	1140	$\approx 44000$	T-ODT	0.167	FPG	$\approx 19.356$
2000PT	1 (Pipe)	2000	$\approx 82500$	T-ODT	0.167	FPG	$\approx 20.700$
3000PT	1 (Pipe)	3000	$\approx 133000$	T-ODT	0.167	FPG	$\approx 21.666$
6000PT	1 (Pipe)	6000	$\approx 285000$	T-ODT	0.167	FPG	$\approx 23.369$
10000PT	1 (Pipe)	10000	$\approx 509000$	T-ODT	0.167	FPG	$\approx 24.624$
550CS	0 (Channel)	$\approx 550$	20000	S-ODT	0.165	CFR	18.182
550PS	1 (Pipe)	$\approx 550$	19000	S-ODT	0.165	CFR	17.271

#### 4 CHOICE OF THE ODT MODEL PARAMETERS

Usual empiricism of turbulence models associated with model coefficients is portrayed in ODT by the sensitivity of results to the choice of the model parameters mentioned in Section 2.1.1 and 2.2.1. These are, namely,  $\alpha$ , C, and Z. In addition to these three conceptual model parameters, the parameter  $l_{\text{max}}$ , the chosen upper truncation of the eddy distribution as introduced in Section 2.1.1, may also bias the statistics resulting from the eddy event sampling procedure. Furthermore, we note that, despite not having been discussed in ODT publications so far, there is one last parameter of interest in ODT,  $A_{\text{tf}}$ , which is relevant for implementations relying on the dynamic adaptive grid strategy from [22]. The latter is precisely our case. We stress that  $A_{\text{tf}}$  is related to the numerical diffusion caused by the mesh adaption process.

In the following, we discuss first the effect of the three parameters which are theoretically relevant in the ODT formulation,  $\alpha$ , C and Z. The parameters  $l_{\text{max}}$  and  $A_{\text{tf}}$  are considered to be more closely related to numerical effects than to the conceptual formulation. As such, these are discussed later. Table 2 details all of the chosen model parameters for the geometries of interest (m = 0, m = 1).

**TABLE** 2 ODT model parameters used in numerical simulations. The values for the model parameters C and  $A_{tf}$  may be listed as  $C(Re_{\tau})$  and  $A_{tf}(Re_{\tau})$ , respectively, in the case that said parameters exhibit Reynolds number dependence (see Eq. (23), (24), and (25) in text).

m (Geometry)	T-ODT/S-ODT	$\mathrm{Re}_{ au}$	$\alpha$	C	Z	$l_{\max}$	$A_{ m tf}$
0 (Channel)	T-ODT	[180, 10000]	2/3	$C(\operatorname{Re}_{\tau})$	400	δ	25.0
0 (Channel)	S-ODT	$\approx 550$	2/3	8	800	$\delta$	25.0
1 (Pipe)	T-ODT	[180, 10000]	0	$C(\mathrm{Re}_{\tau})$	400	$2\delta/3$	$A_{\rm tf}({\rm Re}_{ au})$
1 (Pipe)	S-ODT	≈ 550	0	6	800	δ	4.0

# **4.1** | Choice of $\alpha$

As per Eq. (2) and (10), the ODT model parameter  $\alpha$  is directly related to the calculation of the kernel coefficients  $\underline{c}$  and  $\underline{b}$ , which are responsible for kinetic energy redistribution among velocity components during eddy events. We use  $\alpha = 2/3$  for our turbulent channel flow simulations. This is an *a priori* theoretical choice implying a tendency to equally redistribute extractable kinetic energy among velocity components. This is the usual choice in ODT publications relying on a vector formulation, see [32, 22, 29].

For pipe flow simulations, or alternatively, cylindrical coordinates, we resort to  $\alpha=0$ . This is also an *a priori* theoretical choice. The reasoning for this choice, which indirectly translates into a single velocity component formulation, is the following. We utilize triplet maps as a way to model turbulent advection, i.e., a convective acceleration; together with the friction and pressure forces, the convective acceleration due to turbulent advection, on the absence of mean wall-normal advection, conforms with the net (inertial) acceleration affecting the momentum component involving rectilinear motion in cylindrical coordinates (velocity component u). Conversely, a net (inertial) acceleration given by the sum of turbulent advection, friction and pressure forces, as well as centrifugal and Coriolis-like accelerations, must be considered for the radial and azimuthal momentum components in cylindrical coordinates (v and w). The centrifugal and Coriolis-like acceleration terms have been neglected so far in published cylindrical ODT formulations. Although the effect of said terms should be small for the analysis of pipe flow statistics, we retain the choice of  $\alpha=0$ , which forbids kinetic energy redistribution during eddy events, therefore constraining the entire kinetic energy (and momentum) in our pipe flows to the streamwise velocity component u. Note that this assumption relies on the utilization of uniform initial conditions for v and w of the form v=0 and w=0.

# 4.2 | Choice of Z

Since  $\alpha$  is chosen *a priori*, we consider *C* and *Z*, as the only effective ODT conceptual model parameters of interest. Recall that *C* is a proportionality coefficient for the eddy rate as per Eq. (3) and (11). Conversely, *Z* is a small eddy event suppression parameter which aims at modeling viscous effects in the eddy frequency formula, Eq. (5) and (12).

The calibration procedure for C and Z, as commented in Section 2.1.1, involves an optimization procedure relying on the minimization of the deviation of flow statistics with respect to some reference data. We consider the mean velocity profile as the reference statistical moment of velocity for the purpose of calibration. As such, we do not carry out a formal optimization procedure. Instead, we carry out a sensitivity analysis of the mean velocity profile  $u^+(y^+)$  to different selected model parameter values. From now on, we will refer to  $u^+$  as the viscous-scaled mean streamwise velocity, and to  $y^+$  as the viscous-scaled distance to the wall. Specifically,  $u^+ = \overline{u}/u_{\tau}$ , where  $\overline{u}(\xi)$  is the average streamwise velocity profile, and  $u_{\tau} = \sqrt{\tau_w/\rho}$  is the friction velocity defined with the help of the wall-shear stress  $\tau_w = \mu \left| (d\overline{u}/d\xi)_w \right|$  (the subindex w indicating quantities evaluated at the wall). Likewise,  $y^+ = (\delta - |\xi|)/\delta_{\eta}$  is defined following the configuration sketches in Figures 1 and 2, and considering  $\delta_{\eta} = \eta/u_{\tau}$  as the viscous length scale. We consider, as a naive assumption, that the mean velocity profile offers only one metric for calibration, e.g., the  $L_1$  or  $L_2$  norm of the ODT model prediction error. As a consequence, we may find several combinations of model parameters, e.g., of C and C values, which lead to similar results. Although this is not usually commented, previous unpublished work from Klein and Schmidt show an example of this issue in the context of turbulent thermal convection [48].

We performed several simulations with the goal of evaluating sensitivity to the C and Z model parameters. It is important to stress, based on findings from previous ODT publications such as [22, 26, 29], that values of C are in orders of magnitude  $\mathcal{O}(1)$ , while values of Z are usually of order  $\mathcal{O}(10^2-10^3)$  in simulated wall-bounded turbulent flows. It is also important to note that optimal C and Z values may be different between T-ODT and S-ODT formulations. While being aware that several combinations of C and Z may lead to equivalent results, we noticed that a certain choice of C yielded values of Z which could be partly justified based on theory. To that extent, we show in Figures 3a and 3b, the effect of changing Z while keeping C = 7 in T-ODT, case 590CT, on both the TKE production  $P^+$  and the mean velocity profile, respectively. Note that  $P^+ = \delta_\eta P/u_\tau^3$ , where P is the dimensional TKE production, e.g.,  $P_{\text{ODT}}$ , defined for ODT in Appendix A.5.

We focus next on an analysis for T-ODT simulations. It is remarkable that a change in Z has an almost negligible influence in the form of  $P^+$  as seen in Figure 3a. Larger values of Z only cause a shift in the profile, specifically, a shift in the peak location  $y_{\hat{p}_+}^+$ . DNS investigations have shown that  $y_{\hat{p}_+}^+ \approx 12$  in both channel and pipe flows, and that  $y_{\hat{p}_+}^+$  remains constant for most ranges of interest of  $Re_{\tau}$ , from moderate to large  $Re_{\tau}$ , see [49]. It is also worth noting that the asymptotic value of  $y_{\hat{p}_+}^+$  coincides with the asymptotic viscous coordinate on which the viscous and turbulent stresses intersect, see also [49]. Such asymptotic value for  $y_{\hat{p}_+}^+$  should be reached in our study in all investigated cases with the exception of 180CT and 180PT. This leads us to hypothesize

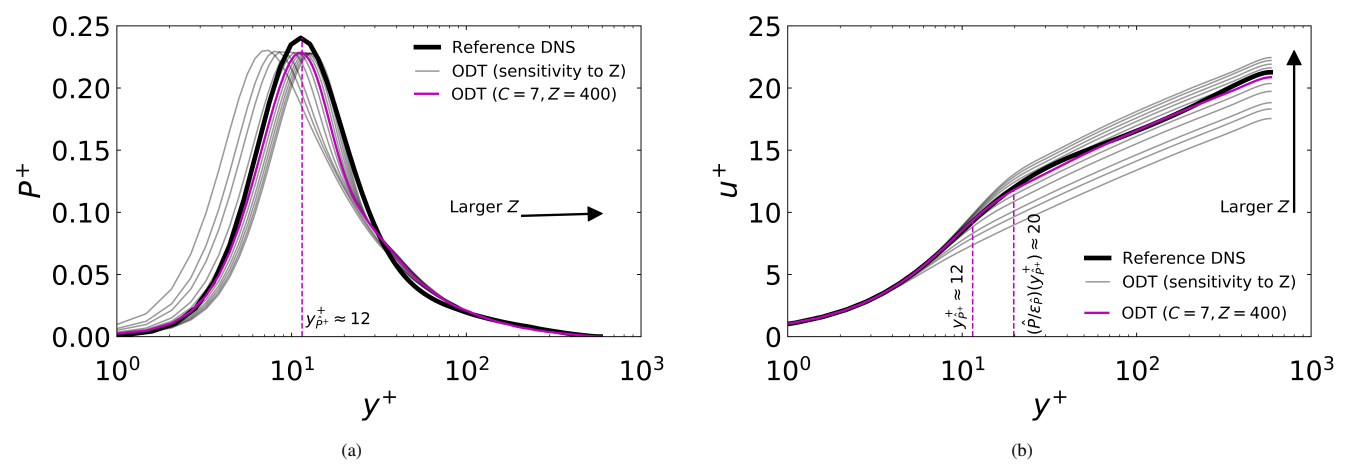


**FIGURE 3** ODT simulation results for case 590CT using values of  $Z \in \{25, 60, 100, 200, 300, 400, 500, 600, 700, 800, 900\}$  and C = 7. (a) TKE production. (b) Mean velocity profile. DNS reference data from Moser et al. [42] is also shown for comparison in both subfigures.

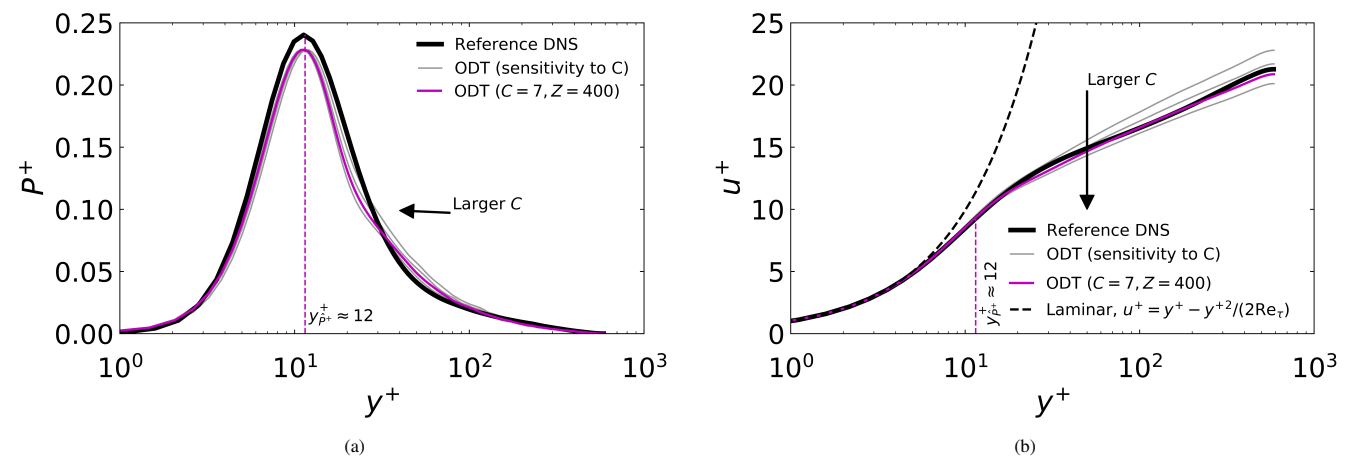


**FIGURE 4** ODT simulation results for case 590CT using values of  $C \in \{5, 6, 7, 8\}$  and Z = 400. (a) TKE production. (b) Mean velocity profile. DNS reference data from Moser et al. [42] is also shown for comparison in both subfigures.

that Z must be a Reynolds number independent parameter. It should also be the same for both channel and pipe T-ODT flows. The effect on  $P^+$  is not seen if C is changed instead of Z, see Figure 4a. Concerning the mean velocity profile, a change of Z has, on one hand, the effect of a shift in the start of the log-layer of the flow and, consequently, the form of the buffer layer; on the other hand, it shifts in a parallel way the log-layer, see Figure 3b. Conversely, changing C does not seem to modify the start of the log-layer. Instead, C seems to affect the entire outer layer of the flow, see Figure 4b. Use of C = 0 would prevent eddy event implementation in ODT, resulting in the laminar solution seen in Figure 4b. A remarkable finding concerning Z is that the optimal T-ODT value Z = 400 (obtained for C = 7 in case 590CT), yields an apparent start of the model-obtained log-layer at  $y^+ \approx 20$ . The viscous coordinate can be obtained as the product  $(\hat{P}/\varepsilon_{\hat{P}})y_{\hat{P}_{\hat{P}}}^+ \approx 20$ , where  $(\hat{P}/\varepsilon_{\hat{P}})$  is the ratio of TKE production to TKE dissipation at the location of peak TKE production. The latter should also be fairly Reynolds number insensitive, and it seems to be around  $5/3 < \hat{P}/\varepsilon_{\hat{P}} < 7/4$ , at least according to the information presented in [43, 5]. The model parameter Z is a viscous penalty coefficient; as such, it is related to the TKE dissipation and viscosity. Thus, it is no surprise that it is connected to the log-law form and potentially to the ratio  $\hat{P}/\varepsilon_{\hat{P}}$ . As commented in previous ODT publications such as [40], Z has the form of the square of a Reynolds number, see also Eq. (5). In this context, it is truly remarkable that the optimal value of Z is precisely  $Z = \left[(\hat{P}/\varepsilon_{\hat{P}})y_{\hat{P}_{\hat{P}}}^+\right]^2$  such that this coincides also with the square of the viscous coordinate (i.e., a local Reynolds number) of the

apparent start of the model-obtained log-layer. Based on this reasoning, we fix the value  $Z = 20^2 = 400$  according to the before mentioned Reynolds number independent estimate, see Table 2.

The previous theoretical rationale is applicable to T-ODT flows, and in particular to Eq. (5). The value of Z in S-ODT flows should be motivated by a similar logic, although the role of Z in S-ODT is slightly different according to Eq. (12), since fluxes due to streamwise advection are considered for the calculation of the representative eddy streamwise length scale. We do not elaborate further on this issue, since we consider it out of scope for this work. As noted, we do not perform an extensive number of S-ODT simulations due to their significantly longer simulation clock times. We only note the following for the S-ODT cases 550CS and 550PS. Using a slightly larger value of C in comparison to T-ODT, a good value of C is C is C in the S-ODT formulation, see Table 2.

#### **4.3** | Choice of *C*

We now comment on the choice of C, the related proportionality coefficient for the eddy rate, also in the context of T-ODT flows. A better visualization of the effect of the C model parameter is seen on the mean velocity profile shown with linear axes in Figure 5a. Intuitively, C seems to be related to the associated value of  $U_b$ , the domain-averaged velocity. This is our rationale for determining the optimal value of C, once Z is fixed as commented before. For all T-ODT cases in Table 1, we fixed Z and then determined which value of C yielded the best match for the skin friction coefficient  $C_f = 2/U_b^{+2}$ , or conversely, of the viscous-scaled bulk velocity  $U_b^+$ . To that extent, C was changed unit-wise between simulations in the range C = 3 to C = 10. An improved estimate was obtained by an interpolation between unit-wise values, i.e., the interpolation yielding the exact  $C_f$  for the given  $Re_\tau$ . We stress that the values of  $C_f$  and  $U_b^+$  for every case in Table 1 were obtained from various sources, ranging from DNS data at low to moderate Reynolds numbers, to experimental correlations for large Reynolds numbers [5, 6, 42, 43, 44, 45, 46, 47]. Figure 5b shows different reference DNS values for  $U_b^+$  as a function of  $Re_\tau$ , as well as the following power law regressions which we have obtained for said reference values,

Channel flow 
$$U_b^+ = 7.579 \text{Re}_{\tau}^{0.141} \quad \text{Re}_{\tau} < 2000$$
 (19)

Pipe flow 
$$U_b^+ = 6.617 \text{Re}_{\tau}^{0.153} \quad \text{Re}_{\tau} < 2000$$
 (20)

We choose the threshold  $\text{Re}_{\tau} = 2000$  to distinguish scaling laws for low and large  $\text{Re}_{\tau}$ . In this context, Figure 5b also shows the log-law fits obtained for  $C_f$  (and consequently for  $U_b^+$ ) in the studies from Zanoun et al. [45] and Pirozzoli et al. [6], for turbulent channel and pipe flows, respectively. These fits are defined for large Reynolds numbers, specifically, for  $\text{Re}_{\tau} \geq 2000$ ,

$$U_b^+ = 2.711 \ln |\text{Re}_\tau| + 1$$
, Channel flow fit obtained by [45]  $\text{Re}_\tau \ge 2000$  (21)

$$U_b^+ = 5.945 \log_{10} |\text{Re}_{\tau}| + 1.227$$
, Pipe flow fit obtained by [6]  $\text{Re}_{\tau} \ge 2000$  (22)

When fixed values of Z and C are maintained across  $Re_{\tau}$ , e.g., choosing C=7 and Z=400 in channels, or C=5 and Z=400 in pipe flows, this leads to deviations in the predicted value of  $U_b^+$  when comparing with reference data, as seen in Figure 5b. Since we choose to keep Z fixed due to partly theoretical justifications, it is necessary to adjust C as a function of  $Re_{\tau}$ , in order to predict the correct  $U_b^+$ . Having said that, Figure 6 shows precisely the necessary changes in C required in order to correctly predict  $U_b^+$ . We fit two power laws for  $C(Re_{\tau})$ , in order to characterize the low-to-moderate Reynolds number range  $180 \le Re_{\tau} < 2000$  and the large Reynolds number range  $Re_{\tau} \ge 2000$ . For T-ODT channels and T-ODT pipe flow simulations, these are,

T-ODT channel flow 
$$C(\text{Re}_{\tau}) = \begin{cases} 2.750 \text{Re}_{\tau}^{0.133} & 180 \le \text{Re}_{\tau} < 2000 \\ 6.666 \text{Re}_{\tau}^{0.013} & \text{Re}_{\tau} \ge 2000 \end{cases}$$
 (23)

T-ODT pipe flow 
$$C(\text{Re}_{\tau}) = \begin{cases} 1.535 \text{Re}_{\tau}^{0.174} & 180 \le \text{Re}_{\tau} < 2000 \\ 3.742 \text{Re}_{\tau}^{0.047} & \text{Re}_{\tau} \ge 2000 \end{cases}$$
 (24)

Two interesting issues can be analyzed from Eq. (19-22) and (23-24). First, there is no meaningful change in C for large Reynolds numbers in T-ODT flows. That is, C remains approximately constant for  $Re_{\tau} \geq 2000$ , as seen in Figure 6. Second, the power law exponents for the dependence of C on  $Re_{\tau}$  for low to moderate Reynolds numbers are relatively close to the power law exponents for  $U_b^+$  in the same Reynolds number range. This supports our hypothesis regarding potential correlations between C and the skin friction coefficient  $C_f$  for T-ODT channel and pipe flows.

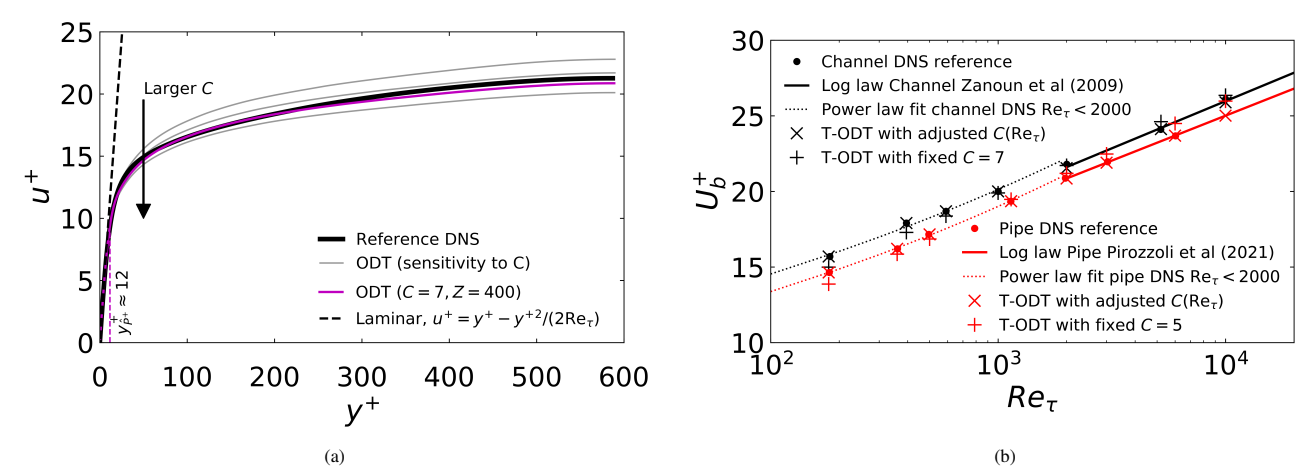


**FIGURE 5** (a) T-ODT simulation results for the mean velocity profile of case 590CT using values of  $C \in \{5, 6, 7, 8\}$  and Z = 400. DNS reference data from Moser et al. [42] is also shown for comparison. (b) Viscous-scaled bulk velocity  $U_b^+$  evaluated with different choices of the T-ODT model parameter C, either by adjusting it to coincide with reference data for  $U_b^+$  or by keeping it fixed. DNS reference data from various sources [5, 6, 42, 43, 44, 45, 46, 47] is shown for reference. Power-law fits of the DNS reference data for  $Re_{\tau} < 2000$ , see Eq. (19) and (20) and log-law fits for  $Re_{\tau} \ge 2000$  according to Eq. (21) and (22), are also shown for reference for both channel and pipe flow configurations.

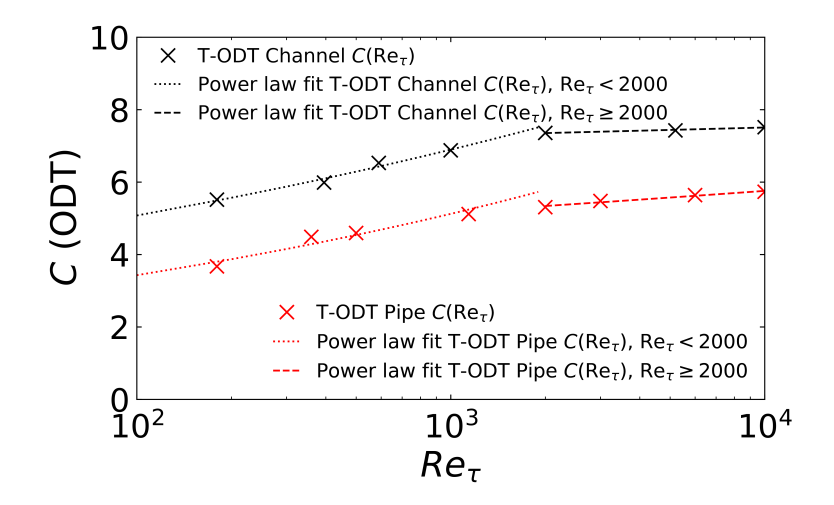


**FIGURE 6** Required values for ODT model parameter C as a function of  $Re_{\tau}$  for appropriate prediction of  $U_b^+$  in statistically steady turbulent channel and pipe flows. The figure also shows the corresponding power law fits for turbulent channel and pipe flows, according to Eq. (23) and (24), respectively.

Due to the limited number of S-ODT cases evaluated, we can not comment extensively on the choice of C for S-ODT flows. To that extent, the chosen values for C from Table 2 are simply those values, which upon use of  $Z = 2\left[(\hat{P}/\varepsilon_{\hat{P}})y_{\hat{P}^+}^+\right]^2 \approx 800$ , yield the adequate value of  $U_b^+$  according to reference data.

# 4.4 Numerical effects associated with the choice of $l_{\text{max}}$

The choice of a large upper bounding value for the presumed eddy event PDF  $\phi_l^*$ , see Section 2.1.1, may lead to the occasional sampling of very large eddy events which would exceed the momentum thickness of the flow. This disproportionately affects

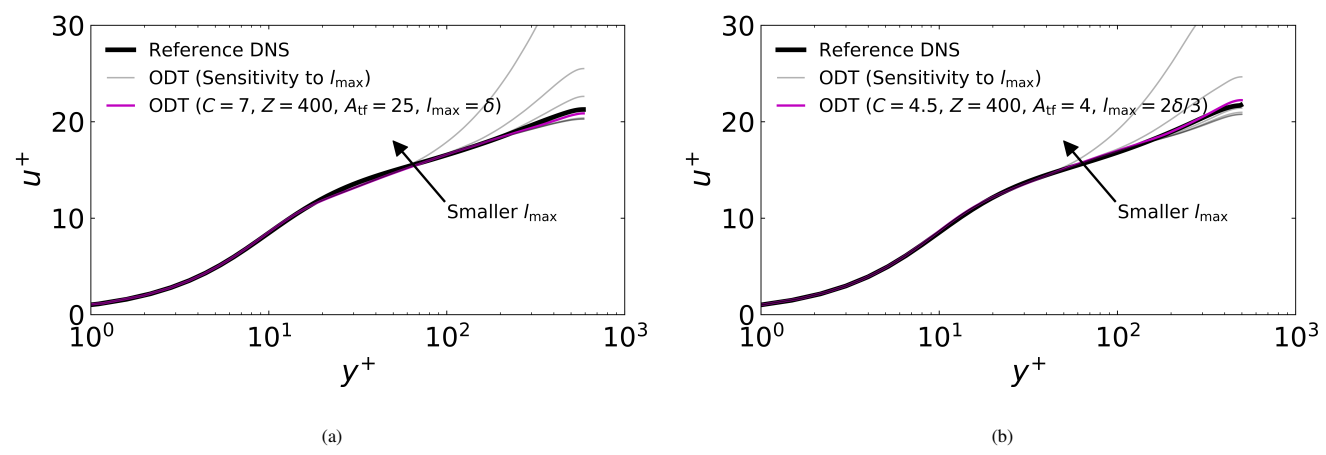


FIGURE 7 (a) Effect of eddy size distribution truncation parameter  $l_{\text{max}}$  on the mean velocity profile of a turbulent channel flow, case 590CT. Effects are shown for  $l_{\text{max}}/(2\delta) \in \{0.1, 0.2, 0.3, 0.5, 0.7, 0.9, 1\}$ . Reference DNS data from [42] is also shown for comparison. (b) Effect of eddy size distribution truncation parameter  $l_{\text{max}}$  on the mean velocity profile of a turbulent pipe flow, case 500PT. Effects are shown for  $l_{\text{max}}/(2\delta) \in \{0.1, 0.2, 1/3, 0.5, 0.7, 0.9, 1\}$ . Reference DNS data from [6] is also shown for comparison.

turbulent transport, specially in the outer layer, see [32]. Previous studies have suggested fixed values for  $l_{\text{max}} \leq \delta$ , which, together with optimal values for other ODT model parameters such as C, seem to yield a reasonable representation of the outer layer, see [35, 41].

Sensitivity tests carried out within this work showed that the qualitative influence of  $l_{\text{max}}$  on the mean velocity profiles was generally the same for all Reynolds numbers evaluated. As shown in Schmidt et al.[35],  $l_{\text{max}}$  affects the mean velocity profiles for channel flows in the outermost region from the wall. This parameter was estimated to have an optimal value of  $\delta$  in [35]. Krishnamoorthy [41] also verified the influence of  $l_{\text{max}}$  on T-ODT pipe flows, estimating an optimal value of  $2\delta/3$ . For consistency reasons, we use the same *a priori* optimal  $l_{\text{max}}$  values for T-ODT flows found in [35, 50, 41]. Qualitatively,  $l_{\text{max}}$  has the same impact in both the T-ODT and S-ODT channel and pipe flow configurations. Generally speaking, larger values of  $l_{\text{max}}$  promote more mixing close to the centerline, thus resulting in a flatter velocity profile near the centerline. Figures 7a and 7b show the effect of different values of  $l_{\text{max}}$  on the mean velocity profile for T-ODT channel and pipe flows.

Although not shown here, we have also verified that the *a priori* choice of  $l_{\text{max}} = \delta$  is appropriate in both S-ODT channel and pipe flows in order to obtain reasonable mean flow statistics. Thus, we obtain better results in the S-ODT cylindrical formulation using  $l_{\text{max}} = \delta$  in comparison to the T-ODT cylindrical choice of  $l_{\text{max}} = 2\delta/3$ . The choice  $l_{\text{max}} = \delta$  also has the conceptual advantage that it is the most physically intuitive one for the upper truncation of the presumed eddy event PDF.

# 4.5 Numerical effects associated with the choice of $A_{tf}$

We remark that the deterministic catch-up process, which is characteristic of ODT, occurs every time an eddy event is implemented. Additionally, deterministic catch-ups also occur after a relatively large amount of sampled increments are taken, which amount to the magnitude of the step size given by the CFL criterion for explicit (time- or streamwise-) numerical integration. This follows the operator split logic between the implementation of viscous effects and of turbulent advection in ODT. In dynamically adaptive grid simulations, the (non-dimensional) parameter  $A_{tf}$  works as a switch for mesh adaption after sufficient time (or streamwise distance) has elapsed without eddy events being implemented. In plain terms,  $A_{tf}$  refers to the number of CFL-determined step sizes taken, without any eddy event implementation and only performing deterministic advancement, before a procedure for mesh adaption takes place as detailed in [22].

Before proceeding with the discussion, we note the following considerations. First, it is more likely that successive deterministic catch-ups occur at lower Reynolds number flows in comparison to larger Reynolds number flows, since fewer turbulent eddies are expected at the former. Second, the T-ODT eddy frequency distribution  $(\Delta t_l)^{-1}$ , or the alternative S-ODT eddy streamwise number distribution  $(\Delta z_l)^{-1}$ , exhibits lower values in the region around  $\xi = 0$  due to (in average) smaller velocity gradients and

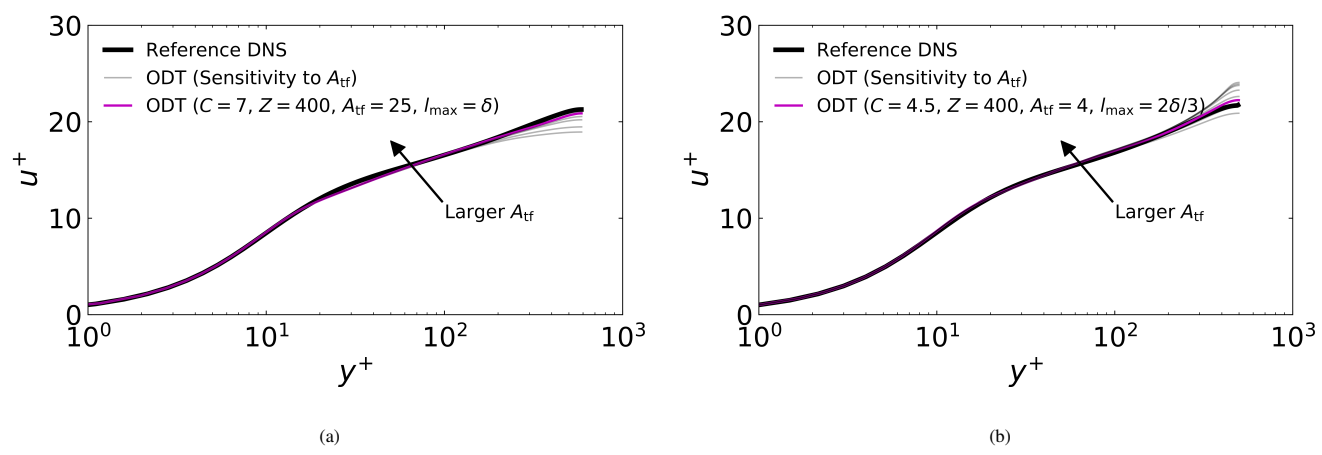


**FIGURE 8** (a) Effect of mesh adaption control parameter  $A_{tf}$  on the mean velocity profile of a turbulent channel flow, case 590CT. Effects are shown for  $A_{tf} \in \{1, 2, 5, 10, 25, 50, 100\}$ . Reference DNS data from [42] is also shown for comparison. (b) Effect of mesh adaption control parameter  $A_{tf}$  on the mean velocity profile of a turbulent pipe flow, case 500PT. Effects are shown for  $A_{tf} \in \{1, 2, 4, 5, 10, 25, 50, 100\}$ . Reference DNS data from [6] is also shown for comparison.

larger streamwise velocity values away from the wall. That is, on average, fewer eddies are sampled in regions away from the wall in comparison to near-wall regions. These considerations imply that the mesh adaption process, and correspondingly,  $A_{\rm tf}$ , have a larger numerical impact around the centerline and/or at low Reynolds numbers.

Operationally, we can define  $A_{tf}$  as a ratio between the characteristic scale for adaption of the numerical domain  $\Delta t_A$  or  $\Delta z_A$ , and the CFL-determined step size (due to diffusion) for explicit numerical integration  $\Delta t_{CFL}$  or  $\Delta z_{CFL}$ , for T-ODT and S-ODT, respectively. Specializing to T-ODT, the mesh adaption procedure should be called if we exceed a threshold  $\Delta t_A > A_{tf} \Delta t_{CFL}$ . In order to achieve statistical similarity across Reynolds numbers in the outer layer of the flow, that is, the flow region most affected by mesh adaption, it is appropriate to scale  $\Delta t_A$  as  $\delta / u_\tau$ . Conversely,  $\Delta t_{CFL}$  is equal or closely proportional to  $\delta_\eta^2 / \eta$ , where  $\delta_\eta$  is the viscous length-scale (comparable to the Kolmogorov length-scale in wall-bounded flows) required for appropriate representation of the entire turbulence length-scale bandwidth. Following this logic,  $A_{tf} = \Delta t_A / \Delta t_{CFL}$  scales linearly with Re $_\tau$ , at least for the alleged sensitive low Reynolds number flows. In this way, it is possible to relate the values of two different factors  $A_{tf,1}$  and  $A_{tf,2}$  potentially associated with two different (low) Reynolds number flows Re $_{\tau,1}$  and Re $_{\tau,2}$ ,

$$A_{tf,2} = A_{tf,1} \frac{Re_{\tau,2}}{Re_{\tau,1}}$$
 (25)

Figures 8a and 8b show the influence of  $A_{\rm tf}$  for channel and pipe flow T-ODT simulations. Qualitatively, the effect of increasing  $A_{\rm tf}$  is similar to that of decreasing  $l_{\rm max}$ , and similar to  $l_{\rm max}$ , the effect is largest close to the centerline. The effect seems to be mostly relevant for cylindrical pipe flows. We find the value  $A_{\rm tf} = 4$  suitable for pipe flows at  $Re_{\tau} \approx 500$  (case 500PT) when the previously discussed optimal values of C and C are simultaneously used, see Figure 8b. For channel flows, we work with a larger value,  $A_{\rm tf} = 25$ , which makes channel flows less sensitive to mesh adaption related issues. We attribute the scaling sensitivity in ODT pipe flows to the characteristic radial stretching of the cylindrical system. The procedure for mesh adaption described in [22] is based on an equal redistribution of arcs formed by property profiles. This may be inaccurate in cylindrical coordinates due to the intrinsic stretching or r-weighting of property and flow profiles.

Figures 9a and 9b show the different contributions to the total stress in T-ODT channel (590CT) and pipe flows (500PT), respectively, determined as indicated in Appendix A.5. Similarly, Figures 10a and 10b show the stress contributions in S-ODT channel (550CS) and pipe flows (550PS). In this context, the sum  $\overline{M_3}^+ + \overline{T_3}^+$  is equivalent to  $\overline{M_3}^+ + \overline{K_3}^+$  as per Eq. (2), and refers to the (viscous scaled) eddy event related contributions to streamwise momentum, including the kernel modification procedure. This represents the model surrogate for the Reynolds shear stress gradient in T-ODT  $\partial \overline{u'v'}^+/\partial y^+$ . The term  $\overline{D_3}^+$  is the streamwise momentum contribution due to the deterministic numerical integration step. For T-ODT, this represents the sum of the FPG and the viscous term,  $\operatorname{Re}_{\tau}^{-1} + \partial^2 u^+/\partial y^{2,+}$ , while in S-ODT, this is simply the viscous term  $\partial^2 u^+/\partial y^{2,+}$ . The terms  $\overline{A_3}^+$  and  $\overline{F_3}^+$  refer to

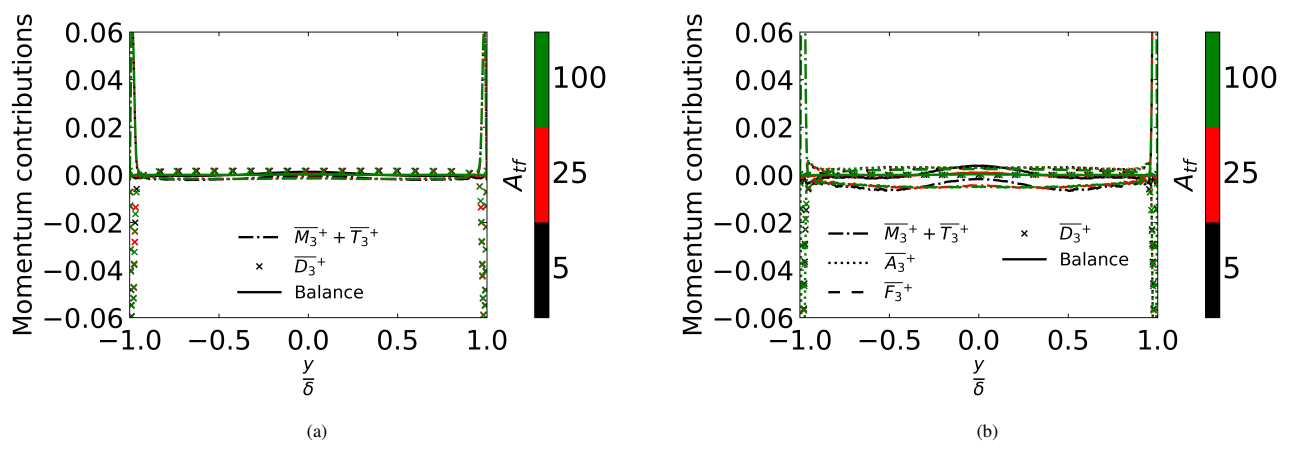


**FIGURE 9** (a) Momentum contributions for the statistically stationary T-ODT turbulent channel flow, case 590CT. (b) Momentum contributions for the statistically stationary T-ODT turbulent pipe flow, case 500PT.

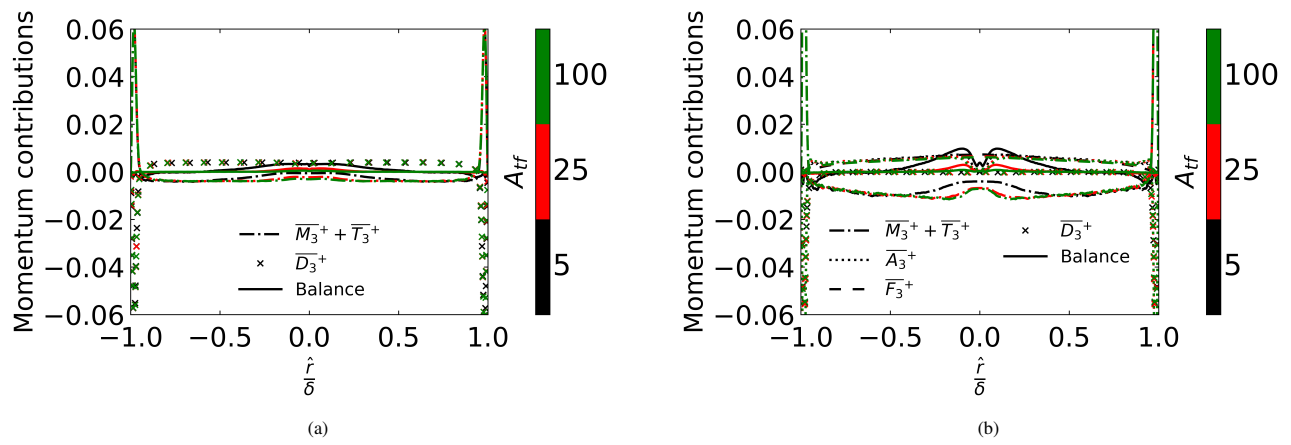


**FIGURE 10** (a) Momentum contributions for the statistically stationary S-ODT turbulent channel flow, case 550CS. (b) Momentum contributions for the statistically stationary S-ODT turbulent pipe flow, case 550PS.

the advective and source-like contributions to momentum derived from the FCE step, as discussed in Section 2.2.3, see also Appendix A.5. The sum  $\overline{M_3}^+ + \overline{T_3}^+ + \overline{A_3}^+$  corresponds to the S-ODT model surrogate for the Reynolds shear stress gradient.

In statistically steady T-ODT flows, the advective contributions  $\overline{M_3}^+ + \overline{T_3}^+$  and deterministic contributions  $\overline{D_3}^+$  should balance each other, up to numerical accuracy. For S-ODT flows, the balance is between advective contributions  $\overline{M_3}^+ + \overline{T_3}^+ + \overline{A_3}^+$ , viscous contributions  $\overline{D_3}^+$  and source-like contributions  $\overline{F_3}^+$ . These balances also evidence the *conservativeness* of the numerical method. Nonzero numerical balances (or imbalances) seen in Figures 9a-10b are attributable to numerical diffusion effects due to mesh adaption, in this case represented by  $A_{tf}$ . The cylindrical formulation is more sensitive to numerical diffusion due to the grid adaption procedure. Similarly, the S-ODT formulation experiences much larger numerical diffusion due to  $A_{tf}$  in comparison to the T-ODT formulation. The larger S-ODT numerical diffusion due to grid adaption is explained by the current failure of the S-ODT mesh adaption procedure for simultaneous conservation of streamwise mass flux, momentum flux and energy flux in confined domains, see also Appendix A.4. The numerical diffusion is reduced for larger values of  $A_{tf}$ , that is, less frequent re-gridding. Since values of  $A_{tf}$  increase for larger Reynolds number flows as per Eq. (25), it is expected that the numerical diffusion effect is also reduced for larger Re<sub>T</sub>.

We note the following after evaluation of both the mean flow statistics per Figures 8a-8b, and of the numerical conservativeness per Figures 9a-10b. It is not possible to reconcile the best reasonable matching of the mean flow, e.g., the mean velocity profile,

with appropriate numerical balance when the dynamic mesh adaption procedure is used in the T-ODT or S-ODT cylindrical formulations (we do not show the S-ODT equivalent figures to 8a-8b here). A modification of the cell-merging operation during mesh adaption is required. The issues are discussed in Appendix A.4, although remediation of said issues is out of scope in this work.

All numerical simulation results to be presented next, unless otherwise noted, use calibrated values of  $A_{tf}$  which yield the best achievable mean flow statistics. For the cylindrical T-ODT formulation, the calibrated values of  $A_{tf}$  scale as in Eq. (25) for  $Re_{\tau} < 2000$ , using the reference value  $A_{rf,1} = 4$  at  $Re_{\tau,1} = 500$ . The scaling range is chosen to correspond with the same one of the model parameter C. All relevant ODT parameter values are listed in Table 2. In the cylindrical T-ODT and S-ODT formulations, the chosen values of  $A_{tf}$  yield non-negligible numerical diffusion which translates into numerical flux imbalances, as seen in Figures 8a-8b, 9a-10b. Although the imbalances are small for  $A_{tf} = 4$  in the cylindrical T-ODT formulation at low Reynolds numbers, they are quite large in the cylindrical S-ODT formulation (case 550PS). Selected results using large values of  $A_{tf}$  which ensure numerical flux balancing for cases 550PT and 550PS can be found in Appendix B.1.

# 5 | NUMERICAL SIMULATION RESULTS

# 5.1 First order statistics (mean flow statistics)

We comment now on the usual mean flow statistics obtained with the calibrated ODT model parameters listed in Table 2. T-ODT model results for the mean flow velocity profile of turbulent channel and pipe flow simulations are shown in Figure 11a with comparison to reference DNS data. In all cases, there is good agreement between ODT model results and DNS reference data. T-ODT model results for turbulent channel flow, specifically, exhibit, qualitatively, the best agreement among all layers of the mean velocity profile, and across all of the different evaluated  $Re_{\tau}$ . In general, it is noted that T-ODT performs best throughout the viscous sublayer and, seemingly, the logarithmic layer of turbulent channel flows (a linear profile is obtained for large  $y^+$  in the semi-logarithmic plot for T-ODT turbulent channel flows).

Figure 11b shows a comparison of the mean velocity profile at the relatively low  $Re_{\tau} = 550$  case, utilizing both T-ODT and S-ODT model formulations. The agreement between both temporal and spatial formulations, and between model results and DNS data is remarkable. As suggested by the theory and DNS data, the region of the outer layer of the mean flow closest to  $\xi = 0$  in the turbulent channel, is slightly different from that in the turbulent pipe at the relatively low  $Re_{\tau} = 550$ . This is most likely due to the curvature effects associated with the cylindrical diffusion operator, which is still relevant for relatively low Reynolds number flows. This feature is captured in both T-ODT and S-ODT model results as evidenced when comparing with DNS reference data.

We now comment on some observations which motivated the choice of the ODT model parameter Z in Section 4.2. Indeed, we previously commented that the optimal choice of Z yields a peak location  $y_{\hat{p}^+}^+$  which coincides with the large  $Re_{\tau}$  asymptotic value  $y_{\hat{p}^+}^+ \approx 12$ . In fact, at large  $Re_{\tau}$ , said value  $y_{\hat{p}^+}^+$  also coincides with the viscous intersection coordinate  $y^+$  at which the (scaled) viscous and turbulent stress are equal (both taking a value of 0.5). In order to illustrate this issue, we show in Figures 12a and 12b, the viscous stress, turbulent stress, and TKE production profiles at two very different  $Re_{\tau}$  of 550 and 10000, for turbulent channel and pipe flows. As before, the TKE production is defined for ODT according to Appendix A.5. Note that due to numerical imbalances which may occur by the choice of specific values of  $A_{tf}$  as explained in Section 4.5, we do not evaluate here the Reynolds shear stress by numerical flux balancing as per Appendix A.5. Instead, we determine  $\overline{u'v'}_{bal}(\xi)$  by the mean momentum balance of the statistically steady RANS turbulent channel or pipe flow equation. That is,

$$\overline{u'v'}_{\text{bal}}(\xi) = \frac{1}{\xi^m} \left[ \left( -\frac{1}{\rho} \frac{d\overline{\rho}}{dz} \right) \left( \frac{\xi^{m+1} - (-\delta)^{m+1}}{m+1} \right) + \xi^m \eta \frac{d\overline{u}}{d\xi} - (-\delta)^m \frac{\tau_w}{\rho} \right]$$
(26)

In T-ODT, the pressure gradient  $d\bar{p}/dz$  for use in Eq. (26) is the corresponding FPG. Conversely, for S-ODT, the equivalent pressure gradient is determined by the resulting  $\tau_w$  in a simulation, i.e., by the additional symmetric solution constraint  $\overline{u'v'}_{bal}(\xi=0)=0$  in the same Eq. (26).

According to Figures 12a and 12b, all ODT model results (T-ODT and S-ODT) yield a TKE production peak at approximately  $y_{P^+}^+ \approx 12$ , coinciding with the intersection of the turbulent and viscous stress, which we note as the viscous coordinate  $y_{vr}^+$ . Results for other intermediate values of Re $_{\tau}$  different from 550 and 10000 are similar, and are not shown here. Due to the reasonable agreement obtained between ODT and DNS mean flow velocity profiles, it is not a surprise that the ODT viscous stress profiles also exhibit good agreement when compared with DNS reference data. Perhaps more illustrative is the representation

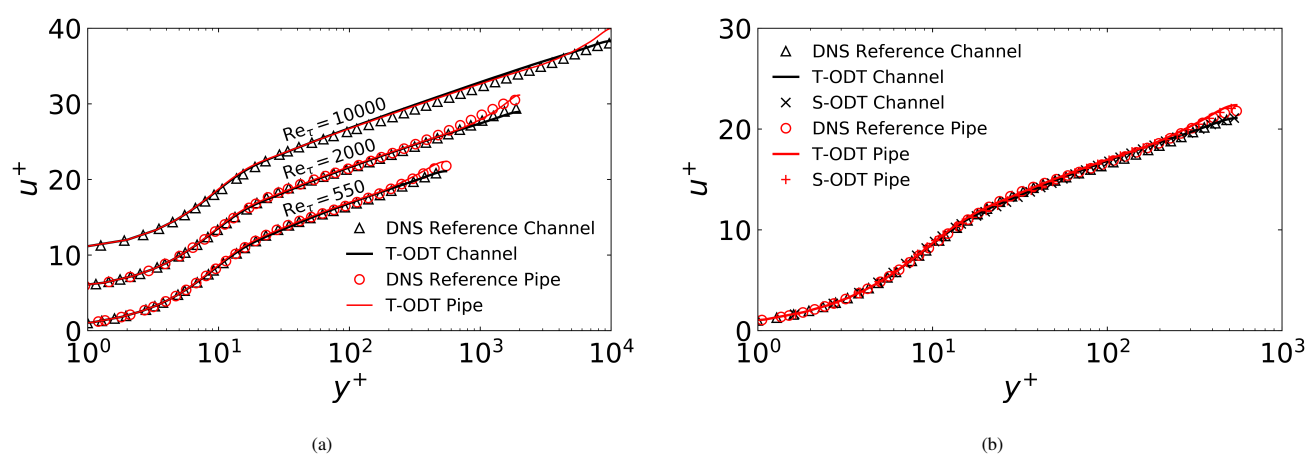


**FIGURE 11** (a) T-ODT mean velocity profiles for turbulent channel and pipe flow simulations (Cases 550CT, 550PT, 2000CT, 2000PT, 10000CT, and 10000PT). The profiles at larger  $Re_{\tau}$  are shifted upward 5 viscous units for better visualization. (b) T-ODT and S-ODT mean velocity profiles for turbulent channel and pipe flow simulations at  $Re_{\tau} = 550$  (Cases 550CT, 550CS, 550PT, and 550PS). DNS turbulent channel flow data from [5, 7], as well as DNS turbulent pipe flow data from [46, 6] are shown for reference. Note that there is no DNS reference data for turbulent pipe flow at  $Re_{\tau} = 10000$ .

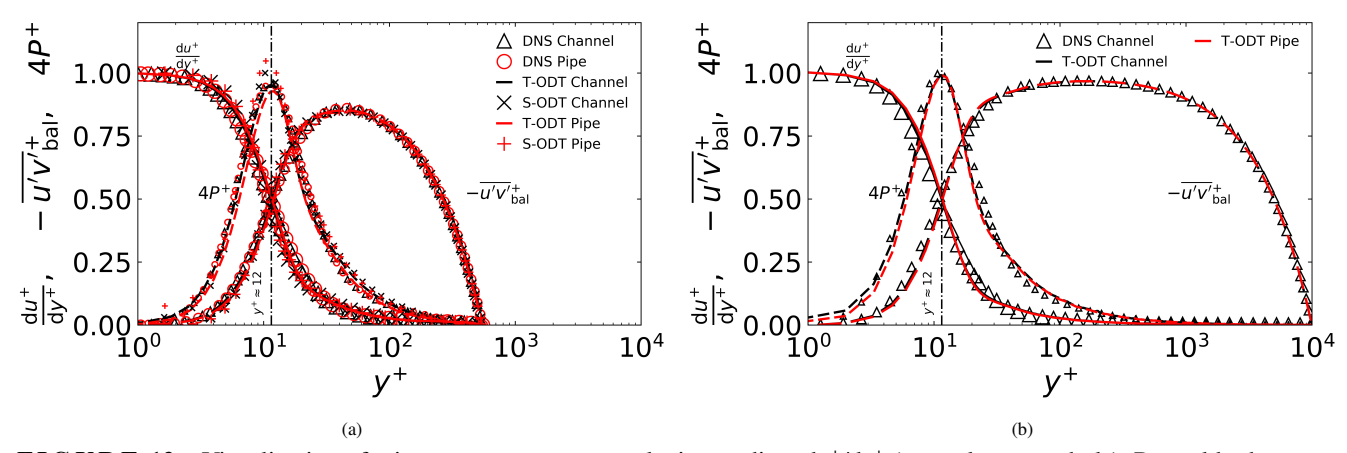


**FIGURE 12** Visualization of: viscous stress or mean velocity gradient  $du^+/dy^+$  (——, large symbols), Reynolds shear stress  $\overline{u'v'}_{bal}^+$  (——— medium-sized symbols), and TKE production  $P^+$  (——, small symbols), all scaled in viscous units. The TKE production is shown multiplied by 4 for better visualization. With the exception of the S-ODT peak  $P^+$ , essentially all data values overlap with the DNS data in the different profiles shown. DNS turbulent channel flow data from [5, 7], as well as DNS turbulent pipe flow data from [46] are shown for reference. Note that there is no DNS reference data for turbulent pipe flow at Re<sub> $\tau$ </sub> = 10000. The viscous coordinate  $y^+$  = 12 is also indicated with a vertical line · · · · · · · for reference. (a) Re<sub> $\tau$ </sub> = 550 (Cases 550CT, 550CS, 550PT, 550PS). (b) Re<sub> $\tau$ </sub> = 10000 (Cases 10000CT and 10000PT).

of the Reynolds shear stress  $\overline{u'v'}_{\text{bal}}^+$  seen in Figures 12a and 12b. Clearly, the ODT Reynolds stress representation for both turbulent channel and pipe flows is very good, adequately reproducing the DNS data. Interestingly enough, the T-ODT pipe flow representation of the TKE production converges to that of the T-ODT channel flow at larger Re<sub>\tau</sub>, similar to how DNS statistics of statistically steady turbulent channel and pipe flows converge for larger Re<sub>\tau</sub>. For all cases, regardless of the (T-ODT or S-ODT) model formulation, the TKE production representation agrees well with DNS data, although S-ODT model results slightly overshoot the peak value  $\hat{P}^+$  at the evaluated Re<sub>\tau</sub>  $\approx 550$ .

Next, we discuss the evidence related to the presence of a logarithmic layer in the ODT model results. Usually, the logarithmic law results from the integration of a dimensionless function  $\Phi(y^+, \mathrm{Re}_b)$  related to the velocity gradient by  $\mathrm{d}u^+/\mathrm{d}y^+ = (1/y^+)\Phi(y^+,\mathrm{Re}_b)$ . As  $y^+ \to \infty$  and  $\mathrm{Re}_b \to \infty$ , to a finite limit,  $\Phi(y^+,\mathrm{Re}_b)$  tends to the limiting value  $\Phi(\infty,\infty) = 1/\kappa$ , where  $\kappa$  is the von Kármán constant (usually taken as  $\kappa \approx 0.4$ ). The universal logarithmic law follows then from direct integration, see [51]. The product term  $y^+\mathrm{d}u^+/\mathrm{d}y^+$  is known as the indicator function. If the similarity hypothesis for  $\Phi$  holds, then there should be a region in  $y^+$  along which the indicator function converges to the value  $1/\kappa$ . We show the form of the indicator function for different  $\mathrm{Re}_{\tau}$  in Figures 13a and 13b, in inner and outer coordinate scalings, respectively. Note that inner scaling coordinates are denoted by  $0 \le y^+ \le \mathrm{Re}_{\tau}$ , while outer scaling coordinates are denoted by  $0 \le (\delta - |\xi|)/\delta \le 1$ , or by the equivalent  $0 \le y^+/\mathrm{Re}_{\tau} \le 1$ .

In DNS, the indicator function achieves a local minimum or plateau in inner-scaled coordinates, a region of constant  $1/\kappa$ , most notably at large  $Re_{\tau}$  for  $y^+ > 60$ . This more or less coincides with the usually recognized start of the range of the log-law, see [12]. This is true for both turbulent channel and pipe flows. Notably, turbulent pipe flows exhibit less of a region of constant  $1/\kappa$ . Comparison with outer-scaled quantities confirms that there is indeed an approximate constancy of the indicator function, also around the value  $1/\kappa$  for all Reynolds numbers evaluated. For channel flows, the constancy at  $1/\kappa$  ends approximately at  $y^+/Re_{\tau} \approx 0.8$ , while the pipe flow range is shorter, ending approximately at  $y^+/Re_{\tau} \approx 0.3$  for all Reynolds numbers evaluated, see Figure 13b. We can claim that, overall, ODT turbulent channel flows exhibit a significantly longer logarithmic region in comparison to the ODT turbulent pipe flows, similar to how DNS data of turbulent channel flows seem to exhibit a longer plateau in comparison to DNS data of turbulent pipe flows. There are also no meaningful differences in the log-law representation between T-ODT and S-ODT model results. Note that the clearest region of  $1/\kappa$  constancy, as well as agreement of the ODT indicator function results with DNS is obtained for the turbulent channel flow results at  $Re_{\tau} = 10000$ . This is an indication that the model performance improves with increasing  $Re_{\tau}$ , and that the asymptotic logarithmic law is also most appropriate at large  $Re_{\tau}$ .

Note that T-ODT results for large  $Re_{\tau}$ , as well as S-ODT results in Figures 13a and 13b exhibit relatively large fluctuations away from the wall. This is merely a result of insufficient averaging at the corresponding  $Re_{\tau}$ . Indeed, part of the inherent cost of ODT is the relatively large number of ensemble members (in our case, large averaging time or large averaging streamwise distance) required for converged statistics. Since this has no meaningful consequences in our analysis, we show the profiles with the inherent fluctuations for illustrative purposes.

The region of largest disagreement seen in Figure 13b may be associated with the outer layer of the flow. This may be a confusing result given the relatively good match between ODT and DNS data in Figures 11a, 11b, 12a, and 12b. However, note that all of the before mentioned figures are shown as semi-logarithmic plots in which small errors are not that apparent. Errors in the mean velocity gradient are also scaled up away from the wall, when a multiplication by the position takes place, such as in the indicator function formula. The fact that the outer layer of the flow is not well represented in ODT at low or moderate  $Re_{\tau}$  is to be expected, since the outer layer is dominated by large-scale, non-universal, bulk three-dimensional motion. This cannot be easily captured by the reduced one-dimensional representation of the ODT model.

We now comment on the form of the model-obtained turbulent viscosity. To that extent, we recall the Boussinesq hypothesis for turbulent flow, which defines the Reynolds shear stress in terms of the mean velocity gradient. In this context, the turbulent viscosity can be defined as

$$\eta_t \equiv -\frac{\overline{u'v'}_{\text{bal}}}{\frac{d\overline{u}}{d\varepsilon}} \tag{27}$$

Figures 14a and 14b shows the dimensionless (viscous scaled) turbulent viscosity in both inner and outer scaled wall-normal coordinates. When using outer layer scalings in Figure 14b, an approximately constant region of turbulent viscosity is obtained in DNS for  $y^+/Re_{\tau} > 0.4$ . This would correspond to the outer layer of the flow, and more precisely, to Clausius' precepts concerning an approximately constant turbulent viscosity in the outer layer [52]. In contrast with DNS, ODT model results only show a small region of approximately constant turbulent viscosity for  $y^+/Re_{\tau} > 0.8$  in turbulent channel flow. In ODT turbulent pipe flow, there is no apparent constancy of the turbulent viscosity. Once again, there are no meaningful differences between T-ODT and S-ODT results, with the exception of an apparent local maximum of the S-ODT pipe flow turbulent viscosity close to the pole (r = 0). Overall, the outer layer turbulent viscosity is not reproduced as well as other statistical quantities evaluated so far. As commented before, the shortcomings of the ODT model when predicting outer layer dynamics are not surprising. In principle, the outer layer would be best captured by traditional RANS turbulence models with constant coefficients, since the Boussinesq hypothesis would have full validity and applicability in such cases. In fact, the approximately constant region in Figure 14b would correspond to well-known values of constant coefficients in RANS turbulence models, e.g., the coefficient  $C_{\mu}$  in the RANS  $k - \varepsilon$  model. Despite the apparent shortcomings in ODT, we note that a good representation of the turbulent

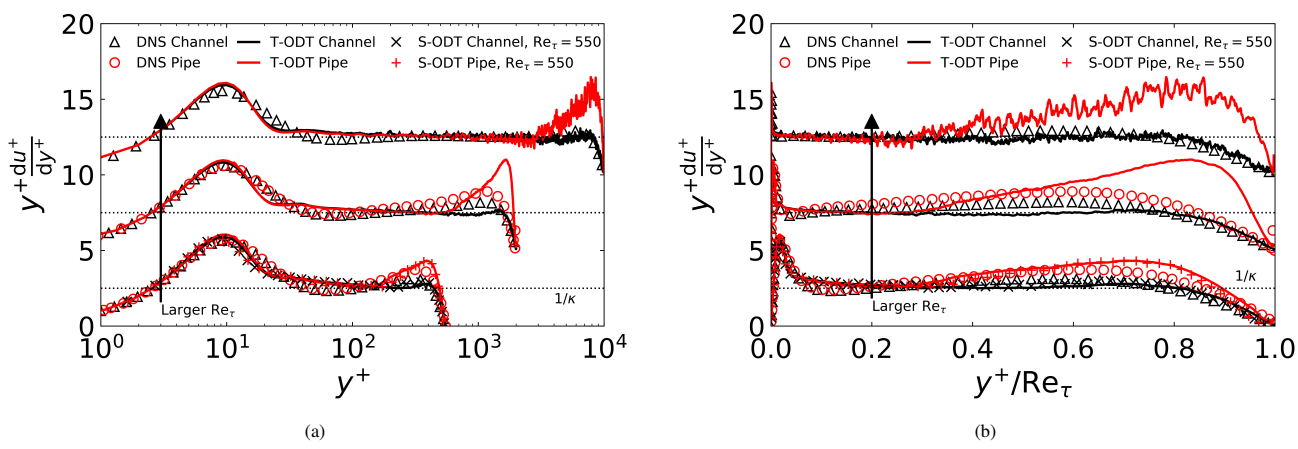


**FIGURE 13** Indicator function  $y^+(du^+/dy^+)$  for different Re $_{\tau}$  in turbulent pipe and channel flows (Cases 550CT, 550PT, 550CS, 550PS, 2000CT, 2000PT, 10000CT, 10000PT). Larger Reynolds numbers are shifted upward 5 viscous units for better visualization. DNS turbulent channel flow data from [5, 7], as well as DNS turbulent pipe flow data from [46, 6] are shown for reference. Note that there is no DNS reference data for turbulent pipe flow at Re $_{\tau}$  = 10000. (a) Inner layer scaling in  $y^+$  coordinates. (b) Outer layer scaling in  $y^+/Re_{\tau} = (\delta - |\xi|)/\delta$  coordinates.

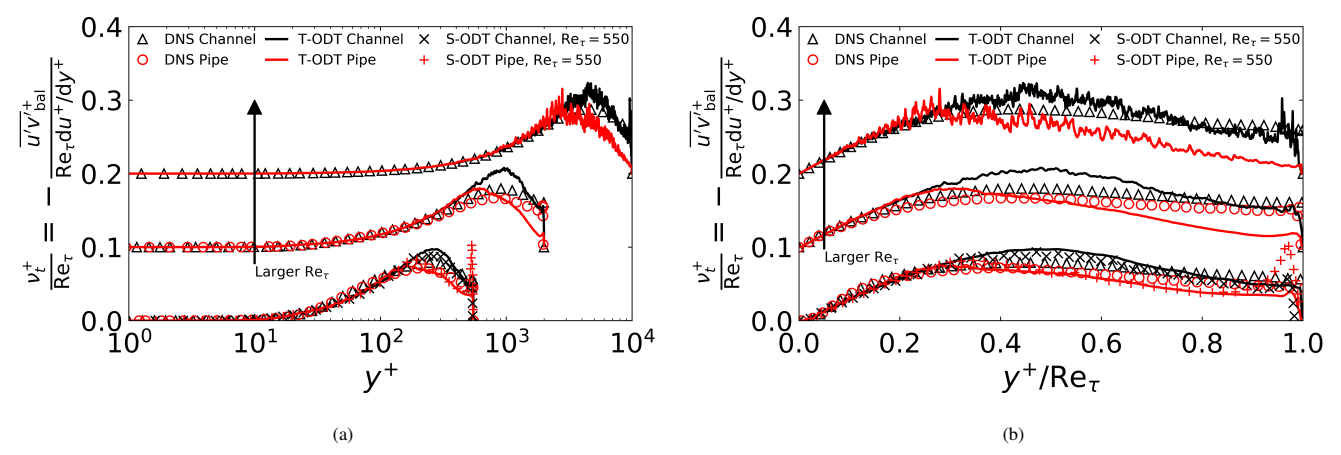


**FIGURE 14** Scaled turbulent viscosity for different  $Re_{\tau}$  in turbulent pipe and channel flows (Cases 550CT, 550PT, 550CS, 550PS, 2000CT, 2000PT, 10000CT, 10000PT). Larger Reynolds numbers are shifted upward by 0.1 units for better visualization. DNS turbulent channel flow data from [5, 7], as well as DNS turbulent pipe flow data from [46, 6] are shown for reference. Note that there is no DNS reference data for turbulent pipe flow at  $Re_{\tau} = 10000$ . (a) Inner layer scaling in  $y^+$  coordinates. (b) Outer layer scaling in  $y^+/Re_{\tau} = (\delta - |\xi|)/\delta$  coordinates.

viscosity is anyway obtained for a range of  $y^+$  values close to the wall (and said range increases with Re $_{\tau}$ ). This is seen in Figure 14a, and confirms that ODT can be used as a near-wall turbulence model. One could think about potential applications in which ODT is used as a near-wall model in constant coefficient RANS turbulence models (or in LES models), since the latter excel in performance away from the wall. One example is the ODT subgrid closure used in [35].

#### 5.2 Second-order statistics (TKE-related statistics)

We now discuss model results concerning TKE-related statistics. First, we discuss model results for root-mean-square (RMS) velocity profiles. To that extent, Figure 15a shows T-ODT and S-ODT model results for  $u_{RMS}^+$ ,  $v_{RMS}^+$  and  $w_{RMS}^+$  profiles in the

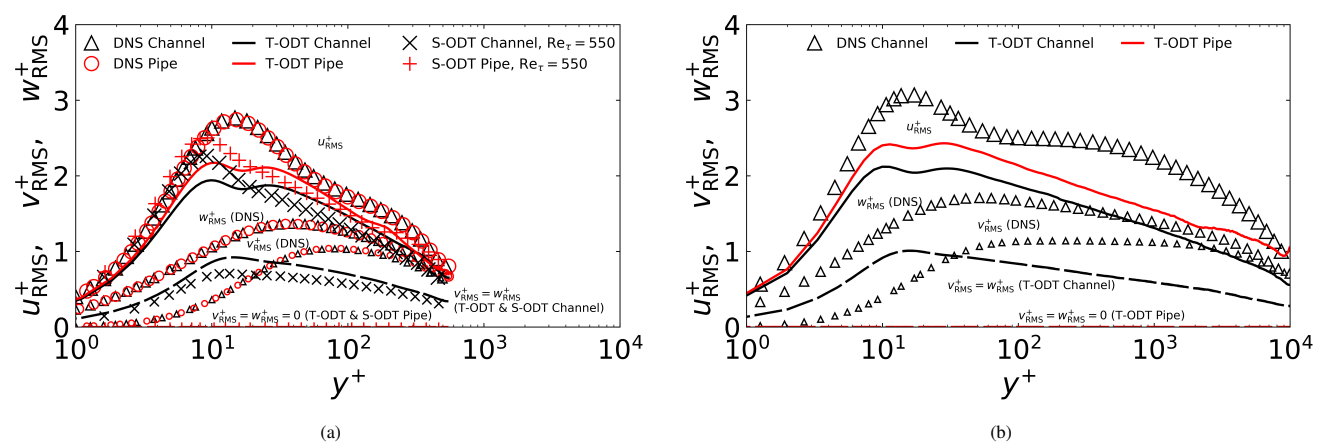


**FIGURE 15** (a) RMS velocity profiles in turbulent pipe and channel flows at  $Re_{\tau} = 550$  (Cases 550CT, 550PT, 550CS, 550PS) showing  $u_{RMS}^+$  (——, large symbols),  $v_{RMS}^+$  (- - - -, mid-sized and small symbols) and  $w_{RMS}^+$  (- - - -, mid-sized and small symbols). DNS turbulent channel flow data from [5], as well as DNS turbulent pipe flow data from [46] are shown for reference. (b) RMS velocity profiles in turbulent pipe and channel flows at  $Re_{\tau} = 10000$  (Cases 10000CT, 10000PT) showing  $u_{RMS}^+$  (——, large symbols),  $v_{RMS}^+$  (- - - -, small symbols) and  $w_{RMS}^+$  (- - - -, mid-sized symbols). DNS turbulent channel flow data from [7] is shown for reference.

turbulent channel and pipe flow at Re<sub> $\tau$ </sub> = 550. The RMS velocity profiles are calculated by the corresponding Reynolds average identity, e.g.,  $u_{\rm RMS} = \sqrt{\overline{u^2} - \overline{u}^2}$ , and are subsequently scaled by  $u_{\tau}$ . ODT turbulent pipe flow results only allow the evaluation of streamwise velocity profiles since  $\alpha = 0$  for cylindrical coordinates. Conversely, ODT turbulent channel flow simulations allow the evaluation of all RMS velocity profiles since  $\alpha = 2/3$ , noting that, however, both  $v_{\rm RMS}$  and  $w_{\rm RMS}$  exhibit the same statistics. This is seen in Figure 15a.

We note a shortcoming of the ODT model. Namely, regardless of the choice of  $\alpha$ , the model is not able to properly represent the anisotropy of the flow, or the different TKE contributions from the normal Reynolds stress components  $u_{RMS}^2 = \overline{u'u'}$ ,  $v_{RMS}^2 = \overline{v'v'}$ , and  $w_{RMS}^2 = \overline{w'w'}$ . The obtained profile  $v_{RMS}$  will always be equal to  $w_{RMS}$ . It is interesting to note though, that the normal Reynolds stress components are not considered for the modeling of the turbulent viscosity in the framework of the classical Boussinesq hypothesis for turbulent flows. From this point of view, the representation of the mean velocity profile is not affected by the deficient representation of the RMS velocity profiles, as we can evidence in all previously obtained results. Further inspection of Figure 15a shows that T-ODT model results for turbulent channel and pipe flows deliver a double peak in the streamwise  $u_{RMS}^2$  profile, with a local minimum in-between peaks which has a coincident position with that of the DNS  $u_{RMS}^2$  profile maximum. The double-peak issue has been observed several times in previous ODT publications, see [22, 26]. In contrast with T-ODT results, S-ODT results exhibit only a single peak in the  $u_{RMS}^2$  profile at low  $u_{RMS}^2 = u_{RMS}^2 = u_{RMS}^$ 

ODT pipe flow  $u_{\rm RMS}^+$  profiles lie above the corresponding ODT channel flow profiles. This may just be the effect of the ODT model parameter  $\alpha$ , which is different between channel and pipe flow simulations. Since  $\alpha=0$  in ODT pipe flows, all of the kinetic energy remains in the u velocity profile, and therefore, it is expected that said  $u_{\rm RMS}^+$  profile exceeds that in which TKE is redistributed among other normal Reynolds stress components, i.e., the case  $\alpha=2/3$  for channel flows. Figure 15b shows the same RMS velocity profiles, but at the largest Reynolds number  ${\rm Re}_{\tau}=10000$ . There are no meaningful differences regarding our previous observations at the lower  ${\rm Re}_{\tau}$ . There is a slight artificial increase in the  $u_{\rm RMS}^+$  ODT pipe flow profiles near the pole (r=0). This effect is exaggerated and more noticeable when using larger values of the factor  $A_{\rm tf}$  which yield smaller numerical diffusion effects due to mesh adaption, see Appendix B.1.

In addition to the TKE contributions due to the normal Reynolds stress components, we also evaluate the performance of the ODT model with respect to the different transport terms in the TKE equation (TKE budgets). This transport equation is relevant

for the formulation of well-known RANS models such as the  $k - \varepsilon$  or  $k - \omega$  models. In the following, all transport terms are calculated as indicated in Appendix A.5.

Figure 16a shows, for the turbulent channel flow at  $Re_{\tau} = 550$ , the ODT representation of the normalized transport terms, or TKE budgets, for both T-ODT and S-ODT models. In general, there is a reasonable representation of the transport terms in both T-ODT and S-ODT, when comparing with reference DNS data. The so-called advective transport contribution  $\mathcal{T}_A^+$  for comparison with ODT is calculated as the sum of the DNS turbulent velocity related diffusion and pressure-related diffusion TKE budgets. The peak of TKE production  $\hat{P}^+$  is slightly overestimated in the S-ODT model in comparison to the T-ODT model. However, the representation of the near-wall advective transport  $\mathcal{T}_A^+$ , and of the viscous transport of TKE,  $\mathcal{T}_V^+$ , is better in S-ODT. Additionally, the near-wall TKE dissipation term  $\varepsilon^+$  is also better represented in S-ODT. This confirms the leverage of the S-ODT formulation when evaluating near-wall gradients. Note that we also calculate the TKE dissipation by the balance of the TKE transport equation, noted as  $\varepsilon_{\text{bal}}$ . For T-ODT and S-ODT channel flows, the dissipation resulting from the balance of the TKE transport equation,  $\varepsilon_{\text{bal}}^+$ , coincides approximately with the dissipation term calculated from the definition in Appendix A.5, although the deviation is slightly larger in the (planar) S-ODT formulation. This proves that there is a negligible effect due to numerical dissipation in T-ODT and S-ODT channel flows.

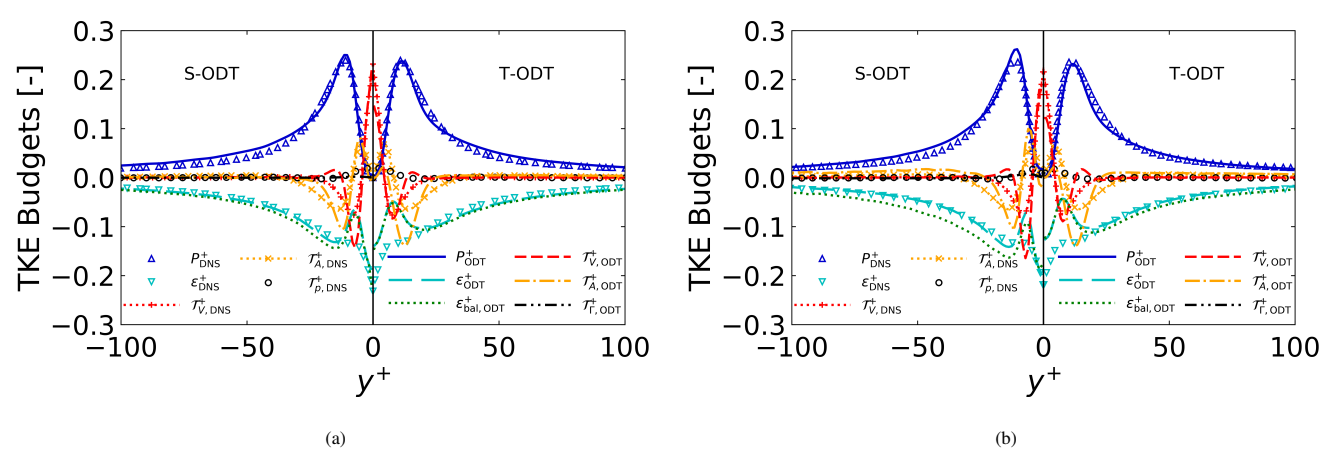
An important feature of S-ODT is that it allows the calculation of an equivalent pressure-diffusion transport term  $\mathcal{T}_{\Gamma}^+$ , comparable to the pressure-related transport in the DNS  $\mathcal{T}_p^+$ . This is not available in T-ODT. Said transport term in S-ODT results from the implementation of the FCE step, see also Appendix A.5. The results in Figure 16a show that  $\mathcal{T}_{\Gamma}^+$  is almost negligible; it is much smaller than the DNS reference data for  $\mathcal{T}_p^+$ . However, we recall that  $\mathcal{T}_p^+$  is in general negligible for low Mach number constant property flows.

Figure 16b shows the same results as in Figure 16a, but now for turbulent pipe flow at the equivalent  $Re_{\tau} = 550$ . There is a meaningful difference in the S-ODT pipe flow results between the dissipation term  $\varepsilon^+$  calculated by its definition in Appendix A.5, and the dissipation term which results from the balance of the TKE transport equation  $\varepsilon_{bal}^+$ . Said deviation is attributed to the chosen values of  $A_{tf}$  as discussed in Section 4.5, which results in non-negligible numerical diffusion due to mesh adaption. The imbalance in TKE transport due to numerical diffusion is also responsible for significant (nonphysical) nonzero values of  $\mathcal{T}_A^+$  away from the wall in the S-ODT cylindrical formulations. We did not find evidence of this issue in any other formulation, neither the T-ODT planar or cylindrical formulation, nor the S-ODT planar formulation. This is remediated by choosing a sufficiently large value of  $A_{tf}$ , as previously discussed in Section 4.5. For comparison, we show in Figures 17a and 17b, the equivalent results for the TKE budgets in S-ODT pipe flows using values  $A_{tf} = 4$  and  $A_{tf} = 100$ . There are additional issues related to numerical artifacts around the pole  $\hat{r} = 0$  in the ODT cylindrical formulation. Appendices A.3 and A.5 discuss some of these issues, which may affect the contributions to momentum and to the TKE. One issue of relevance relates to the appearance of an artificial homogeneous Neumann boundary condition around the pole discussed when performing the deterministic ODT advancement process, see Appendix A.3. Another issue is related to the calculation of the Reynolds stress  $\overline{u'v'}$  and of the turbulent (advective) TKE flux when using the flux accounting method discussed in Appendix A.5.

Finally, we show in Figure 18 the behavior of the turbulence frequency  $\omega^+ = \varepsilon^+/k^+$ , utilizing the TKE dissipation  $\varepsilon$  calculated as in Appendix A.5. This quantity is a measure of the turbulence time scale imposed by the flow, and it is relevant for some RANS turbulence models, namely, the well-known  $k-\omega$  model. Figure 18 shows that all ODT formulations are able to properly capture an apparent viscous sublayer power law for  $\omega$ . Additionally, all ODT formulations are also able to correctly predict the exponent of a power law for  $\omega$  in the logarithmic layer, evidenced by the apparent parallelism of the lines in the double logarithmic plot for  $y^+ > 30$ . Having said that, the prediction of the proportionality coefficient for said power law is incorrect, evidenced by the offset of the parallel lines with respect to DNS in the logarithmic layer. Also, unlike DNS, all ODT model results exhibit a non-monotonic behavior for  $\omega^+$  in the buffer layer, i.e., a local minimum can be seen at  $y^+ \approx 8$ . The ODT results for the turbulence frequency may signalize that, despite the fact that ODT is not able to properly represent contributions to the TKE (normal Reynolds stress components), scalings for the ratio of TKE to dissipation, i.e., scalings for the turbulence time-scale, may be reasonably reproduced in ODT. Thus, ODT could also supply valuable information for  $k-\omega$ -like (or  $k-\varepsilon$ -like) turbulence models.

#### 6 SUMMARY AND CONCLUSIONS

We have revisited the ODT formulation and its application for statistically steady, low Mach number turbulent channel and pipe flows with constant fluid properties. For the T-ODT model formulation, we have performed an extensive study in order to determine optimal model parameter values to use in a wide range of Reynolds numbers. To that extent, we found that the optimal value of the *Z* model parameter, for small viscous suppression of eddies in T-ODT, is related to the position of the peak of TKE



**FIGURE 16** Contributions (Budget terms) to the TKE transport equation, in turbulent channel and pipe flows at  $Re_{\tau} = 550$ . DNS turbulent channel flow data from [5], as well as DNS turbulent pipe flow data from [46], are shown for reference. (a) Turbulent channel flow (Cases 550CT, 550CS). (b) Turbulent pipe flow (Cases 550PT, 550PS).

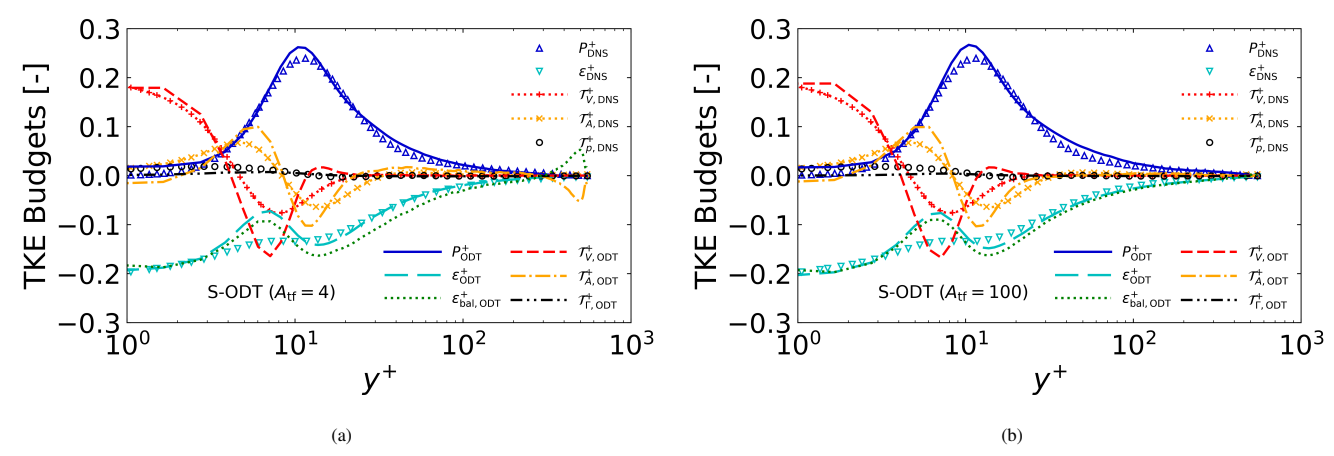


**FIGURE 17** Contributions (Budget terms) to the TKE transport equation, in turbulent S-ODT pipe flows at Re<sub> $\tau$ </sub> = 550 using different values of  $A_{tf}$ . DNS turbulent pipe flow data from [46] is shown for reference. (a)  $A_{tf}$  = 4 is used as in the (calibrated) T-ODT formulation. (b)  $A_{tf}$  = 100. Note that numerical imbalances lead to nonzero dissipation and advective transport around the pole  $\hat{r}$  = 0, see text.

production, or alternatively, to the position of intersection of the viscous and turbulent stress. We deem Z to be a Reynolds number independent parameter. Conversely, the optimal value of the C model parameter, related to the ODT eddy rate, can be determined by calibration with respect to the bulk skin friction coefficient of the flow. C is a model constant at large  $Re_{\tau}$ .

We have discussed several issues related to T-ODT model results concerning first order and second-order flow statistics. In general, we find a very reasonable representation of the mean flow and of the Reynolds shear stress profiles, as well as intrinsic evidence related to the existence of a logarithmic layer in the ODT flow. The model is in general not well-suited to represent the outer layer of the flow, although its performance improves at larger Reynolds numbers, e.g., in the prediction of the indicator function or of the turbulent viscosity. Second-order flow statistics (TKE-related statistics) such as the RMS velocity profiles, are not well represented in ODT. However, contributions to the TKE transport equation seem to be in reasonable agreement with reference DNS data, as well as apparent scalings related to the turbulence time-scale or the turbulence frequency  $\omega$ , at least in the viscous sublayer and the logarithmic layer. Overall, we find very similar results when comparing the dynamics of turbulent pipe and channel flows with ODT, as it is expected from boundary layer theory and from reference DNS data.

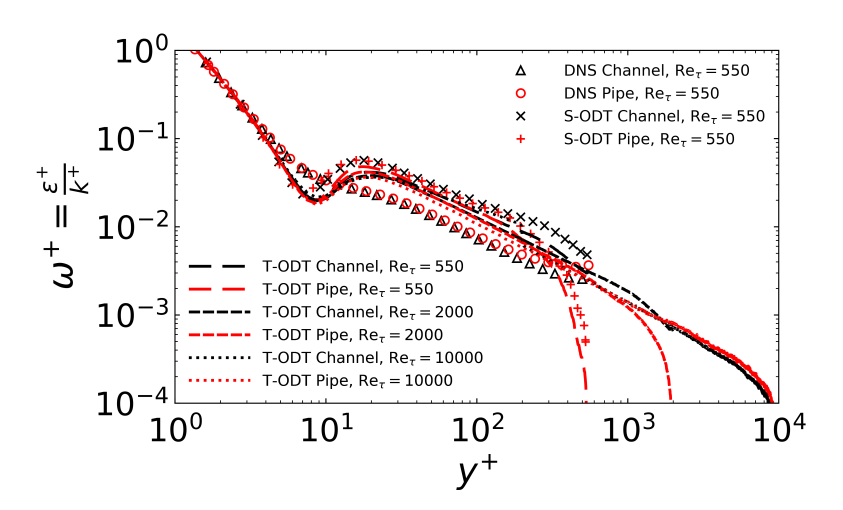


**FIGURE 18** Turbulence frequency  $\omega^+ = \varepsilon^+/k^+$  at different Re $_{\tau}$  (Cases 550CT, 550CS, 550PT, 550PS, 2000CT, 2000PT, 10000CT, 10000PT). DNS turbulent channel flow data from [5], as well as DNS turbulent pipe flow data from [46] are shown for reference. No DNS reference data for turbulent channel flow at Re $_{\tau} = 10000$  or for turbulent pipe flow at Re $_{\tau} = 2000$  or 10000 is presented.

In addition to the extensive evaluation performed with the T-ODT formulation, we have also introduced a novel modification to the existing S-ODT formulation. The modification is aimed at addressing confined flows, i.e., the turbulent channel and pipe flows, with a fully conservative FVM. The modified confined-flow treatment also led to the understanding of some effects related to adaptive grid formulations, which are usually not discussed, i.e., the role of the grid adaption parameter  $A_{tf}$ . This parameter and the dynamic grid adaptivity may be responsible for numerical diffusion. The largest effect due to numerical diffusion by grid adaption was evidenced in the context of the cylindrical formulation, most critically in the S-ODT cylindrical formulation.

S-ODT obeys a CFR-like forcing scheme of the flow, which contrasts with the FPG-like forcing used in constant properties T-ODT flows. The latter is typically used for statistically steady and streamwise homogeneous DNS of turbulent pipe and channel flows. In this context, the results obtained here for the statistically steady and streamwise-homogeneous S-ODT pipe and channel flows are merely illustrative, and serve only as a demonstrative way to prove the consistency between T-ODT and S-ODT. The numerical results showed that both model formulations were able to reasonably reproduce part of the reference DNS data, such as the mean flow related statistics. When evaluating TKE-related statistics with comparison to DNS reference data, the S-ODT formulation seems to deliver overall better results. Specifically, advective and viscous TKE transport budgets near the wall are better represented in S-ODT, as well as the near-wall TKE dissipation rate, in comparison to T-ODT.

Although it was not the main motivation of this work to prove the computational efficiency of the ODT model, we comment on some quantitative indicators. All of the ODT simulations carried out used, independently, one core of an AMD workstation EPYC 7452 (with 32 available cores). These cores share a CPU frequency of 2.35 GHz. The total available working memory in the workstation was 252 GB RAM. As an example for the sake of comparison, we note that an ODT pipe flow simulation at  $Re_{\tau} = 1000$  observes a dynamically adaptive grid with an initial number of 2000 cells. The nek5000 DNS pipe flow code used by Khoury et al. [46] required  $2.1842 \times 10^9$  grid points and employed an available infrastructure of 65536 cores for simulations at  $Re_{\tau} = 1000$ . Having said that, it is important to stress that the computational cost of ODT is not fundamentally related to the spatial discretization, since it is a 1-D model. Rather, it is more related to the number of ensemble members required for the calculation of converged statistics. Larger Reynolds number flows require larger averaging times (more ensemble members) for converged statistics. For the case 5200CT, T-ODT simulations required  $\approx 900$  CPU-h in order to achieve converged statistics. This is significantly cheaper than the equivalent DNS study from [5], which required a total of  $260 \times 10^6$  CPU-h in a supercomputer cluster [53]. The computational cost may also be affected by the complexity of the implemented numerical method. As a further cost example, the pipe flow case 550PT, a T-ODT simulation, required  $\approx 175$  CPU-h in order to achieve the converged statistics reported in this work. This measure is representative of both the simulation time, and of the simultaneous or concurrent online time-averaging required for statistical convergence. In S-ODT, due to the added complexity of the numerical

method and the degree of detail required when gathering converged statistics, the equivalent S-ODT case 550PS (Re $_{\tau}$  = 550) necessitated  $\approx 1225$  CPU-h. S-ODT simulations are, therefore, unequivocally more expensive than their T-ODT counterparts.

Naturally, it is not ideal to carry out S-ODT simulations in cases where T-ODT model formulations suffice. T-ODT is a robust model for statistically steady and streamwise homogeneous flows, but also for system dynamics; it can simulate unsteady, wall-normal inhomogeneous flow as a response of sudden application of uniform pressure gradients. To that extent, control of turbulent flow systems which can be idealized as streamwise homogeneous, as in very long fluid transport systems, or homogeneous chemical reactors or heat exchangers, is a relevant application case for T-ODT. Other engineering flows of relevance in which flow development is important, as in finite length annular pipe flows idealizing coaxial heat exchangers, are more relevant application cases for the newly proposed confined flow S-ODT formulation. In the aforementioned flows, radial mean flow asymmetry renders surrogate FPG-forcing models inconvenient. Further engineering cases of relevance could also be envisioned for S-ODT, such as variable cross-sectional area flow devices like compressors or diffusers. For academic research purposes, the novel confined flow S-ODT formulation presents new ways to potentially improve previous results, e.g., passive scalar transport results from [26], or previous developing heated pipe flow results from [27]. In any case, the modified S-ODT confined flow FVM formulation needs to be subject to more detailed studies in the future, with emphasis on the cylindrical formulation. In general, S-ODT could prove to be a way to effectively approximate confined elliptic flows as parabolic flows. In fact, the FCE step and related considerations presented in this work need not be particularly restricted to its application with ODT. It could also be applied in the future to confined laminar flows exhibiting some degree of ellipticity, e.g., as in the case of most slow moving flows in structured catalytic reactors.

Overall, turbulent spatially developing confined flows may exhibit challenging and technologically important multi-scale or multi-physics flow phenomena. Some of these could now be addressed in the future with the novel S-ODT confined flow framework.

#### **AUTHOR CONTRIBUTIONS**

**J. A. Medina Méndez:** Writing - original manuscript draft, visualization, validation, investigation, formal analysis, data curation, data management. **H. Schmidt:** Supervision, review, conceptualization. **D. O. Lignell:** Review and editing, methodology, supervision, conceptualization. **A. R. Kerstein:** Review and editing, methodology, supervision, conceptualization.

#### ACKNOWLEDGMENTS

We acknowledge the valuable insights and discussions provided by M. Klein during the entire time it took to develop this manuscript. We also acknowledge contributions of different kind made by several students, among others, by Beatriz Extremo and Pei-Yun Tsai.

#### FINANCIAL DISCLOSURE

Financial support provided by the European Regional Development Fund (EFRE-Brandenburg) is recognized and acknowledged in the framework of the former project 'Einsatz elektrohydrodynamisch getriebener Strömungen zur erweiterten Nutzung von Elektroabscheidern', grant number StaF 23035000. Support of the BTU Graduate Research School in the form of Conference Travel Grants is also greatly appreciated and acknowledged, as well as support from the German Academic Exchange Service (DAAD) in the form of research stays abroad. Heiko Schmidt also acknowledges the support by the German Federal Government, the Federal Ministry of Research, Technology and Space, and the State of Brandenburg, within the framework of the joint project EIZ: Energy Innovation Center (project numbers 85056897 and 03SF0693A) with funds from the Structural Development Act (Strukturstärkungsgesetz) for coal-mining regions.

#### CONFLICT OF INTEREST

The authors declare no potential conflict of interests.

#### REFERENCES

- 1. I. Marusic, B. J. McKeon, P. A. Monkewitz, H. M. Nagib, A. J. Smits, K. R. Sreenivasan, Phys. Fluids 22(6), 065103 (2010).
- 2. I. Marusic, J. P. Monty, M. Hultmark, A. J. Smits, J. Fluid Mech. **716**, R3 (2013).
- 3. X. Wu, P. Moin, J. Fluid Mech. 608, 81 (2008).
- 4. C. Chin, J.P. Monty, A. Ooi, Int. J. Heat Fluid Flow 45, 33 (2014).
- 5. M. Lee, R. Moser, J. Fluid Mech. 774, 395 (2015).
- 6. S. Pirozzoli, J. Romero, M. Fatica, R. Verzicco, P. Orlandi, J. Fluid Mech. 926, A28 (2021).
- 7. M. Oberlack, S. Hoyas, S. V. Kraheberger, F. Alcántara-Ávila, J. Laux, Phys. Rev. Lett. 128, 024502 (2022).
- 8. R. B. Dean, J. Fluids Eng. 100(2), 215 (1978).
- 9. M. P. Schultz, K. A. Flack, Phys. Fluids 25(025104) (2013).

- 10. M. Hultmark, M. Vallikivi, S. C. C. Bailey, A. J. Smits, Phys. Rev. Lett. 108(9), 094501 (2012).
- 11. E.-S. Zanoun, C. Egbers, D. Schanz, A. Schröder, E. Öngüner, M. Dittmar, Eur. J. Mech. B/Fluids 102, 103 (2023).
- 12. S. Pope, Turbulent Flows 11th ed. (Cambridge University Press, Cambridge, UK, 2011).
- 13. H. Schlichting, K. Gersten, Boundary-Layer Theory 9th ed. (Springer Nature, Berlin, Germany, 2017).
- 14. M. Ma, J. Lu, G. Tryggvason, Phys. Fluids 27(9), 092101 (2015).
- 15. M. Ma, J. Lu, G. Tryggvason, International Journal of Multiphase Flow 85, 336 (2016).
- 16. J.-L. Wu, H. Xiao, E. Paterson, Phys. Rev. Fluids 3, 074602 (2018).
- 17. A. Leonard, J. Comput. Phys. 37(3), 289 (1980).
- 18. A. J. Chorin, Communications on Pure and Applied Mathematics 39(S1), S47 (1986).
- 19. R. T. Pierrehumbert, Chaos: An Interdisciplinary Journal of Nonlinear Science 10(1), 61 (2000).
- 20. J. M. Ottino, S. C. Jana, V. S. Chakravarthy, Phys. Fluids 6(2), 685 (1994).
- 21. A. Kerstein, J. Fluid Mech. 392, 277 (1999).
- 22. D. Lignell, A. Kerstein, G. Sun, E. Monson, Theor. Comput. Fluid Dyn. 27(3-4), 273 (2013).
- 23. E. D. Gonzalez-Juez, A. R. Kerstein, D. Lignell, Geophys. Astrophys. Fluid Dyn. 107(5), 506 (2013).
- 24. Z. Jozefik, A. Kerstein, H. Schmidt, Combust. Flame 164, 53 (2016).
- 25. J. A. Medina Méndez, C. Bacher, U. Riebel, H. Schmidt, Eur. J. Mech. B/Fluids 95, 240 (2022).
- 26. M. Klein, H. Schmidt, D. O. Lignell, Int. J. Heat Fluid Flow 93, 108889 (2022).
- 27. J. A. Medina Méndez, M. Klein, H. Schmidt, Int. J. Heat Fluid Flow 80(108481) (2019).
- 28. A Kerstein, Combustion Science and Technology 60(4-6), 391 (1988).
- D. O. Lignell, V. B. Lansinger, J. Medina Méndez, M. Klein, A. R. Kerstein, H. Schmidt, M. Fistler, M. Oevermann, Theor. Comput. Fluid Dyn. 32(4), 495 (2018).
- 30. K. Mohseni, T. Colonius, J. Comput. Phys. 157(2), 787 (2000).
- 31. G.S. Constantinescu, S.K. Lele, J. Comput. Phys. 183(1), 165 (2002).
- 32. A. Kerstein, W. Ashurst, S. Wunsch, V. Nilsen, J. Fluid Mech. 447, 85 (2001).
- 33. R McDermott, Ph.D. thesis, University of Utah, (2005).
- 34. W. T. Ashurst, A. R. Kerstein, Phys. Fluids 17(2), 025107 (2005).
- 35. R. C. Schmidt, A. Kerstein, S. Wunsch, V. Nilsen, J. Comput. Phys. 186, 317 (2003).
- 36. B. Müller, J. Eng. Math. 34(1), 97 (1998).
- 37. J. G. M. Eggels, F. Unger, M. H. Weiss, J. Westerweel, R. J. Adrian, R. Friedrich, F. T. M. Nieuwstadt, J. Fluid Mech. 268, 175-210 (1994).
- 38. M. Quadrio, P. Ricco, J. Fluid Mech. 667, 135-157 (2011).
- 39. B. Frohnapfel, Y. Hasegawa, M. Quadrio, J. Fluid Mech. 700, 406–418 (2012).
- 40. M. Klein, C. Zenker, H. Schmidt, Chem. Eng. Sci. 204, 186 (2019).
- 41. N. Krishnamoorthy, Ph.D. thesis, University of Utah, (2008).
- 42. R. Moser, J. Kim, N. Mansour, Phys. Fluids 11(4), 943 (1999).
- 43. T. Tsukahara, Y. Seki, H. Kawamura, D. Tochio, in Fourth International Symposium on Turbulence and Shear Flow Phenomena.
- H. Kawamura, Direct Numerical Simulation Database for Turbulent Channel Flow with Heat Transfer (2025), Website accessed on 24.03.2025. https://www.rs.tus.ac.jp/t2lab/db/index.html.
- 45. E.-S. Zanoun, H. Nagib, F. Durst, Fluid Dynamics Research 41(2), 021405 (2009).
- 46. G. K. El Khoury, P. Schlatter, A. Noorani, P. F. Fischer, G. Brethouwer, A. V. Johansson, Flow, Turbul. Comb. 91(3), 475 (2013).
- 47. S. Hoyas, M. Oberlack, F. Alcántara-Ávila, S. V. Kraheberger, J. Laux, Phys. Rev. Fluids 7, 014602 (2022).
- 48. M. Klein, H. Schmidt, *Investigating thermal convection at low Prandtl numbers using one-dimensional turbulence*, Poster presented at TSFP11, see http://dx.doi.org/10.13140/RG.2.2.13144.24322 (2019).
- 49. F. Laadhari, Phys. Fluids **14**(10), L65 (2002).
- F. Meiselbach, Ph.D. thesis, Brandenburgische Technische Universität Cottbus-Senftenberg, (2015). https://opus4.kobv.de/opus4-btu/frontdoor/index/index/docId/3495.
- 51. G. I. Barenblatt, J. Fluid Mech. 248, 513-520 (1993).
- 52. F. H. Clauser, Adv. Appl. Mech. 4, 1 (1956).
- 53. M. Lee, N. Malaya, R. D. Moser, in *Proceedings of the International Conference on High Performance Computing, Networking, Storage and Analysis* (Association for Computing Machinery, New York, NY, USA, 2013).
- 54. T. Lackmann, A. Kerstein, M. Oevermann, Combust. Flame 193, 1 (2018).
- 55. A. Mignone, J. Comput. Phys. 270, 784 (2014).
- 56. A. Shiri, Ph.D. thesis, (2010). http://www.turbulence-online.com/Publications/Theses/Shiri10.pdf.

#### SUPPORTING INFORMATION

Additional supporting information may be found in the online version of the article at the publisher's website. A repository hosted at Zenodo, containing the simulation data, freely available for download and reference, will be linked here in the accepted version of the manuscript. A freely available version of ODT maintained by Prof. David Lignell, fully capable of simulating smooth wall turbulent pipe and channel flows with a T-ODT formulation can be accessed at https://github.com/BYUignite/ODT. The confined S-ODT formulation code is not included in said repository, but it can be provided upon request.

**How to cite this article:** Medina Méndez J.A., Schmidt H., Lignell D.O., and Kerstein A.R.. Revisiting the formulation and application of the One-Dimensional Turbulence model for pipe and channel flows. *Z. Angew. Math. Me.* 2025;00(00):1–18.

#### **APPENDIX**

#### A ODT FORMULATION

#### A.1 Triplet map formulation

We comment on the analytical form of the mapping  $f(\xi)$  (triplet map), which is used in ODT eddy events. First, for the sake of completion, we detail the relevant form of the mapping rule applicable in planar Cartesian coordinates. This is taken from [21, 32],

$$f(y) \equiv \begin{cases} 3y - 2y_0 & \text{if} \quad y_0 \le y \le y_0 + \frac{1}{3}l \\ 2l - 3y + 4y_0 & \text{if} \quad y_0 + \frac{1}{3}l \le y \le y_0 + \frac{2}{3}l \\ 3y - 2y_0 - 2l & \text{if} \quad y_0 + \frac{2}{3}l \le y \le y_0 + l \\ y & \text{otherwise} \end{cases}$$
(A1)

As specified in [32], this mapping rule is applicable for fluid at location f(y), which is moved to a location y as a consequence of the transformation.

Next, we provide a novel analytical formula for the rule f(r) applicable for triplet maps in cylindrical coordinates. There may be different types of mappings applicable in cylindrical coordinates. Lignell et al. [29] discuss some variants for the cylindrical triplet maps, from which we focus in the so-called Triplet Map A (TMA) formulation. The TMA formulation is derived next using an approach that is similar to the derivation of the spherical triplet map in [54]. First, assume positive  $r \ge 0$  coordinates. We can denote the volume of an ODT eddy event per unit streamwise length, and unit angular displacement  $\Omega_l/(\Delta z \Delta \theta)$ , as

$$\left. \frac{\Omega_l}{\Delta z \Delta \theta} \right|_{r \ge 0} = \int_{r_0}^{r_0 + l} r \mathrm{d}r = \frac{1}{2} \int_{r_0}^{r_0 + l} \mathrm{d}r^2 \tag{A2}$$

The identity is obtained by differentiation properties. The above expression can then be rewritten as

$$\left. \frac{\Omega_l}{\Delta z \Delta \theta} \right|_{r \ge 0} = \frac{1}{2} \left[ \int_0^{r_0 + l} dr^2 - \int_0^{r_0} dr^2 \right] \tag{A3}$$

This second identity is obtained by splitting integrals around the pole r = 0. Equation (A3) can be generalized for the coordinate  $\hat{r}$  using the signum operator sgn as

$$\frac{\Omega_l}{\Delta z \Delta \theta} = \frac{1}{2} \operatorname{sgn}(\hat{r}_0) \left[ \operatorname{sgn}(\hat{r}_0 + l) \operatorname{sgn}(\hat{r}_0) \int_0^{|\hat{r}_0 + l|} d\hat{r}^2 - \int_0^{|\hat{r}_0|} d\hat{r}^2 \right]$$
(A4)

We now use the identities outlined before to define the cylindrical triplet map. As in [54], we first find the internal boundaries  $\hat{r}_b$  for  $b \in \{0, 1, 2, 3\}$ , which limit the three segments of the triplet map. Note that for b = 0 we have the left edge of the eddy  $\hat{r}_0$ , while for b = 3 we have the right edge  $\hat{r}_3 = \hat{r}_0 + l$ . The boundaries  $\hat{r}_b$  are obtained following the consideration that the volume of each segment of the triplet map (TMA), is equivalent to one third of the overall eddy volume. To that extent, as an example, consider the boundary  $\hat{r}_1$ , which can be calculated by

$$\frac{1}{2} \int_0^{|\hat{r}_1|} d\hat{r}^2 = \operatorname{sgn}\left(\frac{1}{2} \int_0^{|\hat{r}_0|} d\hat{r}^2 + \operatorname{sgn}(\hat{r}_0) \frac{1}{3} \frac{\Omega_l}{\Delta z \Delta \theta}\right) \left[\frac{1}{2} \int_0^{|\hat{r}_0|} d\hat{r}^2 + \operatorname{sgn}(\hat{r}_0) \frac{1}{3} \frac{\Omega_l}{\Delta z \Delta \theta}\right] \tag{A5}$$

Substituting  $\Omega_l/(\Delta z \Delta \theta)$  from Eq. (A4), and solving for  $\hat{r}_1^2$ , we obtain,

$$\hat{r}_{1}^{2} = \operatorname{sgn}\left(\frac{1}{3}\operatorname{sgn}(\hat{r}_{0} + l)\operatorname{sgn}(\hat{r}_{0})\left(\hat{r}_{0} + l\right)^{2} + \frac{2}{3}\hat{r}_{0}^{2}\right)\left[\frac{1}{3}\operatorname{sgn}(\hat{r}_{0} + l)\operatorname{sgn}(\hat{r}_{0})\left(\hat{r}_{0} + l\right)^{2} + \frac{2}{3}\hat{r}_{0}^{2}\right]$$
(A6)

The boundary  $\hat{r}_2$ , or rather,  $\hat{r}_2^2$ , can be obtained in a very similar way,

$$\frac{1}{2} \int_0^{|\hat{r}_2|} d\hat{r}^2 = \operatorname{sgn}\left(\frac{1}{2} \int_0^{|\hat{r}_1|} d\hat{r}^2 + \operatorname{sgn}(\hat{r}_1) \frac{1}{3} \frac{\Omega_l}{\Delta z \Delta \theta}\right) \left[\frac{1}{2} \int_0^{|\hat{r}_1|} d\hat{r}^2 + \operatorname{sgn}(\hat{r}_1) \frac{1}{3} \frac{\Omega_l}{\Delta z \Delta \theta}\right] \tag{A7}$$

such that

$$\hat{r}_{2}^{2} = \operatorname{sgn}\left(\hat{r}_{1}^{2} + \frac{1}{3}\operatorname{sgn}(\hat{r}_{1})\operatorname{sgn}(\hat{r}_{0} + l)\left(\hat{r}_{0} + l\right)^{2} - \frac{1}{3}\operatorname{sgn}(\hat{r}_{1})\operatorname{sgn}(\hat{r}_{0})\hat{r}_{0}^{2}\right)$$

$$\left[\hat{r}_{1}^{2} + \frac{1}{3}\operatorname{sgn}(\hat{r}_{1})\operatorname{sgn}(\hat{r}_{0} + l)\left(\hat{r}_{0} + l\right)^{2} - \frac{1}{3}\operatorname{sgn}(\hat{r}_{1})\operatorname{sgn}(\hat{r}_{0})\hat{r}_{0}^{2}\right]$$
(A8)

The formula for all  $\hat{r}_b$  for  $b \in \{0, 1, 2, 3\}$  can then be written in a generalized form as

$$\hat{r}_{b}^{2} = \operatorname{sgn}\left(\hat{r}_{b-1}^{2} + \frac{1}{3}\operatorname{sgn}(\hat{r}_{b-1})\operatorname{sgn}(\hat{r}_{0} + l)(\hat{r}_{0} + l)^{2} - \frac{1}{3}\operatorname{sgn}(\hat{r}_{b-1})\operatorname{sgn}(\hat{r}_{0})\hat{r}_{0}^{2}\right)$$

$$\left[\hat{r}_{b-1}^{2} + \frac{1}{3}\operatorname{sgn}(\hat{r}_{b-1})\operatorname{sgn}(\hat{r}_{0} + l)(\hat{r}_{0} + l)^{2} - \frac{1}{3}\operatorname{sgn}(\hat{r}_{b-1})\operatorname{sgn}(\hat{r}_{0})\hat{r}_{0}^{2}\right]$$
(A9)

Note that the actual positions  $\hat{r}_b$  with their corresponding sign can be found by taking the square root of  $\hat{r}_b^2$ , and then multiplying the preceding RHS signum operator expression in Eq. (A9) by the sign of the boundary  $\hat{r}_{b-1}$ . Next, we find the mapping rule in the first segment of the triplet map (TMA). In said segment, the scalar profile from the range  $[\hat{r}_0, \hat{r}_0 + l]$  is compressed to fit the range  $[\hat{r}_0, \hat{r}_0 + l]$ . The equivalence between the fluid at location  $f(\hat{r})$  and the mapped location  $\hat{r}$  is given by a volumetric relation, which considers that the volume resulting from the fluid at location  $f(\hat{r})$  and the left edge of the eddy  $\hat{r}_0$ , is three times the volume of the corresponding mapped location  $\hat{r}$  in the first segment of the map. Therefore, similar to the procedure to find  $\hat{r}_b$ , we get

$$\frac{1}{2} \int_{0}^{|f(\hat{r})|} d\hat{r}^{2} = \operatorname{sgn}\left(\frac{1}{2} \int_{0}^{|\hat{r}_{0}|} d\hat{r}^{2} + 3\operatorname{sgn}(\hat{r}_{0}) \left[\frac{1}{2}\operatorname{sgn}(\hat{r}) \int_{0}^{|\hat{r}|} d\hat{r}^{2} - \frac{1}{2}\operatorname{sgn}(\hat{r}_{0}) \int_{0}^{|\hat{r}_{0}|} d\hat{r}^{2}\right]\right) \\
\left\{\frac{1}{2} \int_{0}^{|\hat{r}_{0}|} d\hat{r}^{2} + 3\operatorname{sgn}(\hat{r}_{0}) \left[\frac{1}{2}\operatorname{sgn}(\hat{r}) \int_{0}^{|\hat{r}|} d\hat{r}^{2} - \frac{1}{2}\operatorname{sgn}(\hat{r}_{0}) \int_{0}^{|\hat{r}_{0}|} d\hat{r}^{2}\right]\right\} \tag{A10}$$

After some rearrangement and solving for  $f^2(\hat{r})$ , we find

$$f^{2}(\hat{r}) \bigg|_{\text{1st segment}} = \text{sgn}\left(3\text{sgn}(\hat{r}_{0})\text{sgn}(\hat{r})\hat{r}^{2} - 2\hat{r}_{0}^{2}\right) \left[3\text{sgn}(\hat{r}_{0})\text{sgn}(\hat{r})\hat{r}^{2} - 2\hat{r}_{0}^{2}\right]$$
(A11)

In the second segment of the triplet map, the scalar profile from the range  $[\hat{r}_0, \hat{r}_0 + l]$  is compressed to fit the range  $[\hat{r}_0 + l/3, \hat{r}_0 + 2l/3]$ , and is subsequently reversed (inverted slope). In order to invert the profile, we state a volumetric relation between  $f(\hat{r})$  and the right edge of the eddy at  $\hat{r}_0 + l$ . The corresponding relation is

$$\frac{1}{2} \int_{0}^{|f(\hat{r})|} d\hat{r}^{2} = \operatorname{sgn}\left(\frac{1}{2} \int_{0}^{|\hat{r}_{0}+l|} d\hat{r}^{2} - 3\operatorname{sgn}(\hat{r}_{0}+l) \left[\frac{1}{2}\operatorname{sgn}(\hat{r}) \int_{0}^{|\hat{r}|} d\hat{r}^{2} - \frac{1}{2}\operatorname{sgn}(\hat{r}_{1}) \int_{0}^{|\hat{r}_{1}|} d\hat{r}^{2}\right]\right) \\
\left\{\frac{1}{2} \int_{0}^{|\hat{r}_{0}+l|} d\hat{r}^{2} - 3\operatorname{sgn}(\hat{r}_{0}+l) \left[\frac{1}{2}\operatorname{sgn}(\hat{r}) \int_{0}^{|\hat{r}|} d\hat{r}^{2} - \frac{1}{2}\operatorname{sgn}(\hat{r}_{1}) \int_{0}^{|\hat{r}_{1}|} d\hat{r}^{2}\right]\right\} \tag{A12}$$

From which, solving for  $f^2(\hat{r})$ , we find

$$f^{2}(\hat{r}) \bigg|_{\text{2nd segment}} = \operatorname{sgn}\left( (\hat{r}_{0} + l)^{2} - 3\operatorname{sgn}(\hat{r}_{0} + l)\operatorname{sgn}(\hat{r})\hat{r}^{2} + 3\operatorname{sgn}(\hat{r}_{0} + l)\operatorname{sgn}(\hat{r}_{1})\hat{r}_{1}^{2} \right)$$

$$\left[ (\hat{r}_{0} + l)^{2} - 3\operatorname{sgn}(\hat{r}_{0} + l)\operatorname{sgn}(\hat{r})\hat{r}^{2} + 3\operatorname{sgn}(\hat{r}_{0} + l)\operatorname{sgn}(\hat{r}_{1})\hat{r}_{1}^{2} \right]$$
(A13)

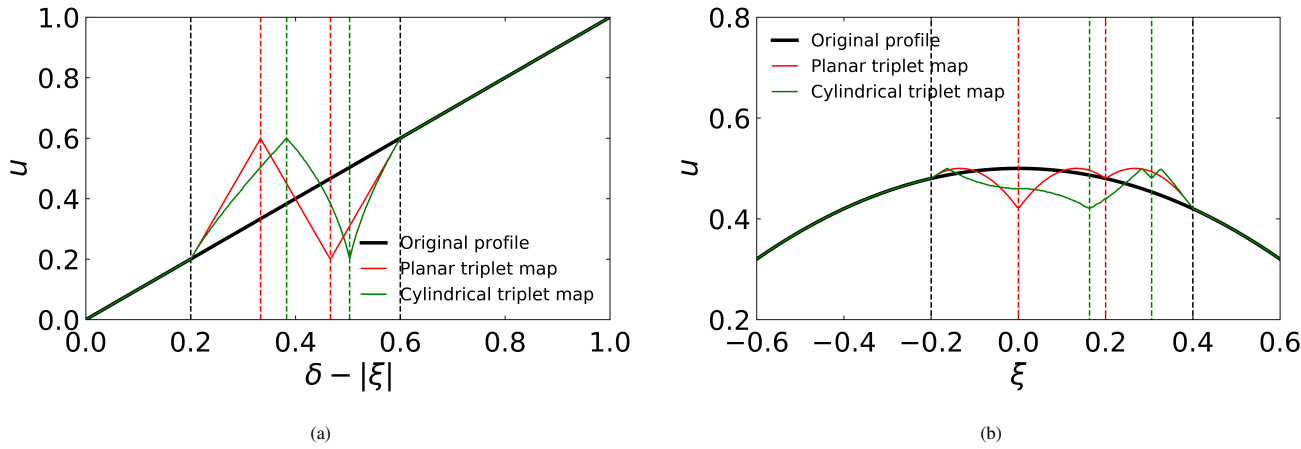


**FIGURE A1** Effect of planar and cylindrical triplet maps on a scalar velocity profile. The dashed vertical lines indicate the internal boundaries of the map (first, second and third segments). (a) Near-wall triplet map applied on a linear velocity profile using  $\delta = 1$ ,  $\xi_0 = -0.8$  and l = 0.4. (b) Centerline-asymmetric triplet map applied on a parabolic velocity profile using  $\delta = 1$ ,  $\xi_0 = -0.2$  and l = 0.6.

The third segment in the map is entirely similar to the first one. Similar reasoning leads then to

$$f^{2}(\hat{r})\bigg|_{\text{3rd segment}} = \operatorname{sgn}\left(\hat{r}_{0}^{2} + 3\operatorname{sgn}(\hat{r}_{0})\operatorname{sgn}(\hat{r})\hat{r}^{2} - 3\operatorname{sgn}(\hat{r}_{0})\operatorname{sgn}(\hat{r}_{2})\hat{r}_{2}^{2}\right)\left[\hat{r}_{0}^{2} + 3\operatorname{sgn}(\hat{r}_{0})\operatorname{sgn}(\hat{r})\hat{r}^{2} - 3\operatorname{sgn}(\hat{r}_{0})\operatorname{sgn}(\hat{r}_{2})\hat{r}_{2}^{2}\right]$$
(A14)

Similar to the determination of the positions  $\hat{r}_b$ , we can find the actual positions  $f(\hat{r})$  by taking the square root of  $f^2(\hat{r})$  and then multiplying the preceding signum operator expressions on the RHS of Eq. (A11), (A13) and (A14) by the sign of  $\hat{r}_0$ ,  $\hat{r}_0 + l$  and  $\hat{r}_0$ , in the first, second and third segments, respectively. To summarize, the generalized mapping rule in cylindrical coordinates, for a fluid at location  $f(\hat{r})$  and mapped location  $\hat{r}$ , takes the form

$$f(\hat{r}) \equiv \begin{cases} \operatorname{sgn}(F_1) \operatorname{sgn}(\hat{r}_0) \sqrt{\operatorname{sgn}(F_1)F_1}, & F_1 = 3\operatorname{sgn}(\hat{r}_0) \operatorname{sgn}(\hat{r}) \hat{r}^2 - 2\hat{r}_0^2 & \text{if} \quad \hat{r}_0 \leq \hat{r} \leq \hat{r}_1 \\ \operatorname{sgn}(F_2) \operatorname{sgn}(\hat{r}_0 + l) \sqrt{\operatorname{sgn}(F_2)F_2}, & F_2 = (\hat{r}_0 + l)^2 - 3\operatorname{sgn}(\hat{r}_0 + l)\operatorname{sgn}(\hat{r}) \hat{r}^2 + 3\operatorname{sgn}(\hat{r}_0 + l)\operatorname{sgn}(\hat{r}_1)\hat{r}_1^2 & \text{if} \quad \hat{r}_1 \leq \hat{r} \leq \hat{r}_2 \\ \operatorname{sgn}(F_3) \operatorname{sgn}(\hat{r}_0) \sqrt{\operatorname{sgn}(F_3)F_3}, & F_3 = \hat{r}_0^2 + 3\operatorname{sgn}(\hat{r}_0)\operatorname{sgn}(\hat{r}) \hat{r}^2 - 3\operatorname{sgn}(\hat{r}_0)\operatorname{sgn}(\hat{r}_2)\hat{r}_2^2 & \text{if} \quad \hat{r}_2 \leq \hat{r} \leq \hat{r}_0 + l \\ \hat{r} & \text{otherwise} \end{cases}$$

Figure A1a shows the effect of a planar and a cylindrical triplet map on a linear velocity profile, e.g., near the wall in a turbulent pipe or channel flow. For comparison, we also show in Figure A1b the effect of slightly asymmetric maps (asymmetric with respect to the centerline) on a parabolic velocity profile.

#### A.2 Kernel coefficients

Next, we explain the calculation of the kernel coefficients  $\underline{c} = [c_w, c_v, c_u]^T$  and  $\underline{b} = [b_w, b_v, b_u]^T$  in Equations (2) and (10). These coefficients modify the corresponding velocity components during eddy events, and are associated to the kinetic energy redistribution procedure detailed in Sections 2.1.1 and 2.2.1.

#### **A.2.1** T-ODT kernel coefficients

The procedure for calculation of the T-ODT kernel coefficients is explained in [22] and [29]. Here, we only summarize the most important issues. It is necessary to conserve momentum upon application of any triplet map and kernel procedure during eddy

events. As per Eq. (2), observing constant density, this implies

$$\int_{\xi_0}^{\xi_0+l} \underline{u}(\xi, t_e) \xi^m d\xi = \int_{\xi_0}^{\xi_0+l} \left[ \underline{u}(f(\xi), t_e) + \underline{c}K(\xi) \right] \xi^m d\xi$$
(A16)

For subsequent ease of notation and clarity, we note that it is possible to replace integrals of the form  $\int u^n(\xi)\xi^m d\xi$  by  $\int u^n(f(\xi))\xi^m d\xi$  due to the measure preserving properties of the triplet map. To that extent, momentum conservation can be rewritten as

$$\int_{\xi_0}^{\xi_0+l} \underline{u}(f(\xi), t_e) \xi^m d\xi = \int_{\xi_0}^{\xi_0+l} \left[ \underline{u}(f(\xi), t_e) + \underline{c}K(\xi) \right] \xi^m d\xi$$
(A17)

Since  $\underline{c}$  is uniform, and by definition  $\int_{\xi_0}^{\xi_0+l} K(\xi) \xi^m d\xi = 0$ , Eq. (A17) is trivially satisfied. For low Mach number isothermal constant density flows, the total energy may be evaluated by the kinetic energy of the flow. An eddy event causes the kinetic energy of all velocity components to change by a certain amount. Omitting functional dependencies other than those needed to indicate mapped quantities, said change  $\Delta \underline{E}$  per velocity component, which has units of energy per unit area in a planar formulation, and of energy per unit length and unit angular displacement in a cylindrical formulation, is given by

$$\Delta \underline{E} = \frac{1}{2} \rho \int_{\xi_0}^{\xi_0 + l} \left[ \underline{u}(f(\xi)) * \underline{u}(f(\xi)) * \underline{u}(f(\xi)) * \underline{c}K + K^2 \underline{c} * \underline{c} \right] \xi^m d\xi - \frac{1}{2} \rho \int_{\xi_0}^{\xi_0 + l} \underline{u}(f(\xi)) * \underline{u}(f(\xi)) \xi^m d\xi$$
(A18)

We have defined the operator \* in Eq. (A18) as an element-wise product operator, such that Eq. (A18) remains a vector equation. The sum of the changes in kinetic energy  $\Delta \underline{E}$  among all velocity components results in the conservation of total kinetic energy during eddy events, i.e.,

$$\Delta \underline{E} \cdot \underline{1} = 0 \tag{A19}$$

We have used  $\underline{1} = [1, 1, 1]^T$ . For the sake of a simplified notation, we introduce the following variable substitution,

$$\underline{u_K} \equiv \int_{\xi_0}^{\xi_0 + l} \underline{u}(f(\xi)) K \xi^m d\xi \tag{A20}$$

In order to determine c, we resort to Eq. (A18), which can then be rewritten using Eq. (A20) as

$$\left(\frac{1}{2} \int_{\xi_0}^{\xi_0 + l} K^2 \xi^m d\xi\right) \underline{c} * \underline{c} + \underline{u_K} * \underline{c} - \frac{\Delta \underline{E}}{\rho} = 0$$
(A21)

The quadratic solution for c is, following [22] and [29].

$$\underline{c} = \frac{-\underline{u_K} + \operatorname{sgn}\left(\underline{u_K}\right)\sqrt{\underline{u_K} * \underline{u_K} + 2\left(\int_{\xi_0}^{\xi_0 + l} K^2 \xi^m d\xi\right) \frac{\Delta \underline{E}}{\rho}}}{\left(\int_{\xi_0}^{\xi_0 + l} K^2 \xi^m d\xi\right)}$$
(A22)

The signum operator term  $\operatorname{sgn}(\underline{u_K})$  has been used to resolve the ambiguity of the sign of the corresponding root. Note that we can also find a global minimum for  $\Delta \underline{E}$  by differentiating Eq. (A21) with respect to  $\underline{c}$ , and setting the result equal to zero. Said procedure results in the value  $\underline{c}_{\text{crit}}$  yielding  $\Delta \underline{E}_{\text{min}}$ ,

$$\underline{c}_{\text{crit}} = -\frac{\underline{u}_K}{\int_{\xi_0}^{\xi_0 + l} K^2 \xi^m d\xi}$$
(A23)

The minimum kinetic energy change  $\Delta \underline{E}_{\min}$  is then, upon substitution of  $\underline{c}_{\text{crit}}$ ,

$$\Delta \underline{E}_{\min} = -\rho \frac{\underline{u}_K * \underline{u}_K}{2 \int_{\xi_0}^{\xi_0 + l} K^2 \xi^m d\xi}$$
(A24)

This leads to the definition of the available or extractable kinetic energy per velocity component Q,

$$\underline{Q} \equiv -\Delta \underline{E}_{\min} = \rho \frac{u_K * u_K}{2 \int_{\xi_0}^{\xi_0 + l} K^2 \xi^m d\xi}$$
(A25)

Due to total energy conservation, Eq. (A19), the kinetic energy change per velocity component  $\Delta \underline{E}$  is related to the available kinetic energy  $\underline{Q}$  in a phenomenological way. This introduces the ODT model parameter  $\alpha$  as a way to control the redistribution of kinetic energy among velocity components, see [32],

$$\Delta \underline{E} = \alpha \underline{T} Q \tag{A26}$$

The transfer matrix  $\underline{T}$  in Eq. (A26) is defined as in [32],

$$\underline{\underline{T}} = \frac{1}{2} \begin{bmatrix} -2 & 1 & 1 \\ 1 & -2 & 1 \\ 1 & 1 & -2 \end{bmatrix} \tag{A27}$$

Upon substitution of Eq. (A26) and (A25) in Eq. (A22), we find the formula for calculation of the kernel coefficient vector c,

$$\underline{c} = \frac{-\underline{u_K} + \operatorname{sgn}\left(\underline{u_K}\right)\sqrt{\underline{u_K} * \underline{u_K} + \alpha}\underline{\underline{T}}\underline{u_K} * \underline{u_K}}{\left(\int_{\xi_0}^{\xi_0 + l} K^2 \xi^m d\xi\right)}$$
(A28)

Note that use of  $\alpha = 0$  in Eq. (A28) leads to  $\underline{c} = \underline{0}$ , a vector with components equal to zero. This is the case of the cylindrical formulation used in this work.

#### A.2.2 S-ODT kernel coefficients

The procedure for calculation of the S-ODT kernel coefficients is, mostly, similar to that in T-ODT. We summarize here again only the most important issues from the discussion in [22] and [29]. Notably, instead of conservation laws for (specific) scalars, S-ODT eddy events observe balances of flux-related (specific) quantities due to streamwise velocity advection. We refer first to the balance of momentum flux (due to streamwise advection) upon application of a triplet map and ODT kernel functions as per Eq. (10), considering constant density,

$$\int_{\xi_0}^{\xi_0+l} u(f(\xi)) \underline{u}(f(\xi)) \xi^m d\xi = \int_{\xi_0}^{\xi_0+l} u(f(\xi)) \left[ \underline{u}(f(\xi)) + \underline{c}K(\xi) + \underline{b}J(\xi) \right] \xi^m d\xi$$
(A29)

Note the subtle notation difference between the vector  $\underline{u} = [v, w, u]^T$  and the streamwise velocity component u. The balance of kinetic energy flux per velocity component due to streamwise velocity advection is

$$\Delta \underline{E}_{\underline{u}} = \frac{1}{2} \rho \int_{\xi_{0}}^{\xi_{0}+l} u(f(\xi)) \left[ \underline{u}(f(\xi)) * \underline{u}(f(\xi)) + 2\underline{u}(f(\xi)) * (\underline{c}K + \underline{b}J) + K^{2}\underline{c} * \underline{c} + 2KJ\underline{c} * \underline{b} + J^{2}\underline{b} * \underline{b} \right] \xi^{m} d\xi$$

$$- \frac{1}{2} \rho \int_{\xi_{0}}^{\xi_{0}+l} u(f(\xi)) \left[ \underline{u}(f(\xi)) * \underline{u}(f(\xi)) \right] \xi^{m} d\xi$$
(A30)

Eq. (A29) and (A30) resemble the equations for steady state streamwise momentum and energy flux balances, respectively, upon application of the K and J kernels to the velocity profiles, and under assumption of mass conservation and uniform thermodynamic pressure. The only inconsistency is that the streamwise advecting velocity u on the post-mapped momentum and energy fluxes, see RHS of Eqs. (A29) and (A30), is modified by the triplet map, but not by the subsequent kernel application. This has been discussed in Section 2.2.2. It is not possible to simultaneously enforce constraints on the mass, momentum and energy in S-ODT, since doing so would require elliptic considerations on the pressure. This is the reason why the local constancy of the streamwise mass flux is enforced in a subsequent correction step, modifying the cross-section of the (semi-)Lagrangian S-ODT volume. Furthermore, the presence of walls requires the implementation of the additional FCE step in an entirely similar way to that discussed in Section 2.2.2 and 2.2.3. In addition to Eq. (A29) and (A30), an additional constraint related to the total streamwise kinetic energy flux is observed, similar to T-ODT,

$$\Delta E_u \cdot 1 = 0 \tag{A31}$$

We now introduce the following substitution of variables,

$$u_{Ju} \equiv \int_{\xi_{0}}^{\xi_{0}+l} u(f(\xi))J\xi^{m}d\xi$$

$$u_{Ku} \equiv \int_{\xi_{0}}^{\xi_{0}+l} u(f(\xi))K\xi^{m}d\xi$$

$$u_{KKu} \equiv \int_{\xi_{0}}^{\xi_{0}+l} u(f(\xi))J^{2}\xi^{m}d\xi$$

$$u_{JJu} \equiv \int_{\xi_{0}}^{\xi_{0}+l} u(f(\xi))J^{2}\xi^{m}d\xi = u_{KKu}, \quad \text{since} \quad J^{2} = |K|^{2} = K^{2}$$

$$u_{KJu} \equiv \int_{\xi_{0}}^{\xi_{0}+l} u(f(\xi))KJ\xi^{m}d\xi$$

$$\underline{u_{Juu}} \equiv \int_{\xi_{0}}^{\xi_{0}+l} u(f(\xi))\underline{u}(f(\xi))J\xi^{m}d\xi$$

$$\underline{u_{Kuu}} \equiv \int_{\xi_{0}}^{\xi_{0}+l} u(f(\xi))\underline{u}(f(\xi))K\xi^{m}d\xi$$

$$\underline{u_{Kuu}} \equiv \int_{\xi_{0}}^{\xi_{0}+l} u(f(\xi))\underline{u}(f(\xi))K\xi^{m}d\xi$$

Using Eq. (A32), Eq. (A29) is rewritten as

$$\underline{b}u_{Ju} = -\underline{c}u_{Ku} \tag{A33}$$

For further ease of notation, we also define

$$H_{u} \equiv \frac{u_{Ku}}{u_{Ju}}$$

$$\underline{P_{u}} \equiv \underline{u_{Kuu}} - H\underline{u_{Juu}}$$

$$S_{u} \equiv \frac{1}{2} \left(H_{u}^{2} + 1\right) u_{KKu} - H_{u}u_{KJu}$$
(A34)

In order to determine  $\underline{c}$ , we resort to Eq. (A30), which can then be rewritten using Eq. (A32) and (A34) as

$$S_{u}\underline{c} * \underline{c} + \underline{P_{u}} * \underline{c} - \frac{\Delta \underline{E_{u}}}{\rho} = 0 \tag{A35}$$

The solution for c is then, following [22] and [29],

$$\underline{c} = \frac{-\underline{P_u} + \operatorname{sgn}\left(\underline{P_u}\right)\sqrt{\underline{P_u} * \underline{P_u} + 4S_u \frac{\Delta E_u}{\rho}}}{2S_u} \tag{A36}$$

As in T-ODT, there is a critical coefficient  $\underline{c}_{crit}$  which yields a minimum kinetic energy flux change per velocity component,

$$\underline{c}_{\text{crit}} = -\frac{P_u}{2S_u} \tag{A37}$$

The minimum kinetic energy flux change defines then the available or extractable kinetic energy flux  $Q_u$ ,

$$\underline{Q_u} \equiv -\Delta \underline{E_u}_{\min} = \rho \frac{P_u * \underline{P_u}}{4S_u} \tag{A38}$$

As in T-ODT, due to the constraint given by Eq. (A31),  $\Delta \underline{E_u}$  is related to  $\underline{Q_u}$  by the ODT model parameter  $\alpha$  and the same transfer matrix  $\underline{T}$  from Eq. (A27),

$$\Delta E_u = \alpha \underline{T} \ Q_u \tag{A39}$$

Upon substitution of Eq. (A39) and (A38) in Eq. (A36), we find the formula for calculation of the kernel coefficient vector  $\underline{c}$  in the S-ODT formulation,

$$\underline{c} = \frac{-\underline{P_u} + \operatorname{sgn}\left(\underline{P_u}\right)\sqrt{\underline{P_u} * \underline{P_u} + \alpha \underline{\underline{T}} \underline{P_u} * \underline{P_u}}}{2S_u} \tag{A40}$$

By substitution of Eq. (A40) in Eq. (A33), we find the value of the coefficient vector  $\underline{b}$  in S-ODT,

$$\underline{b} = -H_u \left[ \frac{-\underline{P}_u + \operatorname{sgn}(\underline{P}_u) \sqrt{\underline{P}_u * \underline{P}_u + \alpha} \underline{\underline{T}} \underline{P}_u * \underline{P}_u}{2S_u} \right]$$
(A41)

As in T-ODT, use of  $\alpha = 0$  in Eq. (A40) and (A41) leads to  $\underline{c} = \underline{b} = \underline{0}$ . Note also that for S-ODT channel flows, with  $\alpha \neq 0$ , some eddy events may occasionally cause negative values u < 0 upon implementation of the kernel procedure. Said negative values violate parabolic flow assumptions in S-ODT, and as such, these candidate eddy events are discarded and not implemented (even if they succeed the acceptance probability test as explained in Section 2.2.1).

#### A.3 Numerical methods and discretization issues

The discretization and numerical advancement of the ODT governing equations for use in the deterministic advancement process is discussed next. We specialize the discussion and notation to the T-ODT and S-ODT cylindrical formulations.

# **A.3.1** T-ODT cylindrical formulation

The FVM for the integral T-ODT momentum pipe flow equation, Eq. (9), is obtained by discretization of the  $\hat{r}$  coordinate in a numerical domain  $[-\delta, \delta]$ , considering grid cells with midpoint-located cell centers identified with subindex i, and corresponding cell interfaces identified with subindices i + 1/2 and i - 1/2. The numerical grid is irregular, since an adaptive mesh is used, see [22]. Constant properties are assumed within cells and the density is constant. This results in the trivial enforcement of mass conservation, Eq. (8), which implies that there are no changes in the cell interfaces or cell sizes during numerical time integration. The T-ODT momentum pipe flow equation, Eq. (9), is then the only equation required for numerical advancement. Said equation is integrated numerically in time using an explicit Euler time-advancement scheme. The resulting numerical discretization is

$$\left(\frac{\underline{u_{i,n+1}} - \underline{u_{i,n}}}{\Delta t}\right) \frac{\left(\Delta \hat{r}_i^2\right)}{2} = -\frac{1}{\rho} \frac{\mathrm{d}\overline{p}}{\mathrm{d}z} \underbrace{e_z}{2} + \eta \left[ \left(\hat{r}_{i+1/2} \frac{\underline{u_{i+1,n}} - \underline{u_{i,n}}}{\hat{r}_{i+1} - \hat{r}_i}\right) - \left(\hat{r}_{i-1/2} \frac{\underline{u_{i,n}} - \underline{u_{i-1,n}}}{\hat{r}_i - \hat{r}_{i-1}}\right) \right] \tag{A42}$$

Note that  $\Delta \hat{r}_i^2 = \hat{r}_{i+1/2}^2 - \hat{r}_{i-1/2}^2$  is a measure for the cell volume (per unit streamwise length, and unit angular displacement), applicable for cells which do not include the pole  $\hat{r} = 0$ . For the cell including the pole,  $\Delta \hat{r}_i^2 = \hat{r}_{i+1/2}^2 + \hat{r}_{i-1/2}^2$ , following [29]. This notation is different from the square of the cell length (for any cell)  $\Delta \hat{r}_i^2 \neq (\Delta \hat{r}_i)^2 = (\hat{r}_{i+1/2} - \hat{r}_{i-1/2})^2$ . In addition to the spatial discretization subindex i, we have also used the subindex n for temporal discretization. To that extent, Eq. (A42) is solved for the new velocity at cell i and discrete time n+1, i.e.,  $\underline{u}_{i,n+1}$ . The time-step for advancement is  $\Delta t = t_{n+1} - t_n$ .

Since we are using an explicit Euler time-advancement scheme,  $\Delta t$  needs to obey the CFL diffusion criterion for numerical stability. However, to the best of our knowledge, there is no clear basis for the calculation of such CFL criterion in the specific problem at discussion, i.e., a pseudo-polar coordinate  $\hat{r}$  grid, which is also irregular. On the basis of a rewriting of the second radial derivative associated with the diffusion term  $(\eta/\hat{r})d/d\hat{r}(\hat{r}d\underline{u}/d\hat{r})$ , as  $(\eta/\hat{r})d\underline{u}/d\hat{r} + \eta d^2\underline{u}/d\hat{r}^2$ , we suggest a CFL criterion which results from the most restrictive condition associated to both terms contributing to the cylindrical diffusion term. That is,

$$\Delta t = \min \left( C_{\text{CFL}} \frac{(\Delta \hat{r}_i)^2}{\eta}, C_{\text{CFL}} \frac{\Delta \hat{r}_i^2}{2\eta} \right) \quad \text{among all } i$$
 (A43)

Here, we consider the dimensionless safety factor  $C_{CFL} \leq 0.25$ . Note that  $C_{CFL} = 0.5$  is the theoretical CFL condition limit for diffusion in a 1-D equidistant grid. Our stability limit is taken conservatively as half of the equidistant grid limit. The first candidate for evaluation of  $\Delta t$  in Eq. (A43) is then the usual CFL diffusion criterion in Cartesian coordinates, which would correspond to the planar contribution to diffusion, i.e., the term  $\eta d^2 \underline{u}/d\hat{r}^2$ . Conversely, the second candidate for evaluation of  $\Delta t$  in Eq. (A43) is a normal deceleration term due to viscous friction, i.e., that linked to the contribution  $(\eta/\hat{r})d\underline{u}/d\hat{r}$ , noting that  $\hat{r}d\hat{r} = (1/2)d\hat{r}^2$ . This term only appears in cylindrical coordinates.

In the cylindrical 1-D grid, there is an additional issue which requires further consideration. Despite the fact that  $\Delta \hat{r}_i^2 \neq 0$  and  $(\Delta \hat{r}_i)^2 \neq 0$  for all i, it is possible that a given cell observes an interface  $\hat{r}_{i+1/2} \to 0$  or  $\hat{r}_{i-1/2} \to 0$ . In such cases, the explicit advancement of Eq. (A42) may effectively introduce an artificial boundary condition at said cell interface near the pole. Indeed, this would be an artificial homogeneous Neumann boundary condition, which would result in an apparent decoupling of the

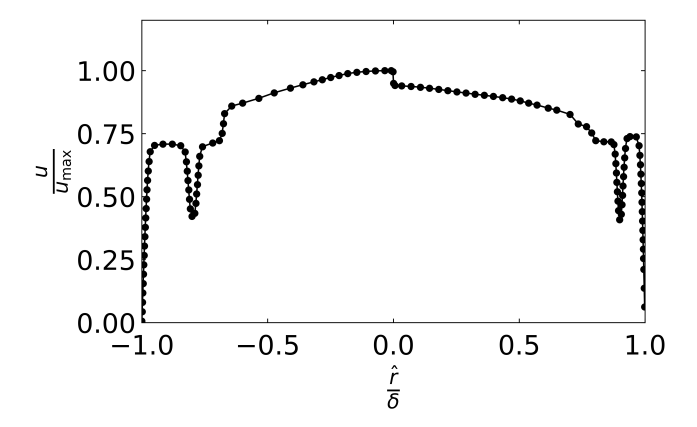
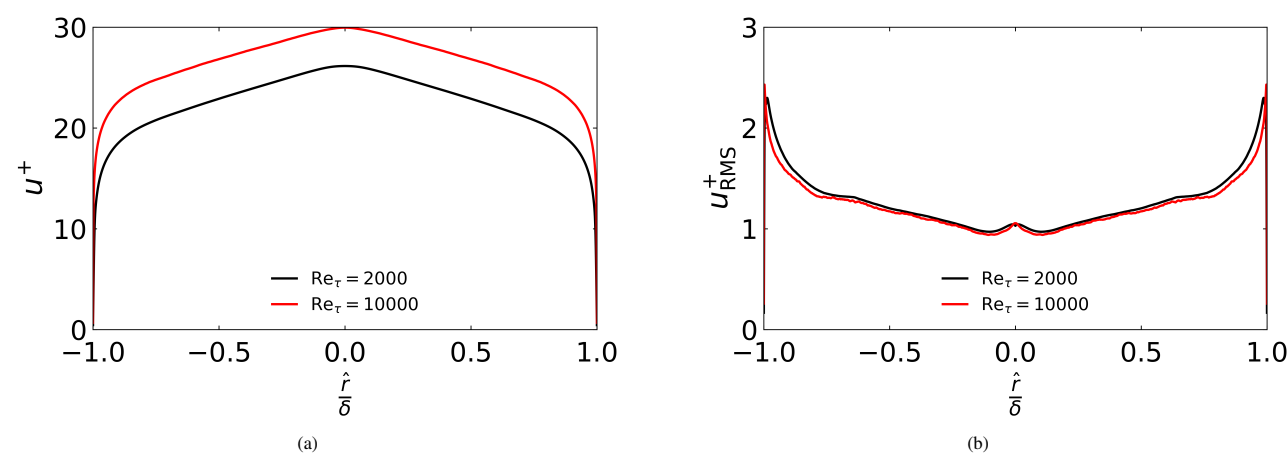


FIGURE A2 Developing flow velocity profile showing an apparent discontinuity around the pole when using the cylindrical ODT formulation.

semi-positive and semi-negative radial domains,  $\hat{r} > 0$  and  $\hat{r} < 0$ , respectively. This is another issue which is only relevant for the ODT formulation at discussion. In 3-D DNS, both cylindrical domains,  $\hat{r} > 0$  and  $\hat{r} < 0$ , would be coupled by the complementary azimuthal discretization of flow variables. Alternatively, in the case of the numerical solution of regular 1-D radial diffusion equations, e.g., for a laminar pipe flow, the symmetry of the solution prevents any related issue. However, in the ODT cylindrical formulation, asymmetries around the pole may arise due to the implementation of triplet maps crossing  $\hat{r} = 0$ . In this context, it is possible that the numerical solution found at any given discrete time after the deterministic advancement process exhibits an apparent discontinuity, or rather, numerical stiffness around the pole. This is shown in Figure A2.

We note that the presence of the apparent discontinuity or numerical stiffness around the pole in any given flow snapshot in the T-ODT cylindrical formulation does not necessarily lead to significant effects in the resulting flow statistics. Figures A3a and A3b show the mean and RMS streamwise velocity profiles across the entire radial grid for case 2000PT and 10000PT. The apparent formulation artifact at the pole does not seem to affect the mean velocity profiles in a significant way. There is no apparent dependency or effect due to lower or larger Reynolds numbers on the mean velocity profile either. The RMS velocity profile for case 2000PT exhibits a mild decrease very close to (or precisely at)  $\hat{r} = 0$ , as well as a moderate increase in the outer-layer region around  $\hat{r} = 0$ . This artifact is also affected by the simulated flow Reynolds number, since case 10000PT does not show the decrease in the RMS velocity at  $\hat{r} = 0$ . The affected domain range remains, in all cases, limited to a region of extent  $\leq 0.2\delta$  centered around  $\hat{r} = 0$ , i.e., a region of  $0.1\delta$  in both the semi-negative and semi-positive radial domains. During the time it took to finish this manuscript, several strategies were tested as a way to remediate the numerical ODT cylindrical artifact around the pole. One strategy was a method for artificial diffusion flux suppression close to  $\hat{r} = 0$ , which was similar to the one used by [41]. Said flux suppression method required specification of a suppression range in the numerical grid (additional model parameter), and it worsened the behavior of the artificial Neumann boundary condition. Thus, it performed in an undesirable way. Another tested strategy relied on the use of a symmetric cell around the pole, i.e., a cell with cell center at  $\hat{r}_{i=\text{center}} = 0$ , and faces at  $\hat{r}_{i=\text{center}-1/2} = -\Delta r_{i=\text{center}}/2$  and  $\hat{r}_{i=\text{center}+1/2} = \Delta r_{i=\text{center}}/2$ . This strategy required the specification of the center cell size  $\Delta r_{i=\text{center}}$ . Said center cell necessitated a size significantly larger than  $\delta_n$ . In this way, the mitigation strategy increased numerical diffusion around the pole, effectively coupling both half-domains  $\hat{r} < 0$  and  $\hat{r} > 0$ . Although the latter strategy was effective, it was numerically undesirable since it introduced additional numerical diffusion in order to enforce the size of the centered cell at the pole. It also introduced another model parameter to the formulation, namely  $\Delta r_{i=\text{center}}$ , which was also sensitive to the simulated flow Reynolds number. Yet another tested strategy was the use of an implicit Euler time integration scheme for the advancement of Eq. (A42). The motivation for this strategy was the uncertainty associated to the appropriate CFL stability criterion for explicit Euler advancement in the 1-D cylindrical grid. Since the artificial Neumann boundary condition results in numerical stiffness, it was believed that the use of an implicit time integration method could remediate these issues. However, the use of an implicit Euler scheme still yielded instantaneous profiles such as those shown in Figure A2.

In an effort to clarify the effects which may arise from the numerical artifact at the pole, consider the following situations. First, consider a plain 1-D laminar pipe-flow simulation with an irregular, yet fixed (static, not dynamic) grid, with a central element having a cell face position at  $\hat{r} = 0$ , in which an initial profile, asymmetric with respect to r = 0, diffuses over some time. Before reaching the steady state solution, we will always have 2 independent profiles for the semi-positive and semi-negative domain sides. Now consider the effect of eddy events in this simulation. In general, large velocity gradients favor the implementation of



**FIGURE A3** (a) Mean streamwise velocity pipe flow profile throughout the entire 1-D radial grid for cases 2000PT (Re<sub> $\tau$ </sub> = 2000) and 10000PT (Re<sub> $\tau$ </sub> = 10000). (b) RMS streamwise velocity pipe flow profile throughout the entire 1-D radial grid for cases 2000PT (Re<sub> $\tau$ </sub> = 2000) and 10000PT (Re<sub> $\tau$ </sub> = 10000).

eddy events. For infrequent turbulent transport, the centerline region of the numerical pipe is mostly unaffected by mappings, and the induced zero gradient due to diffusion next to r = 0 results in a feedback mechanism forbidding implementation of eddies around the centerline. This is a region of low mixing or laminarization centered around  $\hat{r} = 0$ , which is responsible for a sudden drop in the streamwise RMS velocity profile exactly at  $\hat{r} = 0$ . This is the situation seen in Figure A3b for case 2000PT. The local laminarization also implies that only larger (and infrequent) eddies are responsible for mixing around the centerline. The larger eddies, conversely, yield an additional artificial increase in the turbulence intensity close yet away from  $\hat{r} = 0$ . Since the frequency of implementation of eddy events increases with the Reynolds number, we expect that the numerical artifact around the pole is mitigated at larger Reynolds numbers. We partially see this in Figure A3b for case 10000PT, since the sudden drop due to laminarization in the streamwise RMS velocity profile exactly at  $\hat{r} = 0$  is attenuated in comparison to case 2000PT. More importantly, this also implies that ODT eddy events are the mechanism responsible for preserving the dynamical coupling between both the semi-negative and semi-positive radial domains in an otherwise laminar developing flow solution.

Based on our results, shortcomings, and discussion, we deliberately omitted the use of any remediating strategy for the numerical artifact at the pole in the final version of the results of this manuscript. Our goal and deliberate decision in this work was to maintain the simplicity of the formulation, while commenting on these issues. The pole artifact, despite not invalidating the obtained results, specially not those of the mean flow which is unaffected by them, must be carefully observed and considered when discussing the cylindrical ODT formulation. As commented in Section 4.5, the dynamic grid adaption strategy also introduces numerical diffusion. Future work should evaluate a cylindrical ODT formulation with a fixed (non-dynamic) grid, in which the cells are located in a way such that no face coincides with  $\hat{r} = 0$ . The best numerical accuracy would be obtained for an equidistant grid. Furthermore, a theoretically second-order accuracy for the spatial discretization could be obtained if the center of the cells in the 1-D domain corresponds to the centroid of the cylindrical volume, instead of the midpoint choice used here, see [55].

# A.3.2 S-ODT formulation

We begin the discussion of the numerical discretization applicable in S-ODT (specializing to the cylindrical formulation) with the corresponding momentum equation, Eq. (16),

$$\underline{u_{i,n+1}}u_{i,n+1}\frac{\left(\Delta\hat{r}_{i,n+1}^{2}\right)}{2} - \underline{u_{i,n}}u_{i,n}\frac{\left(\Delta\hat{r}_{i,n}^{2}\right)}{2} = \eta \int_{\Delta z} \left[ \left(\hat{r}_{i+1/2}\frac{\underline{u_{i+1}} - \underline{u_{i}}}{\hat{r}_{i+1} - \hat{r}_{i}}\right) - \left(\hat{r}_{i-1/2}\frac{\underline{u_{i}} - \underline{u_{i-1}}}{\hat{r}_{i} - \hat{r}_{i-1}}\right) \right] dz \tag{A44}$$

We have deliberately omitted the subindex n for all variables in the integral of the RHS. The reason for this will be explained next. Note that, in comparison with the T-ODT formulation, the grid cell positions and sizes now observe a subindex n to indicate the dynamic change in the grid cell interfaces due to the mass conservation enforcement as discussed in Section 2.2.3. As per the

logic of the FCE step, and also due to Eq. (15), the local cell-wise streamwise mass flux must remain constant. Furthermore, grid cell volume changes should occur during the FCE step, and not during the integration of the momentum equation. This suggests that Eq. (A44) may be rewritten as

$$\underline{u}_{i,n+1} - \underline{u}_{i,n} = \frac{\eta}{u_{i,n} \frac{(\Delta \hat{r}_{i,n}^2)}{2}} \int_{\Delta z} \left[ \left( \hat{r}_{i+1/2,n} \frac{\underline{u}_{i+1} - \underline{u}_i}{\hat{r}_{i+1,n} - \hat{r}_{i,n}} \right) - \left( \hat{r}_{i-1/2,n} \frac{\underline{u}_i - \underline{u}_{i-1}}{\hat{r}_{i,n} - \hat{r}_{i-1,n}} \right) \right] dz$$
(A45)

Upon consideration of Eq. (A45), there is the question of how to numerically evaluate the integral on the RHS. The easiest choice is an explicit Euler method for  $\underline{u}_i$ . In this context, previous S-ODT investigations have only used traditional forms of the CFL condition as Eq. (A43), in order to determine the size of the explicit advancement step  $\Delta z$ . However, the numerical stability discussion for cylindrical coordinates initiated for the T-ODT formulation gains now additional relevance in the S-ODT formulation. If the nature of the CFL condition in cylindrical coordinates was already opaque for time-dependent 1-D diffusion equations, it becomes entirely unclear when discussing Eq. (A45). Intuitively, or empirically, a locally u dependent CFL condition should be used in S-ODT in order to solve the momentum equation with an explicit integration method. This is due to the preceding (inverse) u term on the RHS of Eq. (A45). Concerning the magnitude of the advancement step, we could propose a modification on condition (A43) for the required streamwise advancement step  $\Delta z$  in S-ODT as

$$\Delta z = \min\left(C_{\text{CFL}}u_{i,n} \frac{\left(\Delta \hat{r}_{i,n}\right)^2}{\eta}, C_{\text{CFL}}u_{i,n} \frac{\Delta \hat{r}_{i,n}^2}{2\eta}\right) \quad \text{among all } i$$
(A46)

Unfortunately, in the case of the the turbulent pipe and channel flows evaluated in this work, the use of the condition (A46) for the estimation of  $\Delta z$ , and subsequent use of an explicit Euler advancement scheme for Eq. (A45) resulted, in almost all cases, in unstable S-ODT simulations. It is noted that any appearance of velocity values u < 0 in S-ODT immediately forbids simulation progress. This is because negative streamwise velocities indicate recirculation, and therefore, a violation of the parabolic flow assumptions required for streamwise marching schemes. Appearance of negative velocity values using condition (A46), usually occurred near the walls. In the specific case of the cylindrical formulation, since we were using the model parameter  $\alpha = 0$  as well as equal (uniform zero) initial conditions for azimuthal and radial velocity components w and v, respectively, the appearance of values u < 0 could only be attributed to numerical instabilities. However, we note that instabilities of the same type also occurred for S-ODT channel flows. Recall also that, for both planar and cylindrical formulations, the FCE step cannot yield negative velocities if the input velocity field is entirely positive. This is because the FCE step is merely a multiplicative correction step. Based on condition (A46), it is clear that the most critical condition for determination of  $\Delta z$  is located near the walls, where  $u_i$  values are smaller, the velocity gradient is steepest, and consequently,  $\Delta \hat{r}_i$  (or  $\Delta y_i$  in the planar formulation) is also smaller due to the dynamically adaptive grid.

In order to overcome stability issues, we have found a compromise for the S-ODT numerical advancement of Eq. (A45), and that is to use an implicit scheme for the evaluation of the RHS integral. In practice, we use a Crank-Nicolson time-integration method of the following form

$$\left(\underline{u}_{i,n+1}^{*} - \underline{u}_{i,n}\right) = \frac{\Delta z}{u_{i,n}\left(\Delta \hat{r}_{i,n}^{2}\right)} \left\{ \eta \left[ \left(\hat{r}_{i+1/2,n} \frac{\underline{u}_{i+1,n+1}^{*} - \underline{u}_{i,n+1}^{*}}{\hat{r}_{i+1,n} - \hat{r}_{i,n}}\right) - \left(\hat{r}_{i-1/2,n} \frac{\underline{u}_{i,n+1}^{*} - \underline{u}_{i-1,n+1}^{*}}{\hat{r}_{i,n} - \hat{r}_{i-1,n}}\right) \right] + \eta \left[ \left(\hat{r}_{i+1/2,n} \frac{\underline{u}_{i+1,n} - \underline{u}_{i,n}}{\hat{r}_{i+1,n} - \hat{r}_{i,n}}\right) - \left(\hat{r}_{i-1/2,n} \frac{\underline{u}_{i,n} - \underline{u}_{i-1,n}}{\hat{r}_{i,n} - \hat{r}_{i-1,n}}\right) \right] \right\}$$
(A47)

A similar numerical method is used for the planar formulation. As in Section 2.2.3, we have used  $\underline{u}^*$  to indicate the predictor value of the velocity field at coordinate  $z_{n+1}$  resulting from the advancement of Eq. (16). Said predictor value is corrected next in the FCE step, see Section 2.2.3.

The FVM discretization of Eq. (15), which is required in order to calculate the new Lagrangian radial cell sizes as demanded by Eq. (17), is

$$u_{i,n+1}^* \frac{\Delta \hat{r}_{i,n+1}^{2*}}{2} = u_{i,n} \frac{\Delta \hat{r}_{i,n}^2}{2}$$
 (A48)

Here, the updated values of  $u_{i,n+1}^*$  from the momentum PDE advancement, Eq. (A47), are used in order to calculate the new cell sizes  $\Delta \hat{r}_{i,n+1}^{2*}$ . This is the Lagrangian volume deformation step from previous unconfined S-ODT formulations, see [22, 29, 34]. In unconfined flow formulations, the newly calculated 1-D cells are arranged starting with one of the two fixed wall positions. In the novel confined flow S-ODT formulation, the latter cell rearrangement step is omitted. The Lagrangian volume deformation

step is followed directly by the FCE corrector step, involving a new adjustment of the cell sizes in order to comply with the confinement due to the walls. To that extent, the correction factor  $\Gamma$  is calculated as per Eq. (18). In discrete cylindrical grid notation,  $\Gamma$  takes the form

$$\Gamma = \frac{\sum_{i} \Delta \hat{r}_{i}^{2}}{\sum_{i} \Delta \hat{r}_{i,n+1}^{2*}} \tag{A49}$$

Said factor  $\Gamma$  is then used to correct  $\Delta \hat{r}_{i,n+1}^{2*}$ , as well as the predicted velocity values  $u_{i,n+1}^*$  such that

$$\Delta \hat{r}_{i,n+1}^2 = \Gamma \Delta \hat{r}_{i,n+1}^{2*}, \qquad u_{i,n+1}^{\dagger} = \frac{u_{i,n+1}^*}{\Gamma}$$
 (A50)

The corrected cells are now rearranged starting with one of the two fixed wall positions. The FCE corrector step allows the last cell edge to coincide with the position of the other wall. We note that cell interface rearrangement in the S-ODT cylindrical formulation is based on the readjustment of cell volumes  $\Delta \hat{r}^2$  in a way in which these are forced to obey the confinement constraint due to the pipe walls. In the planar formulation, cell interface rearrangement follows regular enforcement of cell sizes  $\Delta y$  instead (here omitting cell indices i for generality). It may be relevant to stress that advective transport due to the shifting of cell interfaces, or more specifically, the Lagrangian cell interface velocity, is defined precisely in terms of the displacement of the cell interfaces (a distance), and not in terms of cell volumes. The latter could be considered an added consideration of the effect of radial stretching in the advective transport effect, which is our current interpretation. Nonetheless, it could also be interpreted as another potentially different form of transport, not purely advective. We do not elaborate further on this conjecture.

This concludes the implementation of the deterministic S-ODT advancement process, including the FCE corrector step. The new cell sizes and velocities,  $\Delta \hat{r}_{i,n+1}$  and  $u_{i,n+1}^{\dagger}$ , are taken as the values of cell sizes and velocities for the beginning of a new streamwise advancement cycle, respectively. Although the FCE was previously explained with reference to the deterministic advancement, it is likewise applied during eddy events, as commented in Section 2.2.1. In such case, the velocity  $u_{i,n+1}^*$  refers instead to the discrete mapped and kernel transformed velocity, which will be used for an alternative FCE corrector step for S-ODT eddy events, following the same logic given by Eqs. (A48) and (A50).

We remark that the FCE step implies an additional coupling of both semi-negative and semi-positive radial domains due to the cell interface shifting (advection), which is not present in the T-ODT formulation. As such, the FCE step may introduce other issues related to the previously commented T-ODT numerical artifact of domain decoupling (due to artificial boundary conditions at  $\hat{r} = 0$ ). In principle, the artificial discontinuity at the pole may shift positions due to the cell rearrangement implied in the FCE step for the cylindrical S-ODT formulation. This may result in worsened statistical flow moments evaluated using flux balance schemes, see Appendix A.5. In any case, the inherent coupling of both semi-negative and semi-positive radial domains during the FCE step under the presence of numerical stiffness at the pole (due to the artificial homogeneous Neumann boundary condition), would result in a very large advective transport contribution.

Previous comments made for the T-ODT formulation concerning alleviation of the numerical artifact around the pole at larger Reynolds number flows should still be valid in the context of the S-ODT formulation. However, we have not evaluated this directly in the present work, since we only carried out S-ODT simulations at one specific  $Re_{\tau}$ , see Section 3.

### A.4 Considerations on the dynamical mesh-adaption procedure

A detailed description of the dynamical mesh-adaption operations taking place in ODT can be found in [22]. The adaptive grid ODT code has been used extensively in previous investigations for both temporal and spatial formulations, e.g., [27, 29]. Nonetheless, details regarding the conservative operations for cell merging and splitting have not been discussed in detail in any publication other than that of [22]. Given that this work discusses conservative T-ODT and S-ODT formulations, it is of interest to briefly mention some related issues here.

## A.4.1 Cell merging and splitting in T-ODT

We limit the discussion of this section to the T-ODT constant density cases evaluated in the present work. In constant density, local conservation of mass in a cell is trivial, as discussed in Section 2.1.2. Cell property profiles are assumed constant within cells. The splitting of cells during dynamical mesh-adaption is resolved here in the most straightforward way. The neighboring cells are partitioned by length in the planar formulation (and by volume in the cylindrical formulation) while maintaining the

properties uniform or constant within the partitioned cells. In this way, the splitting operation is fully conservative. Merging of two cells during mesh adaption observes mass and momentum conservation, such that the merging operation is also fully conservative. The mass of each cell previous to the merge operation is calculated as  $\rho\Delta\xi_i^{m+1}/(m+1)$ . For the merge of two cells, say i and i+1, mass conservations implies, for constant density, that the merged cell has mass  $\rho\Delta\Omega$ , where  $\Delta\Omega$  is the volume of the resulting merged cell,

$$\rho\Delta\Omega = \rho \left[ \frac{\Delta\xi_i^{m+1}}{m+1} + \frac{\Delta\xi_{i+1}^{m+1}}{m+1} \right], \quad \text{which simplifies to} \quad \Delta\Omega = \left[ \frac{\Delta\xi_i^{m+1}}{m+1} + \frac{\Delta\xi_{i+1}^{m+1}}{m+1} \right]$$
 (A51)

Algorithmically, Eq. (A51) is implemented by setting the boundaries of the merged cell as the opposite extreme boundaries of the neighbor cells i and i + 1 undergoing the merge operation. This implies then volume conservation during cell merging. Any velocity component  $u_{k,M}$  (for  $k \in \{1, 2, 3\}$ ) at the merged cell M is then calculated for momentum conservation as

$$u_{k,M} = \frac{\rho u_{k,i} \frac{\Delta \xi_i^{m+1}}{m+1} + \rho u_{k,i+1} \frac{\Delta \xi_{i+1}^{m+1}}{m+1}}{\rho \Delta \Omega}, \quad \text{which simplifies to} \quad u_{k,M} = \frac{u_{k,i} \Delta \xi_i^{m+1} + u_{k,i+1} \Delta \xi_{i+1}^{m+1}}{\Delta \xi_{i+1}^{m+1} + \Delta \xi_{i+1}^{m+1}}$$
(A52)

Note that although (specific) mass and momentum are conserved during cell merging upon application of Eq. (A51) and (A52), (specific) kinetic energy,  $u_k u_k/2$  (considering the Einstein summation rule), cannot be simultaneously conserved. This is because the application of the procedure given by Eq. (A52) for two cells observing  $u_{k,i}u_{k,i}/2$  and  $u_{k,i+1}u_{k,i+1}/2$ , does not yield the same result as  $u_{k,M}u_{k,M}/2$ . Therefore, the cell merging operation introduces numerical diffusion in the form of loss of conservation (dissipation) of kinetic energy. As evidenced by the T-ODT results presented in this work, see specifically Section 4.5, this numerical effect is deemed negligible in the T-ODT planar formulation. The effect is also small, yet noticeable, in the T-ODT cylindrical formulation.

## A.4.2 Cell merging and splitting in S-ODT

S-ODT conservation laws require numerical flux balance before and after the cell splitting and cell merge operations. The splitting of cells may be carried out as in T-ODT, such that the procedure remains as a fully conservative operation in S-ODT. Having said that, an important issue is present during cell merging. The streamwise mass flux of each cell previous to the merge can be calculated, using  $u_k$  for k = 3 (the streamwise velocity component), as  $\rho u_3 \Delta \xi_i^{m+1}/(m+1)$ . For the merge of cells i and i+1, considering constant density, the merged cell M observes a resulting streamwise mass flux  $\rho u_{3,M,U} \Delta \Omega_U$  such that

$$\rho u_{3,M,U} \Delta \Omega_U = \rho \left[ u_{3,i} \frac{\Delta \xi_i^{m+1}}{m+1} + u_{3,i+1} \frac{\Delta \xi_{i+1}^{m+1}}{m+1} \right], \quad \text{which simplifies to} \quad u_{3,M,U} \Delta \Omega_U = u_{3,i} \frac{\Delta \xi_i^{m+1}}{m+1} + u_{3,i+1} \frac{\Delta \xi_{i+1}^{m+1}}{m+1}$$
 (A53)

In traditional unconfined S-ODT flow formulations, see [22, 29], merged momentum fluxes for velocity components  $u_{k,M,U}$  at cell M (here using the subindex U to indicate reference to the unconfined flow formulation), are calculated upon observation of Eq. (A53) as

$$\rho u_{3,M,U} u_{k,M,U} \Delta \Omega_U = \rho \left[ u_{3,i} u_{k,i} \frac{\Delta \xi_i^{m+1}}{m+1} + u_{3,i+1} u_{k,i+1} \frac{\Delta \xi_{i+1}^{m+1}}{m+1} \right], \quad \text{leading to} \quad u_{k,M,U} = \frac{u_{3,i} u_{k,i} \Delta \xi_i^{m+1} + u_{3,i+1} u_{k,i+1} \Delta \xi_{i+1}^{m+1}}{u_{3,i} \Delta \xi_i^{m+1} + u_{3,i+1} \Delta \xi_{i+1}^{m+1}} \quad (A54)$$

Upon calculation of  $u_{k,M,U}$ , and more specifically, of  $u_{3,M,U}$  by Eq. (A54),  $\Delta\Omega_U$  from Eq. (A53) can be calculated as

$$\Delta\Omega_U = \frac{u_{3,i} \frac{\Delta \xi_i^{m+1}}{m+1} + u_{3,i+1} \frac{\Delta \xi_{i+1}^{m+1}}{m+1}}{u_{3,M,U}}$$
(A55)

The calculation of  $\Delta\Omega$  by Eq. (A55), using  $u_{3,M,U}$  determined by Eq. (A54), implies a change in the resulting volume by the two merged cells. This transforms, globally, into a violation of the confinement constraint required for the present confined flow S-ODT formulation. To that extent,  $\Delta\Omega_U$  is substituted by  $\Delta\Omega_C$  (confined) calculated instead for volume conservation as in the T-ODT formulation for  $\Delta\Omega$ , Eq. (A51). For the determined  $\Delta\Omega_C$ , the merged streamwise velocity  $u_{3,M,C}$  for confined flow at cell M can then be calculated by Eq. (A53) as

$$u_{3,M,C} = \frac{u_{3,i} \Delta \xi_i^{m+1} + u_{3,i+1} \Delta \xi_{i+1}^{m+1}}{\Delta \xi_i^{m+1} + \Delta \xi_{i+1}^{m+1}}$$
(A56)

In practice, this simply implies that Eq. (A54) can be used for confined flow with the exception of the velocity component k = 3, which must be calculated using Eq. (A56). This in turn implies that, while the streamwise mass flux is numerically balanced before and after a cell merging operation, the momentum flux due to streamwise advection  $\rho u_{3,M,C}u_{3,M,C}\Delta\Omega_C$  is not. This is partly the reason why the mesh adaption procedure in S-ODT is seen to have a larger numerical diffusion effect in the calculation of contributions to the streamwise momentum as seen in Section 4.5.

## A.5 Reynolds stresses and TKE budgets

As shown in Kerstein et al. [32], equivalences between DNS and ODT statistical quantities can be established by comparing the mean ODT and RANS momentum equations. We illustrate these equivalences with reference to Reynolds stresses and turbulent kinetic energy (TKE) budgets. For planar geometry, the findings in Kerstein et al. [32] for T-ODT are summarized next, and then extended to S-ODT by following the strategy outlined by [34]. Afterwards, we introduce the equivalences for the cylindrical geometry. For convenience, we rely on an index notation for the velocity vector,  $u_k$ , where  $k \in \{1, 2, 3\}$  are the spanwise, wall-normal, and streamwise components in the planar Cartesian formulation, while  $k \in \{1, 2, 3\}$  are the azimuthal, radial, and streamwise components in the cylindrical formulation. As usual, constant density  $\rho$  and kinematic viscosity  $\eta$  are assumed.

### **A.5.1** Planar T-ODT formulation

A mathematical representation of the T-ODT momentum evolution equation in the planar case is obtained by rewriting Eq. (9) for Cartesian coordinates, in an Eulerian framework and a differential form. This is,

$$\frac{\partial u_k}{\partial t} = -\frac{1}{\rho} \frac{\mathrm{d}\overline{p}}{\mathrm{d}z} \delta_{k3} + \eta \frac{\partial^2 u_k}{\partial y^2} + M_k + K_k. \tag{A57}$$

We have used  $\delta_{k3}$  as a delta operator with  $\delta_{k3} = 1$  for k = 3, and  $\delta_{k3} = 0$  for  $k \neq 3$ . We retain the use of the index notation and of dz, and  $\partial y$ , for clarity. There is no mean flow in direction y aligned with the ODT domain. The turbulent advection is represented by eddy events.  $M_k + K_k$  stands for the combined effects of the triplet-map  $(M_k)$  and kernel  $(K_k)$  operations on the ODT velocity component  $u_k$  [32]. This also follows the notation introduced by Eq. (2).  $K_k$  can be formally decomposed into transport and scrambling contributions, symbolically  $K_k = T_k + S_k$ , where scrambling refers to momentum changes due to TKE redistribution among velocity components. Momentum conservation requires  $S_k$  to integrate to zero, but apart from this constraint, there is no unique way to decompose  $K_k$  as indicated. The choice  $S_k = 0$  is preferred due to the absence of momentum scrambling contributions in the mean Navier-Stokes momentum equation [32], so  $K_k$  is replaced by  $T_k$  in what follows.

It is instructive to compare Eq. (A57) with the steady state channel flow RANS momentum equation,

$$0 = -\frac{1}{\rho} \frac{d\overline{\rho}}{dz} + \eta \frac{\partial^2 \overline{u_3}}{\partial y^2} - \frac{\partial \overline{v'u_3'}}{\partial y}$$
 (A58)

Note that we have resorted to the notation  $\overline{v'u'_3}$  to indicate the Reynolds shear stress. Converse to Eq. (A58), the mean T-ODT momentum evolution is,

$$0 = -\frac{1}{\rho} \frac{d\overline{\rho}}{dz} + \eta \frac{\partial^2 \overline{u_3}}{\partial y^2} + \overline{M_3} + \overline{T_3}$$
 (A59)

Here and for all other formulations considered in the appendix, we invoke statistical stationarity unless noted otherwise, allowing us to perform a temporal Reynolds averaging, denoted by overbars, and to set the time-derivative of the averaged streamwise velocity to zero in the averaged equation, i.e.,  $\partial \overline{u_3}/\partial t = 0$ . For time-developing flow, the Reynolds averaging would be applied at chosen instants or in chosen time windows to an ensemble of simulated flow realizations and  $\partial \overline{u_3}/\partial t$  would be retained as a nonzero value. It is straightforward to verify that the Reynolds stress component  $\overline{v'u'_3}$  in the T-ODT planar case is given by

$$I_3 \equiv -\int_{-\delta}^{y} (\overline{M_3} + \overline{T_3}) \mathrm{d}y^* = \overline{v'u_3'}.$$
 (A60)

We have introduced the notation  $I_3$  to indicate the equivalence with the Reynolds stress. We note that, in the context of the turbulent transport or Reynolds stress,  $v' \neq u'_2$  in ODT. Here,  $u_2$  is the velocity component which decides upon implementation of eddy events according to the eddy frequency formula  $(\Delta t_l)^{-1}$ , Eq. (5), and which is subject to the numerical integration of its

corresponding transport PDE. Conversely, v' in the present context is a representative ODT fluctuating contribution, which can not be determined directly, and which is responsible for the turbulent (advective) transport.

There are different ways in which Eqs. (A59) and (A60) can be used to evaluate the Reynolds stress in ODT. The first one is to apply the integration with respect to the wall-normal coordinate in Eq. (A59), while solving for the equivalence of the integral of  $\overline{M_3} + \overline{T_3}$  given by Eq. (A60), i.e., the Reynolds stress  $\overline{v'u'_3}$ . This is precisely the evaluation carried out by Eq. (26) in Section 5, which enables the evaluation of the unknown  $\overline{v'u'_3}$  given the imposed FPG and the mean velocity profile  $\overline{u_3}$  determined from simulation output. Another way is to evaluate the y profile of  $\overline{M_3} + \overline{T_3}$  based on the time rate of eddy-induced change of  $u_3$  as a function of y. Operationally, this is done at given y using the estimate

$$\frac{\sum_{\text{eddies}} (\Delta u_3)}{\Delta t} = \overline{M_3} + \overline{T_3} \tag{A61}$$

The time interval  $\Delta t$  is the total one resulting from aggregated sampling time intervals, such that it is consistent with the summation indicated in the numerator of Eq. (A61) (note that if an eddy is sampled but not implemented, there is no change in the velocity profile). We remark that the evaluation of  $\overline{M_3} + \overline{T_3}$  refers to changes  $\Delta u_3$  that are caused by triplet maps and kernel procedures.

The availability of distinct methods for evaluating  $\overline{v'u'_3}$  is a consequence of statistical stationarity, which assures that the overall  $\Delta u_3$  changes induced by the T-ODT deterministic viscous advancement are locally balanced over time by the stochastic eddy-induced changes. In this sense, it is important to stress that a more faithful version of Eq. (A59) would imply replacing the FPG source term and the diffusion term by another term  $\overline{D_3}$  which involves all changes induced by the T-ODT deterministic viscous advancement. That is, for a given y,

$$\overline{D_3} = \frac{\sum_{\text{d. adv.}} (\Delta u_3)}{\Delta t} \approx -\frac{1}{\rho} \frac{d\overline{p}}{dz} + \eta \frac{\partial \overline{u_3}}{\partial z}$$
(A62)

As per Eq. (A59) and (A62), it is only possible to equate  $\overline{D}$  with the sum of  $(-1/\rho)\mathrm{d}\overline{\rho}/\mathrm{d}z$  and  $\eta\partial^2\overline{u_3}/\partial y^2$ , as long as the accumulation of said  $(-1/\rho)\mathrm{d}\overline{\rho}/\mathrm{d}z$  and  $\eta\partial^2u_3/\partial y^2$  over all deterministic advancement steps (d. adv. notation in Eq. (A62)) equate the averages of the said average pressure gradient and the viscous term. For the pressure gradient, this is not an issue, since it is simply a constant. However, the sum of the different viscous terms integrated in time does not necessarily equal the viscous diffusion of the average velocity  $\overline{u_3}$ . Several factors may contribute to the discrepancies. Examples are the way in which the values of the velocity are sampled to form  $\overline{u_3}$  (e.g., during the deterministic advancement or during eddy events, or considering an average between them), the numerical diffusion due to mesh adaption which is not included in the balance equation (A59), and even the time-integration method used to solve the deterministic advancement with its associated truncation error (the latter being accumulated in Eq. (A62)). Therefore, the availability of both calculation methods for  $\overline{v'u'_3}$  is useful in practice for code verification, since only the calculation method by Eq. (A60) using Eq. (A61), satisfies the average balance of momentum in ODT with the counterpart of Eq. (A62).

For the evaluation of the TKE budgets, the starting point is the momentum evolution equation, Eq. (A57), multiplied by  $u_k$ , which leads to the ODT kinetic energy transport equation for velocity component  $u_k$ ,

$$\frac{1}{2}\frac{\partial u_k^2}{\partial t} = -\frac{u_3}{\rho}\frac{\mathrm{d}\overline{p}}{\mathrm{d}z}\delta_{k3} + \eta u_k \frac{\partial^2 u_k}{\partial v^2} + \frac{1}{2}\left(M_{kk} + K_{kk}\right) \tag{A63}$$

This expression is rewritten with the help of some algebra as

$$\frac{\partial u_k^2}{\partial t} = -\frac{2u_3}{\rho} \frac{\mathrm{d}\overline{p}}{\mathrm{d}z} \delta_{k3} + \eta \frac{\partial^2 u_k^2}{\partial y^2} - 2\eta \left(\frac{\partial u_k}{\partial y}\right)^2 + M_{kk} + K_{kk}. \tag{A64}$$

In the last two terms, the subscript kk generically denotes that the average is evaluated by replacing  $\Delta u_k$  from Eq. (A61), by  $\Delta(u_k u_k)$ , where the summation in the modified equation is over triplet map (kernel) contributions for  $M_{kk}$  ( $K_{kk}$ ). Note that we have used  $u_k M_k = (1/2) M_{kk}$ , since  $u_k \Delta u_k$  could in principle be rewritten as  $\Delta u_k^2 = (1/2) \Delta(u_k u_k)$ . The kernel term in Eq. (A64) is now expressed as  $K_{kk} = T_{kk} + S_{kk}$ . Note also that we omit the application of the Einstein summation rule over repeated indices for clarity. This is the case in Eq. (A64) and elsewhere in this Appendix, unless otherwise noted.

We now pursue a derivation of the generalized T-ODT TKE equation which is valid both for steady and unsteady flows. To that extent, Eq. (A64) is averaged without invoking statistical stationarity. The identity  $\overline{u_k^2} - \overline{u_k}^2 = \overline{u_k'^2}$ , the definition  $I_{kk} = -\int_{-\kappa}^{y} (\overline{M_{kk}} + \overline{T_{kk}}) dy^*$ , as well as the subtraction of Eq. (A59) multiplied by  $2\overline{u}_k$ , yield the equation for the average of the

square of the fluctuation velocity  $u'_k$ , see [32] for details,

$$\frac{\partial \overline{u_k'^2}}{\partial t} = \eta \frac{\partial^2 \overline{u_k'^2}}{\partial y^2} - 2\eta \overline{\left(\frac{\partial u_k'}{\partial y}\right)^2} - \left[\frac{\partial}{\partial y} \left(I_{kk} - 2\overline{u_k}I_k\right) - \overline{S_{kk}}\right] - 2I_k \frac{\partial \overline{u_k}}{\partial y}.\tag{A65}$$

It is noted that a subtraction and addition of  $2I_k\partial \overline{u_k}/\partial y$  is required in order to obtain the final expression.

The time derivative term of the average of the square of the fluctuation velocity  $u'_k$  on the LHS of Eq. (A65) can be neglected if the statistical stationarity of the flow is invoked. Comparing Eq. (A65) to the generalized TKE equation in a Cartesian coordinate system (see, e.g., Eq. (5.164) in [12]), it follows that the advancement equation for TKE =  $(1/2)(\overline{u'_1^2} + \overline{u'_2^2} + \overline{u'_3^2})$  is obtained by summing the advancement equations for  $\overline{u'_1^2}$ ,  $\overline{u'_2^2}$ , and  $\overline{u'_3^2}$  and multiplying by 1/2. As in Kerstein et al. [32], the resulting terms for production  $P_{\text{ODT}}$ , dissipation  $\varepsilon_{\text{ODT}}$ , viscous transport  $\mathcal{T}_{V,\text{ODT}}$ , and advective transport  $\mathcal{T}_{A,\text{ODT}}$  of the TKE budgets are,

$$P_{\text{ODT}} = -\sum_{k} I_{k} \frac{\partial \overline{u_{k}}}{\partial y}, \quad \varepsilon_{\text{ODT}} = \sum_{k} \eta \overline{\left(\frac{\partial u_{k}'}{\partial y}\right)^{2}}, \quad \mathcal{T}_{V,\text{ODT}} = \frac{\eta}{2} \sum_{k} \frac{\partial^{2} \overline{u_{k}'^{2}}}{\partial y^{2}}, \quad \mathcal{T}_{A,\text{ODT}} = \frac{1}{2} \sum_{k} \left[\frac{\partial}{\partial y} \left(I_{kk} - 2\overline{u_{k}}I_{k}\right) - \overline{S_{kk}}\right], \quad (A66)$$

As detailed in [32],  $\sum_k \overline{S_{kk}} = \sum_k S_{kk} = 0$  because scrambling is defined as energy-conserving TKE redistribution among velocity components at given y without changing the total TKE. (Kernel-induced change of the total TKE at given y is attributed to kernel-induced transport of individual velocity components, which is subsumed in the terms  $T_{kk}$ .) Therefore, no assumption about the partition of  $K_{kk}$  into contributions  $T_{kk}$  and  $S_{kk}$  for given k is required in order to evaluate the average of  $\sum_k T_{kk}$  because the latter is equal to the average of  $\sum_k K_{kk}$ , whose evaluation follows from the discussion below Eq. (A64).

It is noted that the formula for  $\varepsilon_{ODT}$  in Eq. (A66) is based on time-averages of the mean velocity profile and of the streamwise kinetic energy profile. The discussion in this case is similar to the one before requiring the distinction between the average pressure gradient and the average viscous term with the term  $\overline{D_3}$ . Although, in general, the differences between  $\overline{D_3}$  and  $(-1/\rho)d\overline{\rho}/dz + \eta\partial^2\overline{u_3}/\partial y^2$  are not very significant, it is expected that there are larger differences in Eq. (A65) when average profiles are used instead of the actual balance terms for the calculation of both  $\mathcal{T}_{V,\text{ODT}}$  and  $\varepsilon_{\text{ODT}}$ . This is because both the viscous transport and dissipation terms are nonlinear functions of the velocity profile. Additionally, the symbolic multiplication by  $u_3$  used to obtain Eq. (A64) is only adequate for a specific type of numerical integration of the ODT momentum equation, given that there is no kinetic energy equation being solved directly in ODT. This motivates the introduction of the alternative dissipation term  $\varepsilon_{\text{bal}}$  discussed in Section 5, which enforces the correct balance in Eq. (A65). Last, we comment on the so-called advective transport term in ODT,  $\mathcal{T}_{A,\text{ODT}}$ . As previously explained in [32], the lack of explicit representation of pressure fluctuations in ODT precludes the partitioning of advective transport into turbulent transport and pressure transport as they are usually defined based on Navier-Stokes analysis. Therefore, these Navier-Stokes terms are combined for the purpose of comparison to ODT results. Pressure-fluctuation effects are implied by ODT eddies because they idealize turbulent motions that are driven by local unsteady pressure gradients. No attempt has been made to infer the pressure fluctuations that the eddies imply, although the novel confined S-ODT formulation is suggestive in this regard, see next.

#### A.5.2 Planar S-ODT formulation

The instantaneous momentum evolution in the spatial formulation is obtained by rewriting Eq. (16) for Cartesian coordinates, in an Eulerian framework and a differential form. This is,

$$\frac{\partial u_3 u_k}{\partial z} = \eta \frac{\partial^2 u_k}{\partial v^2} + M_k + T_k + A_k + F_k \tag{A67}$$

Although the overall framework discussed here is motivated in Appendix C of [21], in the sense that Eq.(A67) is related to truncated forms of the Navier-Stokes equations, a unique formal mathematical derivation based on the terms in the full Navier-Stokes equation has not been identified. The reduced 1-D formulation lacks, in this context, relevant mechanisms of physically consistent local and instantaneous 3-D flow. One consequence, noted at the end of A.5.1, is that all ODT advective transport must be lumped into one TKE budget term because there is no basis for discriminating the individual contributions to advective transport. S-ODT advective transport operations that are lumped in this way are those appearing also in the temporal formulation. On one hand,  $M_k$  and  $K_k$ , is used as in Eq. (10), with the substitution of  $K_k$  by  $K_k$  as in A.5.1. On the other hand, the additional term  $K_k$  denotes the advective part of the FCE step, as described in Section 2.2.3, while  $K_k$  denotes the forcing effect of the FCE step, which is analogous to a pressure-gradient forcing term, but it is unsteady and nonuniform in  $K_k$ .

A necessary condition in order to compare with the traditional RANS momentum equation is to perform an averaging procedure on Eq. (A67). Invoking streamwise homogeneity (although the more general case of spatially developing flow can also be treated) after applying a streamwise Reynolds averaging to Eq. (A67), analogous to the temporal averaging in Eq. (A59), gives

$$0 = \eta \frac{\partial^2 \overline{u_3}}{\partial v^2} + \overline{M_3} + \overline{T_3} + \overline{A_3} + \overline{F_3}. \tag{A68}$$

Analogously to T-ODT,  $\overline{M_k}$  and  $\overline{T_k}$  in Eq. (A68) are the mean rates of change relative to z that are induced by triplet maps and kernels, respectively. In contrast to the temporal data-reduction procedure expressed symbolically by Eq. (A61), the rate of eddy-induced change of the flux of  $u_k$  (due to  $u_3$ ) in S-ODT per streamwise interval  $\Delta z$  is

$$\frac{\sum_{\text{eddies}} \Delta (u_3 u_k)}{\Delta z} = \frac{\sum_{\text{eddies}} \left\{ u_3(f(y)) u_k^*(y) - u_3(y) u_k(y) \right\}}{\Delta z} = \overline{M_k} + \overline{T_k}. \tag{A69}$$

The notation  $u_k(f(y))$  corresponds to the (planar) mapped profile of the velocity  $u_k$ , while  $u_k(y)$  is the corresponding profile prior to mapping during an eddy event.  $u_k^*(y)$  here denotes the velocity component upon application of triplet map and kernel effects,  $u_k(f(y)) + c_kK(y) + b_kJ(y)$ . The summation on the LHS of Eq. (A69) implies a summation over eddy events.

The sum  $\overline{A_k} + \overline{F_k}$  is the mean rate of FCE-induced change of the momentum flux relative to z, as explained in Section 2.2.3. During an eddy event, the FCE induces a momentum flux change (due to  $u_3$ ) from  $u_3(f(y))u_3^*(y)$  to  $u_3^{2\dagger}(y^{\dagger})$  for velocity component k = 3, and from  $u_3(f(y))u_k^*(y)$  to  $u_3^{\dagger}(y^{\dagger})u_k^*(y^{\dagger})$  for components  $k \neq 3$ . We use  $y^{\dagger}$  here to indicate the grid resulting after application of the FCE step. For deterministic advancement, in order to simplify the notation, we note  $u_{k,n+1}^{\dagger}(y_{n+1})$  simply as  $u_k^{\dagger}(y^{\dagger})$ , and we take similar considerations noting  $u_n(y_n)$  as u(y), or  $u_{k,n+1}^*(y_n)$  as  $u_k^*(y)$ . On this basis,  $\overline{A_k} + \overline{F_k}$  is evaluated as

$$\overline{A}_{k} + \overline{F}_{k} = \left(\frac{\sum_{\text{eddies}} \left[u_{k}^{2\dagger}(y^{\dagger}) - u_{3}(f(y))u_{k}^{*}(y)\right]}{\Delta z} + \frac{\sum_{\text{d. adv.}} \left[u_{k}^{2\dagger}(y^{\dagger}) - u_{3}(y)u_{k}^{*}(y)\right]}{\Delta z}\right) \delta_{k3} + \left(\frac{\sum_{\text{eddies}} \left[u_{3}^{\dagger}(y^{\dagger})u_{k}^{*}(y^{\dagger}) - u_{3}(f(y))u_{k}^{*}(y)\right]}{\Delta z} + \frac{\sum_{\text{d. adv.}} \left[u_{3}^{\dagger}(y^{\dagger})u_{k}^{*}(y^{\dagger}) - u_{3}(y)u_{k}^{*}(y)\right]}{\Delta z}\right) \delta_{k\neq 3}$$
(A70)

Note that we use  $\delta_{k\neq 3}$  to indicate that  $\delta_{k\neq 3}=1$  if  $k\neq 3$ , and  $\delta_{k\neq 3}=0$  if k=3. The decomposition of the sum  $\overline{A_k}+\overline{F_k}$  is treated as follows.  $\overline{A_k}$  subsumes the advective contributions to the FCE explained in Section 2.2.3. The FCE-induced momentum flux changes which are purely advective, are then of the form

$$\overline{A_k} = \frac{\sum_{\text{eddies}} \left[ u_3^{\dagger}(y^{\dagger}) u_k^*(y^{\dagger}) - u_3(f(y)) u_k^*(y) \right]}{\Delta z} + \frac{\sum_{\text{d. adv.}} \left[ u_3^{\dagger}(y^{\dagger}) u_k^*(y^{\dagger}) - u_3(y) u_k^*(y) \right]}{\Delta z}$$
(A71)

For k = 3, the source contribution  $\overline{F_3}$  to the momentum flux is calculated summing the deterministic advancement and eddy event contributions as

$$\overline{F_3} = \frac{\sum_{\text{eddies}} \left[ u_3^{2\dagger}(y^{\dagger}) - u_3^{\dagger}(y^{\dagger}) u_3^*(y^{\dagger}) \right]}{\Delta z} + \frac{\sum_{\text{d. adv.}} \left[ u_3^{2\dagger}(y^{\dagger}) - u_3^{\dagger}(y^{\dagger}) u_3^*(y^{\dagger}) \right]}{\Delta z}$$
(A72)

 $\overline{F_3}$  is the equivalent average pressure change which is induced as the net momentum flux source in S-ODT. Note that transported scalars, such as  $u_k$  for  $k \neq 3$ , satisfy the condition  $\overline{F_k} = 0$ , such that only  $\overline{F_3} \neq 0$ .

We now discuss the calculation method for the Reynolds stress in S-ODT. One calculation method considers the evaluation of the mean velocity profile, as in T-ODT. The same comments concerning the use of the average velocity profile instead of the deterministic advancement changes are applicable. We calculate the Reynolds stress (consistent with the balance of Eq. (A68)) as,

$$\overline{v'u_3'} = I_3 = -\int_{-\delta}^{y} \left(\overline{M_3} + \overline{T_3} + \overline{A_3}\right) dy^*$$
(A73)

Next, we obtain the S-ODT TKE flux equation. The appearance of the terms  $A_k$  and  $F_k$  allows free interchange of the velocity  $u_3$  into or out of the partial streamwise derivative on the LHS of Eq. (A67), reflecting an analogous effect of the enforcement of the continuity equation when transforming from the strong to the weak form, or vice-versa, of the Navier-Stokes equation. That is, the presence of  $A_k$  and  $F_k$  is the formal equivalent of the mass conservation enforcement due to the FCE step in the S-ODT

formulation at discussion here. The corresponding Reynolds average equation associated to Eq. (A67) is, without invoking statistical streamwise homogeneity,

$$\frac{\partial \overline{u_3} \ \overline{u_k}}{\partial z} = -\frac{\partial (\overline{u_3' u_k'})}{\partial z} + \eta \frac{\partial^2 \overline{u_k}}{\partial y^2} + \overline{M_k} + \overline{T_k} + \overline{A_k} + \overline{F_k}. \tag{A74}$$

The Reynolds shear stresses are defined by

$$\overline{v'u'_k} = I_k = -\int_{-\delta}^{y} \left( \overline{M_k} + \overline{T_k} + \overline{A_k} \right) dy^*. \tag{A75}$$

The corresponding kinetic energy of each velocity component is then the multiplication of Eq. (A67) by  $u_k$ ,

$$u_k \frac{\partial u_3 u_k}{\partial z} = \eta u_k \frac{\partial^2 u_k}{\partial y^2} + \frac{1}{2} \left( M_{kk} + T_{kk} + A_{kk} + F_{kk} + S_{kk} \right), \quad \text{such that}$$

$$\frac{1}{2} \frac{\partial (u_3 u_k^2)}{\partial z} = \frac{\eta}{2} \frac{\partial^2 u_k^2}{\partial y^2} - \eta \left( \frac{\partial u_k}{\partial y} \right)^2 + \frac{1}{2} \left( M_{kk} + T_{kk} + A_{kk} + F_{kk} + S_{kk} \right)$$
(A76)

Here, quantities with subscripts kk are contributions to the induced rate of change of  $u_3u_k^2$  with respect to z, defined analogous to Eq. (A69 - A72). In that sense,  $M_{33} + T_{33}$  is responsible for a kinetic energy flux change due to  $u_3$  from  $u_3^3(y)$  to  $u_3(f(y))u_3^{*2}(y)$ . Similarly,  $A_{33}$  induces the change from  $u_3(f(y))u_3^{*2}(y)$  to  $u_3^{\dagger}(y^{\dagger})u_3^{*2}(y^{\dagger})$ , while  $F_{33}$  changes it to  $u_3^{3\dagger}(y^{\dagger})$ . Both  $A_{33}$  and  $F_{33}$  being applicable for the deterministic advancement and eddy event contributions. As in the T-ODT TKE budget,  $S_{kk}$  is included in Eq. (A76) although  $S_k$  is omitted from Eq. (A67) in order to indicate that it is again eliminated from the TKE budget as a matter of definition without requiring any additional modeling assumptions. Following a similar derivation procedure as in T-ODT, we obtain the equation for the average of the square of the fluctuation velocity  $u_k'$ ,

$$\overline{u_3} \frac{\partial \overline{u_k'^2}}{\partial z} = \eta \frac{\partial^2 \overline{u_k'^2}}{\partial y^2} - 2\eta \overline{\left(\frac{\partial u_k'}{\partial y}\right)^2} - \left[\frac{\partial \overline{u_3'u_k'u_k'}}{\partial z} + \frac{\partial}{\partial y} \left(I_{kk} - 2\overline{u_k}I_k\right) - \left(\overline{F_{kk}} - 2\overline{u_k}\overline{F_k} + \overline{S_{kk}}\right)\right] - \left(2\overline{u_3'u_k'}\frac{\partial \overline{u_k}}{\partial z} + 2I_k\frac{\partial \overline{u_k}}{\partial y}\right) \tag{A77}$$

where we have used the definition

$$I_{kk} = -\int_{\gamma_w}^{\gamma} \left( \overline{M_{kk}} + \overline{T_{kk}} + \overline{A_{kk}} \right) dy^*$$
(A78)

Finally, the generalized TKE budgets in planar S-ODT are,

$$P_{\text{ODT}} = -\sum_{k} \left( \overline{u_3' u_k'} \frac{\partial \overline{u_k}}{\partial z} + I_k \frac{\partial \overline{u_k}}{\partial y} \right), \quad \varepsilon_{\text{ODT}} = \sum_{k} \eta \left( \overline{\frac{\partial u_k'}{\partial y}} \right)^2, \quad \mathcal{T}_{V, \text{ODT}} = \frac{\eta}{2} \sum_{k} \frac{\partial^2 \overline{u_k'^2}}{\partial y^2},$$

$$\mathcal{T}_{A, \text{ODT}} = \frac{1}{2} \sum_{k} \left[ \overline{\frac{\partial \overline{u_3' u_k' u_k'}}{\partial z}} + \frac{\partial}{\partial y} \left( I_{kk} - 2\overline{u_k} I_k \right) \right] - \mathcal{T}_{\Gamma, \text{ODT}}, \quad \mathcal{T}_{\Gamma, \text{ODT}} = \frac{1}{2} \sum_{k} \left( \overline{F_{kk}} - 2\overline{u_k} \overline{F_k} + \overline{S_{kk}} \right).$$
(A79)

Although  $\sum_k \overline{S_{kk}} = 0$  as in the temporal formulation, we note that the advective transport term incorporates now a transport of kinetic energy by the effects of a source of momentum flux  $\mathcal{T}_{\Gamma, \text{ODT}}$ . The latter could be analogous to the pressure transport in the conventional TKE equation. Nonetheless, the contribution of  $\mathcal{T}_{\Gamma, \text{ODT}}$  to the TKE budgets in the cases evaluated in this work was shown to be negligible, see Section 5. Similar observations concerning the calculation of an alternative  $\varepsilon_{\text{bal}}$  follow as in T-ODT.

# A.5.3 Cylindrical T-ODT formulation

We now introduce the derivation of the ODT TKE equation for the cylindrical formulation. This derivation provides an important insight regarding assumptions made in the cylindrical ODT formulation. In order to derive the cylindrical TKE budgets, we follow the same methodology as in the planar case. The starting point in this case is the T-ODT cylindrical momentum equation given by rewriting Eq. (9) in an Eulerian differential framework in cylindrical coordinates as follows:

$$\frac{\partial u_k}{\partial t} = -\frac{1}{\rho} \frac{\mathrm{d}\overline{p}}{\mathrm{d}z} \delta_{k3} + \frac{\eta}{r} \frac{\partial}{\partial r} \left( r \frac{\partial u_k}{\partial r} \right) + M_k + T_k \tag{A80}$$

Note that we will use the coordinate system r and not  $\hat{r}$  in this appendix, motivated by the symmetry of all statistical flow moments around the pole. Note also that our cylindrical formulation specializes to the case with k = 3, due to our choice of the ODT model parameter  $\alpha = 0$ , see Section 4.1. Eq. (A80) is compared with the steady pipe flow RANS momentum evolution,

$$0 = -\frac{1}{\rho} \frac{d\overline{\rho}}{dz} + \frac{\eta}{r} \frac{\partial}{\partial r} \left( r \frac{\partial \overline{u_3}}{\partial r} \right) - \frac{1}{r} \frac{\partial \left( r \overline{v' u_3'} \right)}{\partial r}. \tag{A81}$$

The mean T-ODT momentum evolution is in this case, invoking statistical stationarity,

$$0 = -\frac{1}{\rho} \frac{d\overline{p}}{dz} + \frac{\eta}{r} \frac{\partial}{\partial r} \left( r \frac{\partial \overline{u_3}}{\partial r} \right) + \overline{M_3} + \overline{T_3}$$
(A82)

Comparing Eqs. (A81) and (A82), the Reynolds stress component  $\overline{v'u'_3}$  in the T-ODT cylindrical case can then be defined analogously to the T-ODT planar formulation. Indeed, the integral of  $\overline{M_3} + \overline{T_3}$  yielding  $\overline{v'u'_3}$  can be calculated just like in the planar case by two possible methods. The first method is by the integration of the mean velocity profile. The second method requires the evaluation of the changes in the velocity profiles due to mapping and kernel operations (eddy events), in order to evaluate  $\overline{M_3} + \overline{T_3}$  by Eq. (A61). Nonetheless, unlike in the planar case, the integration of  $\overline{M_3} + \overline{T_3}$  is done along the radial direction dr using the radial weight r. This yields the Reynolds stress  $r\overline{v'u'_3}$  as a radially weighted flux.

$$r\overline{v'u'_3} = rI_3 = \int_r^{\delta} (\overline{M_3} + \overline{T_3})r^* dr^*$$
(A83)

It is important to stress again that ODT simulations take place in a dynamically adaptive grid. The only possible way in which statistics can be gathered, either by means of an online temporal average in T-ODT, or an online streamwise average in S-ODT (for the case of the statistically stationary and statistically streamwise homogeneous flows at discussion here), is by the interpolation of flow quantities from the irregular, dynamically adaptive grid, to a fixed (and in our case equidistant) statistics grid. This supposes that interpolation methods are inherently implied when calculating averages. In practice, we employ cubic spline interpolations, such that we obtain high order reconstructions of the flow for use in the online averaging procedure in the fixed statistics grid. Consider now the planar T-ODT formulation, where the Reynolds stress is calculated by Eq. (A60). Using a midpoint rule for evaluation of the integral in Eq. (A60) leads to an approximation with a second-order spatial numerical error term, such that

$$\overline{v'u'_3}(y) = -\sum_{i,y_i > -\delta}^{y_i < y} \left( \overline{M_{3i}} + \overline{T_{3i}} \right) \Delta y + \mathcal{O}((\Delta y)^2)$$
(A84)

We have used  $\Delta y$  to indicate the equidistant and fixed statistics grid spacing in Eq. (A84). The numerical error  $\mathcal{O}(\Delta y^2)$  refers in this case, solely, to the midpoint rule used for the evaluation of the integral in Eq. (A60). We note that  $\overline{v'u'_3}$  is properly reconstructed with a numerical simulation order of accuracy equivalent to that obtained by all flow variables in the ODT flow simulation (implicit Euler time-integration method using linear interpolation for the diffusion flux, see Appendix A.3). Consider now the discrete form of Eq. (A83), when solving for the Reynolds stress in cylindrical coordinates,

$$\overline{v'u'_3}(r) = -\frac{1}{r} \sum_{i,r,<\delta}^{r_i > r} \left( \overline{M_{3_i}} + \overline{T_{3_i}} \right) r_i \Delta r + \frac{\mathcal{O}((\Delta r)^2)}{r}$$
(A85)

Eq. (A85) shows that the numerical error term due to the numerical integral approximation will always be responsible for large errors in the reconstruction of the Reynolds stress when  $r \to 0$ . This is an important issue to consider when evaluating cylindrical ODT Reynolds stresses. To that extent, the conservative ODT cylindrical formulation is only able to confidently predict the radially weighted Reynolds stress  $r\overline{v'v'u'_3}$ , and not the Reynolds stress itself  $\overline{v'v'_3}$ , in the presence of even small numerical errors. The alternative method for calculation of the Reynolds stress,  $\overline{v'u'_3}$  used in Section 5, that is, using the mean velocity profile instead of the changes due to eddy events, provides better results in this context. Another clear issue when computing the Reynolds stress by Eq. (A85) is that it is not possible to compute the numerical integral throughout the entire radial  $\hat{r}$  numerical domain, since doing that would result in a blowup term at  $\hat{r} = 0$ . Thus, Eq. (A85) can only be evaluated on either the seminegative or the semi-positive radial domain, ensuring that  $|\hat{r}| > 0$ . The numerical integration from both walls towards  $\hat{r} \to 0$ , or alternatively, from  $|\hat{r}| > 0$  to each wall separately, are then suitable numerical integration strategies. This is also the natural way to solve for the pole singularity in FVMs, i.e., setting fluxes from the degenerate volume element faces at r = 0 to zero.

In order to obtain the cylindrical ODT TKE equation, we proceed by finding the kinetic energy equation of the  $u_3$  streamwise velocity component,

$$\frac{1}{2}\frac{\partial u_3^2}{\partial t} = -\frac{u_3}{\rho}\frac{d\overline{p}}{dz} + \eta \frac{u_3}{r}\frac{\partial}{\partial r}\left(r\frac{\partial u_3}{\partial r}\right) + \frac{1}{2}\left(M_{33} + T_{33} + S_{33}\right),$$

$$\frac{\partial u_3^2}{\partial t} = -\frac{2u_3}{\rho}\frac{d\overline{p}}{dz} + \frac{\eta}{r}\frac{\partial u_3^2}{\partial r} + \eta \frac{\partial^2 u_3^2}{\partial r^2} - 2\eta\left(\frac{\partial u_3}{\partial r}\right)^2 + M_{33} + T_{33} + S_{33}$$
(A86)

Analogously to the planar case, the equation for the average of the square of the fluctuation velocity  $u_3'$  can be obtained as

$$\frac{\partial \overline{u_3'^2}}{\partial t} = \frac{\eta}{r} \frac{\partial}{\partial r} \left( r \frac{\partial \overline{u_3'^2}}{\partial r} \right) - 2\eta \overline{\left( \frac{\partial u_3'}{\partial r} \right)^2} - \left\{ \frac{1}{r} \frac{\partial}{\partial r} \left[ r \left( I_{33} - 2\overline{u_3} I_3 \right) \right] - \overline{S_{33}} \right\} - 2I_3 \frac{\partial \overline{u_3}}{\partial r}. \tag{A87}$$

Here, we have used the notation  $I_{33} = -(1/r) \int_0^r (\overline{M_{33}} + \overline{T_{33}}) r^* dr^*$ , with evaluation of  $\overline{M_{33}} + \overline{T_{33}}$  as in the planar formulation. A subtraction and addition of  $2I_3\partial\overline{u_3}/\partial r$  is required, just as in the planar case, in order to obtain the final expression. It is interesting to note that, when comparing this expression to the generalized TKE equation in cylindrical coordinates (see, e.g. Eqs. (B.31-B.33) in Shiri, 2010 [56]), a series of terms could be missing in the model if we try to generalize Eq. (A87) to the radial and tangential fluctuating velocity components,  $\overline{u_1'^2}$  and  $\overline{u_2'^2}$ . In a cylindrical coordinate system, the diffusion evolution equations for  $u_1$  and  $u_2$  do not have in general the same terms as  $u_3$  (in contrast to the planar case). In this sense, the budget terms obtained by analyzing Eq. (A87) represent only radial fluxes, a radial TKE production term, and interestingly enough, a planar dissipation component. In order to be able to obtain a more consistent representation of the TKE budget terms in a vector formulation, different equations for the radial and tangential velocity components would be required, not only in the diffusion evolution PDEs, but possibly in the same eddy implementation procedure. Although this is a minor technicality, given that the non-streamwise velocity components are just interpreted as energy containers in the ODT vector formulation [32], we maintain a consistent representation by applying a scalar treatment of the momentum and energy, which we accomplish by setting  $\alpha$  in the cylindrical formulation to 0, and using the corresponding momentum equation consistent with a single component formulation, Eq. (9), see also the discussion in Sections 2.2.2 and 4.1.

The TKE budget terms are consequently identified based on Eq. (A87) as

$$P_{\text{ODT}} = -I_3 \frac{\partial \overline{u_3}}{\partial r}, \quad \varepsilon_{\text{ODT}} = \eta \overline{\left(\frac{\partial u_3'}{\partial r}\right)^2}, \quad \mathcal{T}_{V,\text{ODT}} = \frac{\eta}{2r} \frac{\partial}{\partial r} \left(r \frac{\partial \overline{u_3'^2}}{\partial r}\right), \quad \mathcal{T}_{A,\text{ODT}} = \frac{1}{2r} \frac{\partial}{\partial r} \left[r \left(I_{33} - 2\overline{u_3}I_3\right)\right], \quad (A88)$$

where  $\overline{S_{33}}$  is omitted from the advective transport term  $\mathcal{T}_{A,\text{ODT}}$  since there is no kernel application during an  $\alpha = 0$  eddy event, despite kernel functions being still used to determine the eddy occurrence frequencies.

# A.5.4 Cylindrical S-ODT formulation

Similar to the spatial planar formulation, the generalized spatial ODT cylindrical momentum evolution for u<sub>3</sub> is given by

$$\frac{\partial u_3 u_3}{\partial z} = \frac{\eta}{r} \frac{\partial}{\partial r} \left( r \frac{\partial u_3}{\partial r} \right) + M_3 + T_3 + A_3 + F_3. \tag{A89}$$

Averaging Eq. (A89), results in

$$\frac{\partial \overline{u_3} \, \overline{u_3}}{\partial z} = -\frac{\partial \overline{u_3' u_3'}}{\partial z} + \frac{\eta}{r} \frac{\partial}{\partial r} \left( r \frac{\partial \overline{u_3}}{\partial r} \right) + \overline{M_3} + \overline{T_3} + \overline{A_3} + \overline{F_3}. \tag{A90}$$

The Reynolds stress component  $\overline{v'u'_3}$  is then equivalent to  $I_3$ , where

$$r\overline{v'u'_3} = rI_3 = -\int_0^r \left(\overline{M_3} + \overline{T_3} + \overline{A_3}\right) r^* dr^*. \tag{A91}$$

The evaluation of  $\overline{M_3} + \overline{T_3}$  and  $\overline{A_3}$  is carried out as in the planar formulation by Eq. (A69) and (A71). Likewise,  $\overline{F_3}$  in Eq. (A90) can be evaluated by Eq. (A72).

The equation for the average of the square of the fluctuation velocity  $u_3'$  can be obtained using the definition

$$I_{33} = -\frac{1}{r} \int_0^r \left( \overline{M_{33}} + \overline{T_{33}} + \overline{A_{33}} \right) r^* dr^*, \tag{A92}$$

such that

$$\overline{u_3} \frac{\partial \overline{u_3'^2}}{\partial z} = \frac{\eta}{r} \frac{\partial}{\partial r} \left( r \frac{\partial \overline{u_3'^2}}{\partial r} \right) - 2\eta \overline{\left( \frac{\partial u_3'}{\partial r} \right)^2} - \left\{ \frac{\partial \overline{u_3'u_3'u_3'}}{\partial z} + \frac{1}{r} \frac{\partial}{\partial r} \left[ r \left( I_{33} - 2\overline{u_3}I_3 \right) \right] - \left( \overline{F_{33}} - 2\overline{u_3}\overline{F_3} + \overline{S_{33}} \right) \right\} - \left( 2\overline{u_3'u_3'} \frac{\partial \overline{u_3}}{\partial z} + 2I_3 \frac{\partial \overline{u_3}}{\partial r} \right).$$
(A93)

The TKE budget terms considering  $\alpha = 0$  (one velocity component) are then

$$P_{\text{ODT}} = -\left(\overline{u_3'u_3'}\frac{\partial \overline{u_3}}{\partial z} + I_3\frac{\partial \overline{u_3}}{\partial r}\right), \quad \varepsilon_{\text{ODT}} = \eta \overline{\left(\frac{\partial u_3'}{\partial r}\right)^2}, \quad \mathcal{T}_{V,\text{ODT}} = \frac{\eta}{2r}\frac{\partial}{\partial r}\left(r\frac{\partial \overline{u_3'^2}}{\partial r}\right),$$

$$\mathcal{T}_{A,\text{ODT}} = \frac{1}{2}\left\{\frac{\partial \overline{u_3'u_3'u_3'}}{\partial z} + \frac{1}{r}\frac{\partial}{\partial r}\left[r\left(I_{33} - 2\overline{u_3}I_3\right)\right]\right\} - \mathcal{T}_{\Gamma,\text{ODT}}, \quad \mathcal{T}_{\Gamma,\text{ODT}} = \frac{1}{2}\left(\overline{F_{33}} - 2\overline{u_3}\overline{F_3}\right),$$
(A94)

with  $\overline{S_{33}}$  again omitted from  $\mathcal{T}_{A,\text{ODT}}$  (or  $\mathcal{T}_{\Gamma,\text{ODT}}$ ) for  $\alpha = 0$ .

#### B EXTENDED RESULTS FOR THE CYLINDRICAL FORMULATION

## B.1 Cylindrical formulation results at low Reynolds numbers using large values of $A_{\rm tf}$

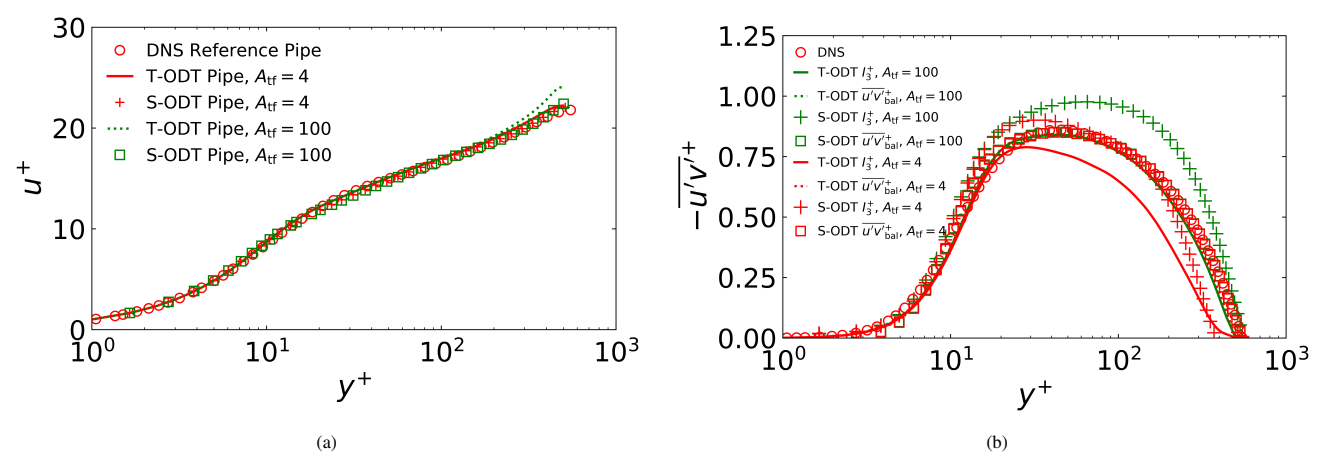
In the following, we compare flow statistics obtained with the T-ODT and S-ODT cylindrical formulations for cases 500PT and 550PS. We use the calibrated value of  $A_{tf} = 4$  for  $Re_{\tau} \approx 550$ , which yields steady state imbalances as seen in Section 4.5, and the very large value  $A_{tf} = 100$ , which ensures steady state numerical flux balancing.

Figure B4a shows a comparison of the mean velocity profiles. In this case, the sensitivity to  $A_{tf}$  is larger for the T-ODT cylindrical formulation.

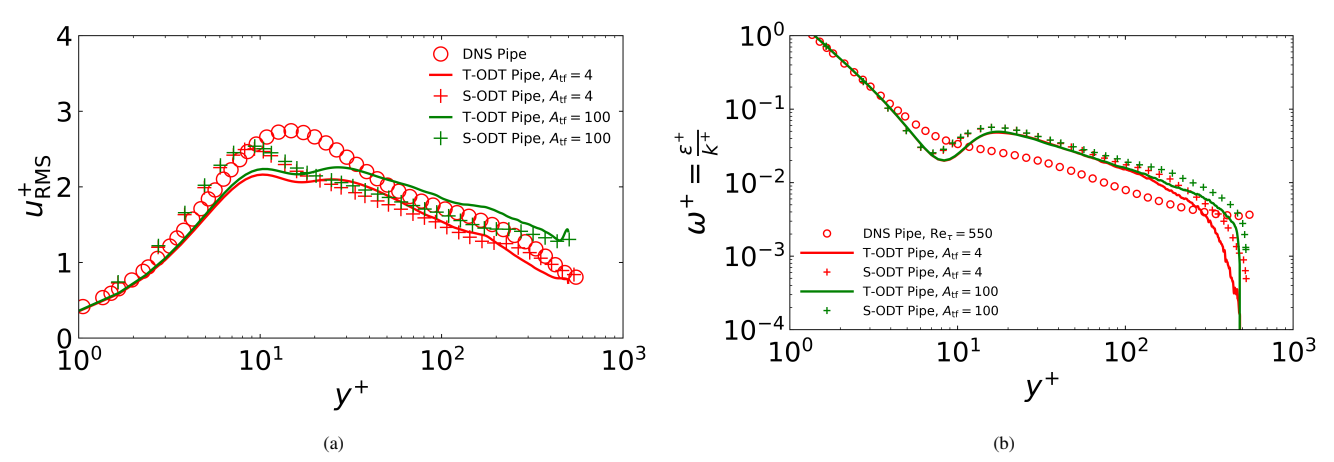
Figure B4b shows a comparison of the Reynolds shear stress profile, calculated using two different methods. The first method refers to  $\overline{u'v'}_{bal}$ , determined by the forced steady state balance of the RANS momentum equation, Eq. (26). The second method refers to  $I_3$  as in Appendix A.5, accounting for the numerical average of advective flux contributions. Figure B4b shows that the large value  $A_{tf} = 100$  achieves convergence of both calculation methods to the same result in both T-ODT and S-ODT, given that numerical diffusion due to grid adaption is reduced.

Figure B5a shows a comparison of the streamwise RMS velocity profile. In this case, the larger value of  $A_{tf}$  is responsible for increased turbulence intensity levels away from the wall, close to the pole r = 0, in both the T-ODT and S-ODT cylindrical formulations. This is related to the pole numerical artifacts discussed in Appendix A.3. We verify that it is not possible to achieve monotonic decrease of the RMS velocity profile in the outer layer, as demanded by DNS, with the steady state numerical flux balancing yielded by large values of  $A_{tf}$ .

Finally, Figure B5b shows a comparison of the turbulence frequency  $\omega^+$ . We note that in the cylindrical ODT one velocity component formulation, the TKE is given by  $k = u_{\text{RMS}}^2/2$ . Figure B5b shows that larger values of  $A_{\text{tf}}$  are responsible for increased turbulence frequency levels away from the wall, which is not a trivial result given that k also increases for larger  $A_{\text{tf}}$  away from the wall, towards the pole.



**FIGURE B4** (a) Mean velocity profiles for turbulent pipe flow cases 500PT (T-ODT) and 550PS (S-ODT) using values of  $A_{tf}$  of 4 and 100. (b) Reynolds shear stress profiles for turbulent pipe flow cases 500PT (T-ODT) and 550PS (S-ODT) using values of  $A_{tf}$  of 4 and 100. Two methods for calculation of the Reynolds shear stress are shown, see text. DNS turbulent pipe flow data from [46] is shown for reference in both (a) and (b).



**FIGURE B5** (a) RMS streamwise velocity profiles for turbulent pipe flow cases 500PT (T-ODT) and 550PS (S-ODT) using values of  $A_{\rm tf}$  of 4 and 100. (b) Turbulence frequency profiles for turbulent pipe flow cases 500PT (T-ODT) and 550PS (S-ODT) using values of  $A_{\rm tf}$  of 4 and 100. DNS turbulent pipe flow data from [46] is shown for reference in both (a) and (b).